Hydrodynamic Escape of Planetary Atmospheres Revisited

Richard D. Chatterjee

Under the Supervision Of:

Prof. Raymond Pierrehumbert

A thesis submitted in partial fulfilment for the degree of Doctor of Philosophy

Merton College · University of Oxford · August 2025

To working in the storied tradition of physics and uncovering some small facet of nature.

Declaration

I hereby declare that except where specific reference is made to the work of others, the contents of this dissertation are original and have not been submitted in whole or in part for consideration for any other degree or qualification in this, or any other university. Material originating from jointly authored publications is explicitly noted below and in the main text.

Chapters 2 and 3 are accepted at The Astrophysical Journal as

> Chatterjee, R. D. and Pierrehumbert, R.T, "Novel Physics of Escaping Secondary Atmospheres May Shape the Cosmic Shoreline," *arXiv*:2412.05188 (2024).

Chapter 4 incorporates sections I wrote for two jointly-authored publications accepted in the Monthly Notices of the Royal Astronomical Society. I modelled the XUV luminosity evolution of the host stars with `MORS` and assessed the resulting potential for atmospheric loss and revival.

> Taylor, J., Radica, M., Chatterjee, R. D. et al "JWST NIRISS transmission spectroscopy of the super-Earth GJ 357b, a favourable target for atmospheric retention," *MNRAS* (July 2025) — See Section 4. "The Potential for an Atmosphere".

> Nicholls, H., Guimond, C.M. , Hay H.C., Chatterjee, R.D., et al "Self-limited tidal heating and prolonged magma oceans in the L 98-59 system," *MNRAS* (August 2025) — See Section 3.6. "Context of atmospheric escape".

Chapter 4 also presents figures I prepared using data from the following jointly-authored publication in the Astrophysical Journal, with all accompanying text my own:

> Ji, X., Chatterjee, R.D., Park Coy, B., Kite, E.S., "The Cosmic Shoreline Revisited: A Metric for Atmospheric Retention Informed by Hydrodynamic Escape," *ApJ* (October 2025)

Chapter 5 features a figure I produced from simulation outputs run by Dr. Shane R. Carberry Mogan using a version of his custom `Harrah` code, in the context of my EPSC-DPS2025-1756 abstract ("Refining Exoplanet Escape Predictions with Molecular-Kinetic Simulations"); all accompanying text is my own.

Richard D. Chatterjee
January 2026

Acknowledgements

It has been a privilege to work on this topic, and I am deeply grateful to the many people whose support has brought me here.

I owe the opportunity to my supervisor, Ray Pierrehumbert, whom I wish to thank for his belief in me and giving me the freedom to research in new directions. Ray is renowned for his breadth of insight into physics, but it is his great enthusiasm and curiosity that I have enjoyed most.

Second, I am grateful to Robert E. Johnson and Shane Carberry Mogan for their receptiveness, generosity, and expertise, all of which encouraged me to pursue my ideas with confidence — I hope to take our work far.

Next, comes the experts on hydrodynamic escape whose research inspries me and who have provided me with invaluable guidance — Antonio García Muñoz, Matthäus Schulik, Richard Booth. I also wish to thank Tim Lichtenberg, David Marshall and Oli Shorttle who went out of their way to support my aspirations.

Many thanks to Xuan Ji and Edwin Kite for opening up their project to revisit the cosmic shoreline to my input. I count myself fortunate to have had the opportunity to help shape such an important study and it was a pleasure to work together.

This thesis should in part be devoted to Ed, Hamish, Namrah, Sally — my experience would have not have been the same without your welcome to Room 206 and your friendship. Special thanks go to Sally for a fascinating collaboration and for running and developing a multitude of photochemical simulations. My appreciation goes out to the whole exoplanets community at Oxford, including Harrison, Tobias, Chloe, Claire, Mark, Marylou, John, Alex, Tad. Especially, Harrison Nicholls for cool collaborations and Jake Taylor for taking me under his wing in my final year. I am grateful to STFC, ERC, Merton College and AEThER for trips worldwide that greatly enriched my experience.

Thanks to the community of physicists who came up alongside me and who continue to inspire me: Rayhan, Oskar, Ross, Liam, Wojtek, Alex and Khalid. Special thanks to Oskar Määttä for a parallel research journey with geometric mechanics. And to Liam Lau for all the milestones we've seen together.

Thanks to the physics professors at Merton College: Alex, Alan, Simon and James, with whom it was the greatest privilege to have tutorials. And to the generation of Mertonians ahead of us, who were also amazing tutors— Anthony, Glenn, Mantas and Toby. Then to my students at Merton, as well as those at St Peter's and the Maths Institute.

Looking back, I would like to thank Sarah Usher for being a brilliant and enthusiastic physics teacher. And to all those at school who listened to my first expositions of physics and are still listening: Adam, Alfie, Matty and Matthew. To Matthew in particular for the creative outlet of the @climatephysics collaboration.

Thanks to Christine, Clement, Bozena, and Sophia for all their support. Thanks most of all to my mother, Sheila, to whom I owe so much and who continues to be a source of inspiration, and to my brothers, Jacob and Laurence, for the adventures we have shared.

Last but not least, *To my wife and soulmate, Kasia— thanks for everything.*

Abstract

The astonishing sensitivity of the James Webb Space Telescope (*JWST*) enables astronomers to characterise the thermal emission of temperate, rocky planets orbiting small, cool stars dozens of light years away. There is a catch: while these low-mass M-dwarf host stars promise a window into the occurrence of Earth- and Venus-like atmospheres, they also disproportionately bathe their planets in intense ionising irradiation that can boil those atmospheres away. The "radius valley," a bimodality in the radius–period distribution of sub-Neptunes found by Kepler, was predicted using models of the photoionisation-driven outflow of primordial hydrogen envelopes. Now, with *JWST*, attention turns to the hypothesised "cosmic shoreline" that divides planets with and without atmospheres, and the theoretical frontier has shifted to metal-dominated outflows, a unique astrophysical regime.

The research presented here investigates the dynamics of rapid atmospheric escape across the size range of rocky planets, focusing on the interplay between stellar XUV (X-ray and EUV) irradiation, gravitational binding, and atomic line cooling. The loss of secondary atmospheres, particularly nitrogen-dominated ones, is examined using three complementary approaches: analytic modelling, time-dependent hydrodynamics, and Monte Carlo simulation of molecular-kinetics, while accounting for the rotational and magnetic evolution of host stars, and plausible volatile supply histories.

We first construct an analytic framework for XUV-driven outflows, identifying the threshold for collisional transonic escape from Earth- and Mars-sized bodies and ensuing energy-limited mass loss rates. The radial structure of escaping atmospheres is modelled as a polytropic expansion, a power-law relationship between density and temperature driven by local XUV heating, with atomic line cooling incorporated via a three-level atom model. For super-Earths, we explore the transition to a "collisional–radiative thermostat" regime, in which the global ion outflow is regulated by efficient line cooling. The framework also accounts for the ion-exobase and the ambipolar electrostatic field, which reduces the effec-

tive mean molecular weight, and highlights the limitations of earlier models that neglected these effects.

Preliminary numerical simulations are developed to explore the transition from hydrostatic to hydrodynamic thermospheres and from subsonic to supersonic outflow regimes. A solver for the spherically symmetric Euler equations, based on the semi-Lagrangian Constrained Interpolation Profile (CIP) algorithm, is implemented and validated, demonstrating its ability to capture steep gradients with minimal numerical diffusion. Simulations of hydrodynamic escape under progressive heating illustrate both the strengths and current limitations of this approach. To address the transition from collisional to collisionless flow, we outline the application of molecular-kinetic methods using the direct simulation Monte Carlo (DSMC) technique. Building on previous molecular-kinetic models of escape from lower-gravity bodies such as Pluto, we present a DSMC simulation of thermal, subsonic escape from an artificially hot Earth-like thermosphere.

Together, these methods characterise unexplored escape regimes, develop analytic tools that can be used in future studies, and apply them to case studies tracking cumulative atmospheric loss and the potential for volcanic replenishment. The resulting models are used to map new cosmic shorelines, revealing how the non-linear physics of escape can shift the retention boundary for high–molecular-weight atmospheres and vary its topography across stellar mass and planetary volatile content. Yet escape's sensitivity to the vast diversity of planetary and stellar environments means that the picture presented here is necessarily incomplete; advancing it will require sustained, state-of-the-art modelling to match the pace of new observations, especially those emerging from the Rocky Worlds Director's Discretionary Time program.

A growing *JWST* dataset already includes roughly a dozen rocky exoplanets whose transmission and emission spectra suggest bare surfaces or very thin atmospheres, alongside a few promising targets with indications of secondary atmospheres that may differ greatly from those in the Solar System. Determining the extent and depth of this trend, and identifying the environments most favourable for atmospheric retention, will require a range of first-principles models building on the foundations laid here. This thesis addresses the bottleneck that atmospheric loss imposes on the occurrence of observable Earth-like habitats, with direct implications for the prevalence of life in the universe.

Table of Contents

List of Figures xv

1 Introduction 1
- 1.1 The Habitable Zones of Stars . . . 2
- 1.2 Vertical Equilibria and Escape of Planetary Upper Atmospheres . . . 5
- 1.3 Signals of Exoplanets and Mass Loss . . . 10
  - 1.3.1 Detection of Exoplanets and their Exospheres . . . 10
  - 1.3.2 Radius valley and Rocky Planet Occurrence . . . 13
- 1.4 The Cosmic Shoreline and JWST . . . 15
- 1.5 An Overview of this Thesis . . . 19

2 Polytropic Solutions to Hydrodynamic Escape 21
- 2.1 Introduction . . . 21
  - 2.1.1 Analytic and Numerical Modeling . . . 23
- 2.2 Polytropic model of atmospheric escape . . . 25
  - 2.2.1 Character of XUV-driven Transonic Expansion into Space . . . 25
  - 2.2.2 Polytropic Approximation to Atmospheric Structure and Escape . . . 29
  - 2.2.3 Polytropic Solution Space . . . 33
  - 2.2.4 Lower Boundary Conditions . . . 36
- 2.3 XUV-flux Threshold for Transonic Escape . . . 36
  - 2.3.1 Knudsen Onset . . . 37
  - 2.3.2 Photoevaporation of Nitrogen Thermospheres by Active Stars . . . 40
  - 2.3.3 Young Sun Earth . . . 43
  - 2.3.4 Young Sun Mars . . . 46
- 2.4 Comparison with Johnson et al. (2013a,b) . . . 48

3 Effect of Atomic Line Cooling on Hydrodynamic Escape 51
- 3.1 Introduction . . . 51

3.2 Accounting for Non-LTE Cooling . . . 54
3.2.1 Three-level Model for Electron Excitation of Atomic Lines . . . 54
3.3 Is Line cooling Minor in the Weakly ionized Onset of Hydrodynamic Escape? . . . 59
3.3.1 Young Sun Mars . . . 59
3.3.2 Young Sun Earth . . . 60
3.4 Collisional-radiative Thermostat and Global Ion Outflow . . . 61
3.4.1 Plasma Escape Temperature . . . 61
3.4.2 Ion-Electron Recombination . . . 63
3.4.3 The Thermostat of Photoionization versus Line Cooling . . . 65
3.4.4 Comparison to Nakayama et al. (2022) . . . 67
3.4.5 TRAPPIST 1-b: Airless . . . 71
3.4.6 LHS 1140 b and c: Airy? . . . 72
3.5 Discussion . . . 73
3.5.1 Landscape of High Molecular Weight Escape . . . 73
3.6 Summary . . . 77

4 Predicting the Fate of Rocky Exoplanet Atmospheres 79
4.1 Introduction . . . 79
4.2 GJ 357 b: JWST Transmission and Potential for an atmosphere . . . 80
4.2.1 Evolution of Ionising Luminosity . . . 81
4.2.2 Possible Evolution to a Retained Atmosphere . . . 84
4.2.3 Limitations . . . 85
4.3 Escape in the L 98-59 system . . . 86
4.4 Revisiting the Cosmic Shoreline . . . 89
4.5 Magnetic Suppression of Rapid Escape . . . 100
4.6 Summary . . . 101

5 Hydrodynamic and Molecular-Kinetic Simulations of Escape 103
5.1 Introduction . . . 103
5.2 Solving Hydrodynamics with Constrained Interpolation Profiles . . . 104
5.2.1 Method . . . 105
5.2.2 Application . . . 108
5.3 Solving Molecular- Kinetics with DSMC . . . 112
5.3.1 Method . . . 112
5.3.2 Application . . . 114
5.4 Outlook . . . 117

6 Conclusions **119**

References **127**

List of Figures

1.1 Habitable zone exoplanets across stellar type . . . 3
1.2 Escape from the hydrostatic and hydrodynamic upper atmospheres of planets 6
1.3 Atmospheric loss from Dole (1964) . . . 8
1.4 Transiting exoplanet characterisation methods . . . 12
1.5 Radius distribution of low-mass, close-in planets . . . 14
1.6 The Cosmic Shoreline – cumulative XUV irradiation . . . 17

2.1 Transonic hydrodynamic escape in Mach-radius plane . . . 28
2.2 Polytropic solution space for escaping planetary atmospheres . . . 34
2.3 Onset of transonic hydrodynamic escape in a Young Sun Earth scenario . . . 44
2.4 Onset of transonic hydrodynamic escape in a Young Sun Mars scenario . . . 48

3.1 Grotrian level diagram for neutral and ionised nitrogen (NI and NII) . . . 52
3.2 Non-LTE populations of the low-lying electronic state of nitrogen (NI) . . . 57
3.3 Heating and cooling in Young Sun Earth and Mars escape scenarios . . . 58
3.4 Intercomparison of line cooling and recombination luminosities in upper atmospheres . . . 63
3.5 The collisional-radiative thermostat . . . 66
3.6 The landscape of high-molecular-weight escape . . . 74

4.1 Models of the evolution of the luminosity of GJ 357 in the X-ray and EUV bands 82
4.2 Cycle-averaged XUV energy flux in the L98-59 system and integrated escape . 87
4.3 Cosmic shorelines for planets hosted by late-G and early-K dwarfs in volatile-poor and volatile-rich scenarios . . . 90
4.4 Cosmic shorelines for planets hosted by late-K dwarfs in volatile-poor and volatile-rich scenarios . . . 94
4.5 Cosmic shorelines for planets hosted by early-to-mid-M dwarfs in volatile-poor and volatile-rich scenarios . . . 95

4.6 Cosmic shorelines for planets hosted by mid-M dwarfs in volatile-poor and volatile-rich scenarios 96
4.7 Cosmic shorelines for planets hosted by late-M dwarfs in volatile-poor and volatile-rich scenarios 97

5.1 Validation of CIP hydrocode scheme against spherical Sod Shock profiles . . . 109
5.2 CIP hydrocode simulation of the escape of hydrogen atmosphere from the Moon with XUV heating 110
5.3 Application of DSMC to monatomic nitrogen outflow 116

1

Introduction

Is planet Earth typical, exceptional, or truly unique? Its distinguishing features include a dynamic system of plate tectonics, oceans of surface water, a nitrogen–oxygen atmosphere, and a pervasive biosphere. Ancient rivers and lakes on Mars may once have provided conditions suitable for life to arise, and there is the tantalising possibility that— even if no life persists in the subsurface, evidence of past life may remain. NASA's *Europa Clipper* mission is now en route to Jupiter's icy moon to investigate whether the conditions within Europa's subsurface ocean could support a microbial ecosystem, one that might be directly sampled by future missions. The results of these and other endeavours, combined with the rapidly growing census of exoplanets, will help to address, perhaps even decisively, humanity's perennial question: Are we alone in the Universe?

The largest and most powerful ever launched into space, the James Webb Space Telescope enables detection of the thermally emitted light from cool rocky planets, heralding a new age in exoplanet astronomy and the search for life. This doctoral thesis explores the loss and retention of rocky planet atmospheres— one of the key biosphere components. While early ideas of habitability considered atmospheric escape, the emerging picture that the first cool, rocky planets we observe may be predominantly airless poses a defining and unexpected challenge for astrophysicists.

In this introduction, I begin by reviewing the concepts of habitability and the physical processes that drive atmospheric escape, then chart the foundational discoveries of exoplanet astronomy and *JWST*'s role in ushering in the era of rocky planet atmospheric characterization. I conclude by outlining how each chapter of this thesis addresses key open questions in the field.

1.1 The Habitable Zones of Stars

The circumstellar habitable zone is generally defined as where a planet is the right temperature to maintain surface oceans of water (Huang, 1959). The inner and outer edge of the conservative habitable zone are defined by the runaway greenhouse and by the maximum greenhouse (Kasting et al., 1993). The runaway greenhouse effect is where water vapour accumulates in the atmosphere to such an extent that outgoing longwave radiation no longer rises with temperature, so the planet cannot reach radiative equilibrium. Surface temperatures then rise substantially until thermal emission shifts to shorter wavelengths at which it can escape, allowing radiative equilibrium to be re-established; for an Earth-mass planet, idealized models estimate this transition to occur at temperatures of order 1400 K (Kasting, 1988). In contrast, the maximum greenhouse effect occurs when further CO_2 increases no longer warm the planet because there is a cooling offset from the resulting rise in Rayleigh scattering and thus planetary albedo. For early Mars under the fainter Young

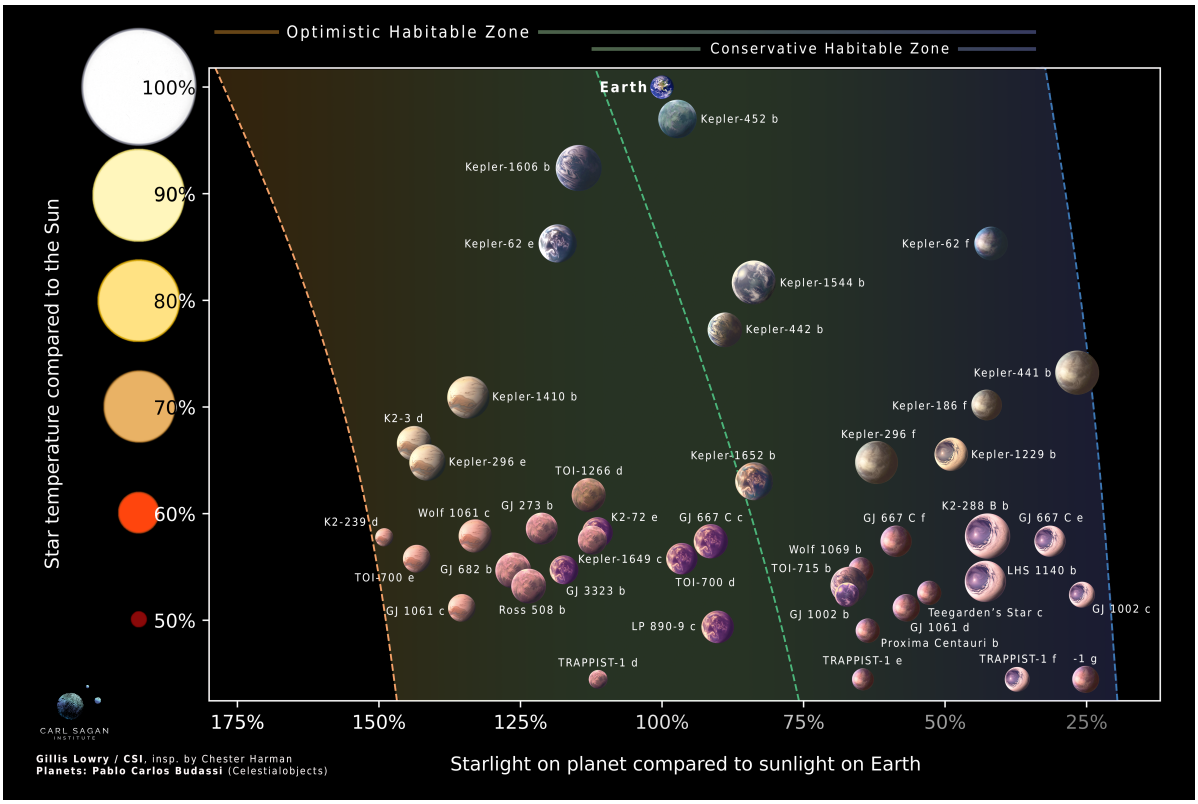

Fig. 1.1 The habitable zone for surface liquid water on planets orbiting host stars of different masses and luminosities. A selection of exoplanets from NASA Exoplanet Archive is included. Credit: Gillis Lowry, Pablo Carlos Budassi, Chester Harman.

Sun, even the maximum greenhouse effect is insufficient to place it within the conservative habitable zone despite strong geological evidence for surface liquid water (e.g. Williams et al., 2013; Kite, 2019; Kite et al., 2025), implying that the conservative HZ struggles with its first empirical test. The inclusion of Early Mars, together with recent Venus lying just outside the inner edge, defines an optimistic habitable zone (Kopparapu et al., 2013). Exoplanets orbiting in the habitable zones of G/K/M-type stars are displayed in Fig. 1.1.

G-type stars have masses around 0.91–1.09, $M_{\odot}$, effective temperatures of 5340–5940 K, and luminosities of 0.55–1.45$L_{\odot}$, with core-hydrogen-burning lifetimes of order ten billion years (Pecaut and Mamajek, 2013; Mamajek, 2022). K-dwarfs, which likewise have a radiative core and convective envelope, span 0.60–0.89$M_{\odot}$, 0.60–0.90$R_{\odot}$, 3860–5260 K, and 0.06–0.47$L_{\odot}$. M dwarfs extend down to the hydrogen-burning limit of ~ 0.08$M_{\odot}$ (M9V),

with radii as small as $\sim 0.1 R_\odot$, effective temperatures down to ~ 2400 K, and luminosities as low as $3 \times 10^{-4} L_\odot$. Late-type M dwarfs (M3V–M9V) with masses below $\sim 0.35 M_\odot$ are fully convective (Johnstone et al., 2021) and, thanks to their extremely low luminosities, sustain hydrogen fusion for trillions of years (Adams et al., 2005). Thus, unlike for the Earth for which habitability will be ended by the red giant phase of evolution, a habitable planet orbiting an M-dwarf could be stable for much longer — the universe has the vast majority of its Stelliferous Era ahead (Adams and Laughlin, 1997).

M-dwarfs are the most common stars in the galaxy and offer observational advantages for exoplanets, including the depth and frequency of transit and eclipse signals (Dressing and Charbonneau, 2015). The habitable zones of low-mass stars lie extremely close to their hosts because of the stars' much lower luminosities. Such proximity may lead to tidal locking, producing a permanent dayside and nightside like the Moon; however, this is not generally considered a severe obstacle to habitability (Maxence Lefèvre, 2021). A more pressing concern is the heightened dose of ionising radiation in M-dwarf systems, which can broil away planetary atmospheres (Selsis et al., 2007). Differential rotation in a star's convective envelope generates a magnetic field that confines and heats coronal plasma to millions of kelvin, resulting in XUV emission from metal lines and the free-free continuum. Stars are initially saturated in X-ray emission relative to bolometric luminosity, later losing angular momentum through magnetic breaking of the stellar wind until converging onto a main-sequence activity track for a given mass (Vilhu, 1984). Depending on the initial rotation rates of F, G, and K stars, their saturated phase lasts around 10 – 300 million years, compared to billions of years for the lower mass M-dwarfs due to their persistently long convective turnover timescale (Johnstone et al., 2021). One issue considered in this thesis is whether, for M-dwarf exoplanets, the orbital distance permitting long-term atmospheric retention could extend beyond the outer edge of the liquid-water habitable zone.

1.2 Vertical Equilibria and Escape of Planetary Upper Atmospheres

To escape a planet's gravitational well, material must have sufficient energy to reach the *escape velocity*; for Earth, this surface threshold is well known from rocketry and the fundamental physics of gravity as roughly $11.2\,\mathrm{km\,s^{-1}}$. The vertical structure of a planetary upper atmosphere roughly conforms to one of two steady states: hydrostatic or hydrodynamic. In hydrostatic equilibrium, the pressure gradient balances gravity up to the exobase, where the fluid–continuum (collisional) assumption breaks down. Above this level, the atmosphere is sufficiently tenuous that the fraction of particles thermally endowed with the local escape velocity outward are lost ballistically to space; this process is known as Jeans escape (Jeans, 1921).

In hydrodynamic equilibrium, the pressure gradient overcomes gravity to accelerate atmospheric layers outward, so that at each altitude there is a steady, time-independent velocity, as illustrated in Figure 1.2. If the atmosphere expands to meet the interplanetary medium and remains collisional, the flow becomes transonic, analogous to the solar wind first predicted and modelled by Parker (1958). Both regimes involve a net flux from the lower atmosphere to space. The lost gas either depletes the atmospheric reservoir of the escaping component or is replenished by processes such as outgassing. Hydrodynamic mass loss generally occurs under more extreme conditions than Jeans escape and is the more efficient of the two.

Significant mass loss requires high temperatures in the upper atmosphere and a large flux of stellar irradiation with a shorter wavelength than the hydrogen ionization edge: extreme ultraviolet (10-92 nm) and X-ray (0.1-10 nm). The strong and broad XUV photoabsorption cross-section finds the tenuous gas of the planet's infrared photosphere optically thick and efficiently drives a temperature inversion from the hot electrons and atoms released.

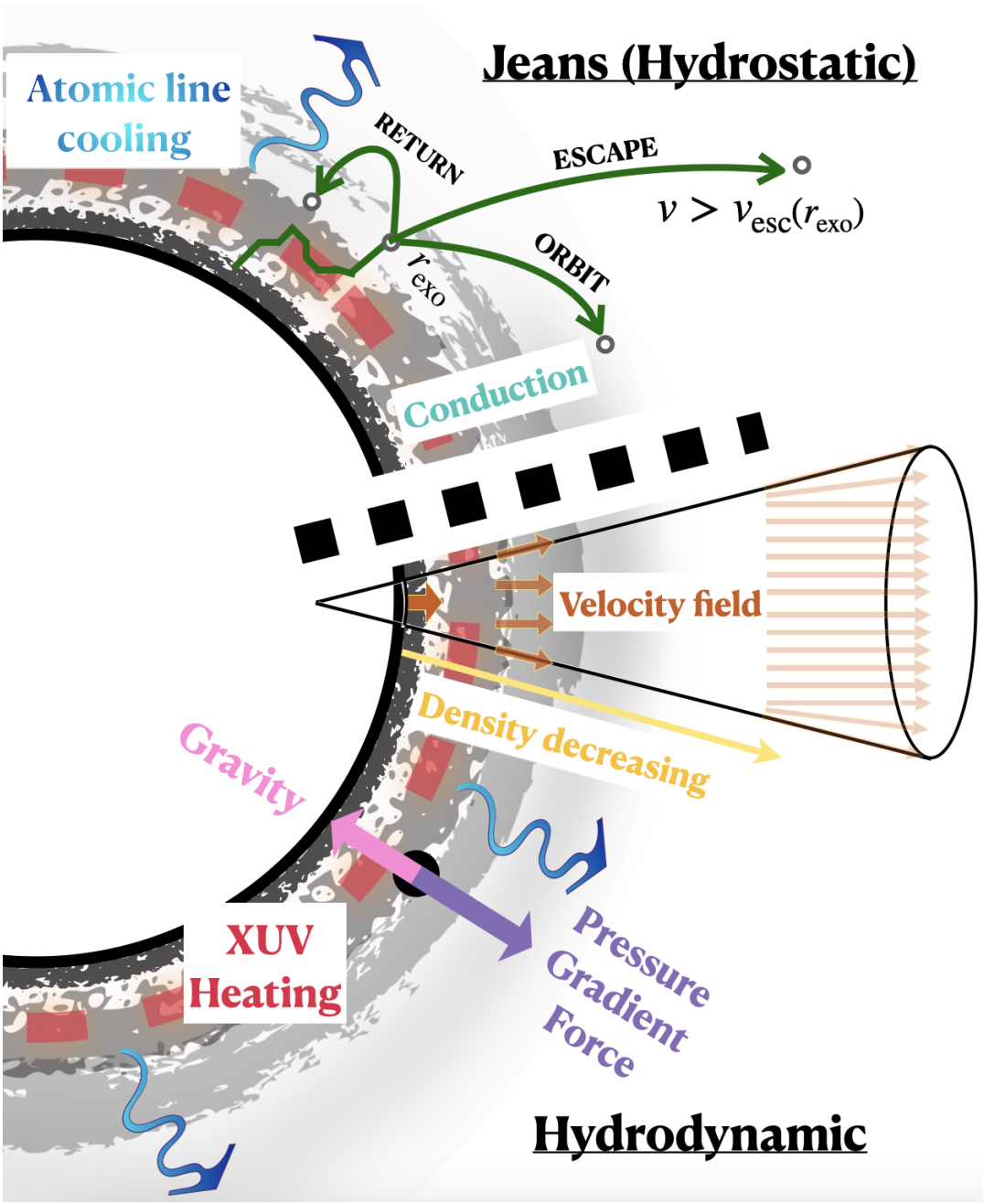

Fig. 1.2 Illustration comparing hydrodynamic and hydrostatic escape. When hydrodynamic, the net heating from XUV photoabsorption, reduced by recombination and atomic line cooling, drives a pressure gradient force to overcome gravity— accelerating the flow radially outwards down the atmosphere's density gradient. Jeans escape occurs from the hydrostatic exobase where the atmosphere becomes collisionless. If the outward-directed thermal velocity of a particle exceeds the escape velocity at the exobase, then it can ballistically escape on a hyperbolic trajectory. The balance of XUV heating, conduction, and radiative cooling determines the escape rate via the exobase temperature.

That is in contrast to the lower atmosphere, where heat from photoabsorption is efficiently reradiated as a blackbody to space, so it cannot contribute to escape.

Spitzer (1949) first recognised that downward thermal conduction can balance XUV heating in a hydrostatic atmosphere. Bates (1951) extended this work by examining how radiative–conductive equilibrium is modified by coolants, such as the far-infrared fine-structure transitions within the ground state of atomic oxygen. In such an atmosphere, the upper layers develop a temperature–pressure inversion in which, at each altitude, EUV heating—partially offset by line cooling—is balanced by the divergence of thermal conduction directed downwards toward the surface. This equilibrium persists under collisional, hydrostatic conditions up to the exobase, where it sets the temperature that, in turn, determines the atmospheric escape rate.

Once the mean free path between collisions approaches the atmospheric scale height, there is then an atmospheric loss rate to the interplanetary medium given by (Jeans, 1921)

$$\Phi_{J,\mathrm{x}} = 4\pi r_{\mathrm{x}}^2 n_{\mathrm{x}} \frac{c_{\gamma_a}}{\sqrt{2\pi\gamma_a}} (1+\lambda_x)\mathrm{e}^{-\lambda_{\mathrm{x}}},$$

where the escape parameter at the exobase, $\lambda_{\mathrm{x}} = \dfrac{GM}{RT_{\mathrm{x}} r_{\mathrm{x}}}$, is the local ratio of gravitational potential energy to thermal energy, involving Newton's gravitational constant G, the mass of the planet M and the specific gas constant R. The exobase radius, number density, temperature and adiabatic sound speed are $r_{\mathrm{x}}, n_{\mathrm{x}}, T_{\mathrm{x}}$ and $c_{\gamma_a,\mathrm{x}}$ respectively. $\gamma_a = c_p/c_v$ the ratio of the specific heats at constant pressure and volume. This formula finds the Maxwellian tail of molecules that have escape velocity and so can ballistically fly off on an hyperbolic trajectory, where those without escape velocity leave and return on an elliptic trajectory - unable to escape the Earth's gravitational field.

Fig. 1.3 from Dole (1964) illustrates the possibility of loss of atmospheric components depending on their molecular weight, the planet's gravity, and the exobase temperature. The lines show where significant erosion is possible on the timescale of hundreds of millions of

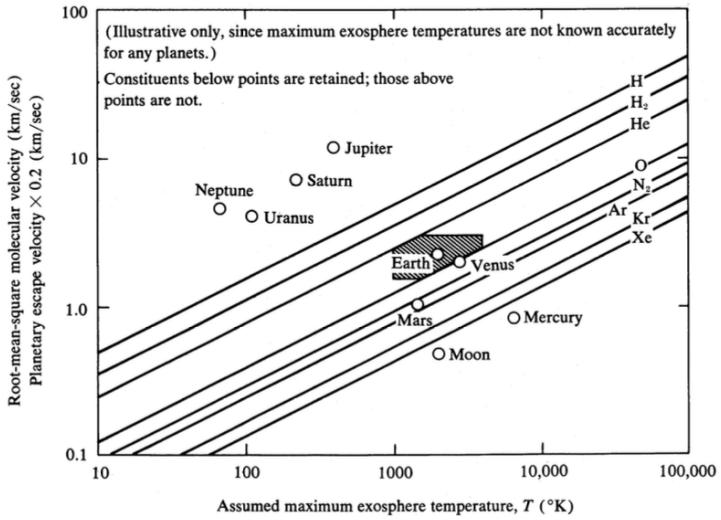

Fig. 1.3 Reproduced from the popular science book *Habitable Planets for Man* (Dole, 1964). In this model, when the root–mean–square thermal velocity of a given molecule at the exobase is at least one–fifth of the planetary escape velocity, the atmosphere is considered liable to rapid Jeans escape. Planets lying above a given molecular line are expected to retain that species, whereas those below are expected to lose it. The Moon and Mercury fall below all lines, consistent with their lack of substantial atmospheres. This early approach invites comparison with the more recent "Cosmic Shoreline" framework (Zahnle and Catling, 2017).

years— where the root-mean-square velocity is one-fifth of the escape velocity. Significantly below the line the upper atmosphere would be in blow-off regime of rapid escape (Öpik, 1963). While above, escape is negligible. As an example, Earth's exobase is observed to vary between 1000 K and 2000 K with the solar cycle, though the box in the figure appears drawn larger. Tian et al. (2008) simulated Jeans escape of nitrogen and oxygen atoms from an expanding Earth-like upper atmosphere under increased ionising irradiation. When XUV heating increases, then the temperature gradient increases and so the extent of the atmosphere grows. The exobase gravitational potential decreases and the thermal energy increases, resulting in a compounded decrease in λ_x and an exponential increase in the Jeans escape rate. Significant escape rates are indeed found for exobase temperatures of several thousand Kelvin as in Fig. 1.3. But also, once XUV irradiation reaches ~ 10× present Earth levels, heating the upper atmosphere to $\lesssim 10^4$K, then the Jeans flux becomes so large that a

hydrostatic solution becomes unstable and the thermosphere collapses into a hydrodynamic outflow (Tian et al., 2008)— then beyond the limits of the model.

In hydrodynamic outflow, the XUV flux $\mathcal{L}_{\rm XUV}/(4\pi a^2)$ is absorbed by an optically thick area πr_{abs}^2 to lift mass at some rate $\Phi_{\rm hyd}$ out of the gravitational potential well GM_p/R_0 with some efficiency η (e.g., Watson et al., 1981):

$$\Phi_{\rm hyd}\frac{GM_p}{r_0} = \eta\cdot\pi r_{abs}^2\frac{\mathcal{L}_{\rm XUV}}{4\pi a^2},$$

where the planet's solid surface radius is r_0, orbiting with semi-major axis a; $\mathcal{L}_{\rm XUV}$ is the star's XUV luminosity with a peak absorption at planetary radius r_{abs}. Thus the rate shifts from a possibly exponential dependence [1] on XUV heating to a roughly linear dependence with some efficiency η.

Watson et al. (1981) considered the energetics of EUV-driven hydrodynamic escape of a primordial hydrogen atmosphere on Earth (see also Sekiya et al., 1980), introducing the energy-limited parametrisation (Eqn 2.6), which has proved remarkably effective across a huge range of conditions. Indeed, a decade after Tian et al. (2008), Johnstone et al. (2019) time-stepped the Euler equations to find a transonic solution for Earth's hydrodynamic thermosphere at XUV fluxes hundreds of times present Earth levels that coincided well with the energy-limit with an efficiency $\eta\sim 1$.

This leads us to the questions of when the energy limit applies and how to evaluate the efficiency of converting XUV heating into escape. For hydrogen atmospheres, quoted heating efficiencies are typically $\eta\sim 0.1$–0.6, but at very high irradiation the flow can become *recombination-limited*, yielding $\dot{M}\propto F_{\rm XUV}^{1/2}$ (Murray-Clay et al., 2009; Owen, 2019). For the outflow of rock vapour atmospheres, Ito and Ikoma (2020) found a very low efficiency $\eta\sim 10^{-4}-10^{-3}$ a modified dynamics but which was still roughly obeyed the equation above.

[1] The exponential onset of rapid escape has since been contested (Johnson et al., 2013a,b). A comprehensive characterisation of the transition from hydrostatic-to-hydrodynamic escape is an open problem.

While Nakayama et al. (2022) found that an Earth-like thermosphere never reaches the hydrodynamic state found in Johnstone et al. (2019) due to efficient cooling from electron-impact excitation of the low-lying electronic states of atoms, meaning the energy-limit may never be reached. Exploring the nuances of the energy-limit for hydrodynamic escape of secondary atmospheres is a key aim of this thesis.

Finally, there has been considerable debate over whether planetary magnetic fields protect Earth from erosion by the solar wind (e.g. Gunell, Herbert et al., 2018; Gronoff et al., 2020a) or suppress hydrogen escape from hot Jupiters (e.g. Owen and Adams, 2014; Khodachenko et al., 2015; Carolan et al., 2021). Yet, the role of magnetic fields in modulating hydrodynamic escape of secondary atmospheres from rocky planets remains largely unexplored.[2] Although Chapter 4 considers the potential importance of planetary dynamos for atmospheric retention, the primary focus of this thesis is on escape in the absence of an intrinsic magnetic field.

1.3 Signals of Exoplanets and Mass Loss

1.3.1 Detection of Exoplanets and their Exospheres

The 2019 Nobel Prize in Physics was shared by Michel Mayor and Didier Queloz for their 1995 discovery of 51 Pegasi b, the first planet detected around a Sun-like star (Mayor and Queloz, 1995). The signal was obtained with the ELODIE echelle spectrograph (Baranne et al., 1996) on the 1.93 m telescope at the Observatoire de Haute-Provence purpose built for the Doppler spectroscopy (radial-velocity) technique that Otto Struve proposed in 1952 (Struve, 1952). The displacement of the centre of mass of an exoplanetary system by a giant

[2]The polar wind may seem, at first glance, like an example, since it is channelled along magnetic field lines. The hydrodynamic aspect of polar wind theory applies primarily to the light-ion component and predicts negligible hydrodynamic escape of heavy ions. Observations, however, show a significant O^+ flux reaching supersonic speeds, requiring non-classical, collisionless acceleration mechanisms (Yau et al., 2007). Moreover, the polar wind is typically modelled in regimes where the atmosphere would not be undergoing global hydrodynamic escape in the absence of a magnetic field.

planet's orbit causes the star to wobble, alternately blue- and red-shfting the light, which yielded a minimum planetary mass for 51 Peg b of roughly half that of Jupiter. Further ELODIE radial velocity data soon helped identify the prototypical transiting "hot Jupiter" HD 209458 b; with a ~ 1.5–2% dimming during transit picked up by the STARE Schmidt Project Camera, giving astronomers both the mass and radius (Charbonneau et al., 2000). The Hubble Space Telescope observed the fingerprint of optical sodium lines in the light filtering through HD 209458 b's atmosphere 160 light-years away to make the first exoplanet transmission spectrum and detection of an exoplanet chemical species (Charbonneau et al., 2002). However, a degeneracy of the Na doublet signal with the Rossiter-McLaughlin transit effect has since been suggested (Casasayas-Barris et al., 2020; Carteret et al., 2024). Soon after, atmospheric loss of hydrogen to the surrounding space was robustly observed through Lyman-α absorption (Vidal-Madjar et al., 2003, 2004). Carbon and oxygen lines in UV were also detected amidst the tenuous gas beyond the Roche lobe; requiring a hydrodynamic mechanism of bulk outflow to drag those heavier molecules out of the gravitational well (García Muñoz, 2007). Finally, HD 209458 b provided the first detection of thermally emitted light from an exoplanet with the Spitzer Space Telescope recording the drop in light due to secondary eclipse (Deming et al., 2005); contemporaneous with a detection from the TrES-1 planetary system (Charbonneau et al., 2005).

We have now encountered the primary exoplanet characterisation methods:

- Primary Transit / Transmission spectroscopy: the wavelength dip in intensity of light in transit can be matched to molecules at the transit radius; star-planet shadow from Fig. 1.4.
- Occultation / Secondary Eclipse: drop due to losing the planets dayside brightness as the planet passes behind star. The drop in brightness at multiple wavelengths will indicated the planet's full thermal emission spectrum.
- Phase Curve of a Full Orbit: both dayside and night side emission with 2D information.

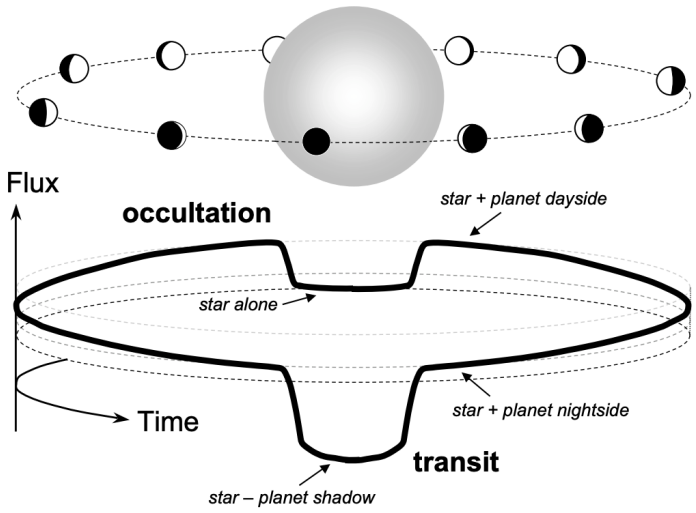

Fig. 1.4 Exoplanet characterisation: a transiting planet passes in front of its star (primary transit), behind the star (secondary eclipse), and through varying orbital phases. Transmission spectroscopy measures wavelength-dependent transit depths to probe atmospheric structure and composition. Emission spectroscopy, via secondary eclipse, measures the planet–to–star flux ratio to infer dayside thermal emission, constraining atmospheric heat redistribution and albedo. Phase curves track the flux ratio over a full orbit, inferring nightside emission and longitudinal temperature structure. Reproduced from Winn (2010).

- A non-transiting planet can be directly imaged or a full optical phase curve can be measured in reflected light from the star.

The amplitude of spectral features scales as

$$\Delta\delta \propto \left(\frac{R_p}{R_\star}\right)^2 \times \begin{cases} \dfrac{H}{R_p}, & \text{(transmission)}, \\ \dfrac{B_\lambda(T_p)}{B_\lambda(T_\star)}, & \text{(emission)}, \end{cases}$$

where R_p and $R_\star$ are the planetary and stellar radii, H is the atmospheric scale height, and $B_\lambda(T)$ is the Planck function at temperature T. Outstanding results from the early characterisation of rocky planets included the phase curves of 55 Cancri e and LHS 3844 b with the *Spitzer* Space Telescope (Demory et al., 2016; Kreidberg et al., 2019). LHS 3844 b exhibits a marked lack of dayside cooling, with no measurable nightside emission. Such

inefficient heat redistribution is best explained by a bare rocky surface or, at most, a tenuous atmosphere; however, interpretations remain somewhat degenerate with assumptions about the planet's surface albedo (e.g., Koll, 2022; Hammond et al., 2025). But the measurement for 55 Cancri e proved less straightforward, with a hot spot offset and variability over many visits, which proves true even today.

For smaller and cooler rocky planets, the best early constraints came from the TRAPPIST-1 System of seven Earth-sized planets locked in a near-resonant chain around an ultracool dwarf star only 12 parsecs away (Gillon et al., 2017). A *HST* transmission revealed a lack of features in the system, ruling out a hydrogen-dominated atmosphere for the innermost planets b and c, at $> 10\sigma$ and the habitable zone planets d, e, f at $4-8\sigma$ (de Wit et al., 2016; de Wit et al., 2018). For constraints on presence of a high molecular weight atmosphere, the community would have to wait until the launch of the *James Webb Space Telescope* in December 2021. However, *HST* continues to provide cutting-edge science results in the UV even three decades after its launch. For example, a marginal detection of an escaping atmosphere from super-Earth π Men c that is dominated by heavy ions— marking a hybrid between a primordial and terrestrial-type atmosphere (García Muñoz et al., 2021).

1.3.2 Radius valley and Rocky Planet Occurrence

Launched in 2009, the Kepler Space Telescope was designed to hunt for small, long-period exoplanets, photometrically monitoring 150,000 stars in a fixed field of view and discovering over 2000 exoplanets. A key discovery of *Kepler* was that around half of Sun-like stars are expected to host a habitable zone rocky planet (e.g., Bryson et al., 2021). Dressing and Charbonneau (2015) further estimated an occurrence rate of 2.5 small exoplanets per M-dwarf, the most common stars. Rocky planets are common and, thus, the possibility that the universe could be teeming with life becomes apparent.

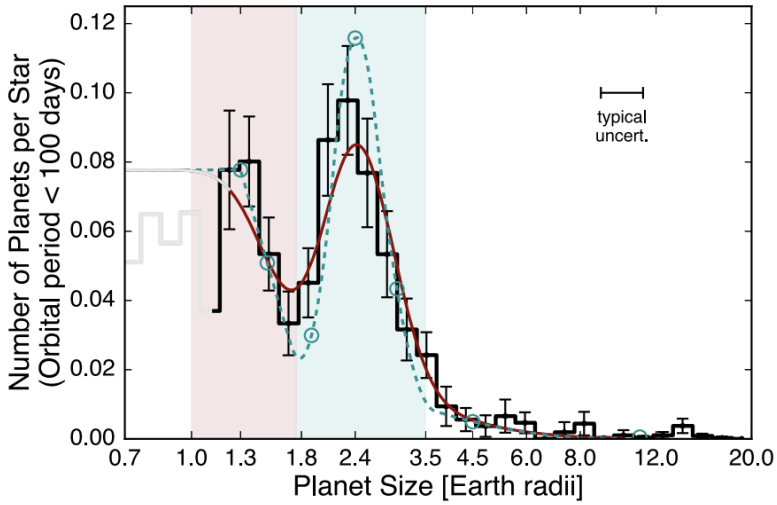

Fig. 1.5 Radius distribution of close-in, low-mass exoplanets. The histogram shows two peaks at ~1.3 $R_\oplus$ and ~2.4 $R_\oplus$, separated by a "radius valley" at ~1.5–2.0 $R_\oplus$. The larger-radius population corresponds to puffy sub-Neptunes; the smaller-radius population to rocky super-Earths. Reproduced from Fulton et al. (2017).

Close-in exoplanets between the size of Earth and Neptune are the most commonly detected and astronomers now have strong evidence that photoevaporation markedly shapes this population (Fulton et al., 2017). Studies predicted that photevaporation over time bifurcates between planets initially with an envelope mass fraction of a few to ten percent, and those with less. Planets with envelopes that double the core fraction are most stable to photoevaporation, with a thinner envelope leading to complete loss and a thicker evolving towards the critical 2 % (Owen and Wu, 2013; Lopez and Fortney, 2013). Fulton et al. (2017) then reported a radius gap, validating the population prediction (see Figure 1.5). Though other factors may be at play, it remains the only mechanism that can explain both the super-Earth and sub-Neptune populations.

For context, out of the 4,467 confirmed exoplanets with measured radii (NASA Exoplanet Archive; August 2025), two thousand (~45%) can be classified as sub-Neptunes (1.75–3.9 $R_\oplus$), one thousand (~25%) as super-Earths (1.1–1.75 $R_\oplus$), and three hundred as approximately Earth-sized or smaller ($R_p \lesssim 1.0\,R_\oplus$). Rogers and Owen (2021) estimate that super-Earths

predominantly formed as sub-Neptunes, at a ratio of 4:1, suggesting that the majority of exoplanets may spend part of their history in a sub-Neptune phase. This inference, however, relies on the strong assumption of a nebular-composition gas envelope, while the true nature of sub-Neptunes remains uncertain. For example, recent observations of the 2.1 $R_\oplus$ planet TOI-270 d (Benneke et al., 2024) reveal a high–molecular-weight atmosphere. Moreover, the most common and readily observed host stars are M dwarfs, and the *Transiting Exoplanet Survey Satellite* (*TESS*) has provided evidence that there may be as many as 14 terrestrial planets for every sub-Neptune on close-in orbits around Mid-to-Late M dwarfs (Ment and Charbonneau, 2023). Nevertheless, gas-rich formation appears to be the rule rather than the exception, implying that inhabited exoplanets – if they exist – may have evolved very differently from Earth.

1.4 The Cosmic Shoreline and JWST

The *cosmic shoreline* hypothesis, proposed by Zahnle and Catling (2013, 2017), posits that a planet's ability to retain an atmosphere [3] is governed primarily by its escape velocity raised to the fourth power in combination with the intensity of incident ionising stellar irradiation : $I_{\mathrm{XUV}} \propto v_{\mathrm{esc}}^4$. In this framework, planets with higher escape velocities are dramatically more effective at holding onto volatiles, while those subjected to stronger irradiation lose them more readily. Crucially, this relationship is proposed to hold across almost four orders of magnitude in escape velocity, from small asteroids to gas giants, and six orders of magnitude in stellar irradiation, demonstrating a remarkable simplicity and unifying principle for atmospheric retention across the full diversity of planetary bodies.

[3] Zahnle and Catling (2017) discuss an alternative "cosmic shoreline" governed by impact erosion. There, typical impact speeds reflect the orbital speed and the additional acceleration from a planet's gravity, so larger escape speeds make for more energetic impacts. Atmospheric loss is expected when impact speeds greatly exceed the escape speed. While impacts and photoevaporation likely act together, the signature of photoevaporation is most prominent in the exoplanet population.

Underpinning this hypothesis is an assumption of indifference to volatile history of planets, whether dominated *primary* (nebular accretion) or *secondary* (outgassing, impacts) atmospheres. The shoreline also neglects the detailed physical models of individual escape mechanisms and their variation, enabling it to become an accessible and central concept to the broad exoplanet community. Indeed, it is reminiscent of Fig. 1.3 (Dole, 1964) but avoids even the model calculation of a maximum exobase temperature.

The James Webb Space Telescope is a 6.5 m infrared observatory at the Sun–Earth L_2 point, passively cooled behind a five-layer sunshield to ~40 K (with MIRI cryogneically cooled to ~7 K) and operating from ~0.6–28.5 μm with exceptionally stable pointing. For rocky exoplanets, NIRSpec, NIRISS/SOSS, NIRCam grisms, and MIRI (LRS/MRS) provide transmission, eclipse, and phase-curve spectroscopy to detect atmospheres via molecular features and thermal emission. The first *JWST* reported observations of the thermal emission of cool rocky planets were for TRAPPIST-1 b and c, revealing no evidence for thick atmospheres (Greene et al., 2023; Zieba et al., 2023). These "null" detections, regarded as disappointing (e.g. Kreidberg, 2023; Witze, 2023), are in fact precisely what both the cosmic shoreline and detailed hydrodynamic escape models would predict. Further observations of joint eclipses, phase curves and transmission spectra confirm the bare rock picture, though uncertainties remain (Ducrot et al., 2024; Gillon, 2024; Radica et al., 2024).

A further six planets have been observed in emission to lack the telltale sign of an atmosphere — dayside cooling due to heat redistribution, so are consistent with bare rocks (Xue et al., 2024; Mansfield et al., 2024; Zhang et al., 2024; Wachiraphan et al., 2025; Luque et al., 2025; Meier Valdés et al., 2025). There have also been the transmission spectra of another six exoplanets that are flat-lines, with the lack of spectral features ruling out thick atmospheres to varying degrees (Lustig-Yaeger et al., 2023; Kirk et al., 2024; Scarsdale et al., 2024; Alderson et al., 2025; Taylor et al., 2025; Piaulet-Ghorayeb et al., 2025). In particular, two transit of TRAPPIST-1 d observed with JWST/NIRSpec PRISM were able to rule out

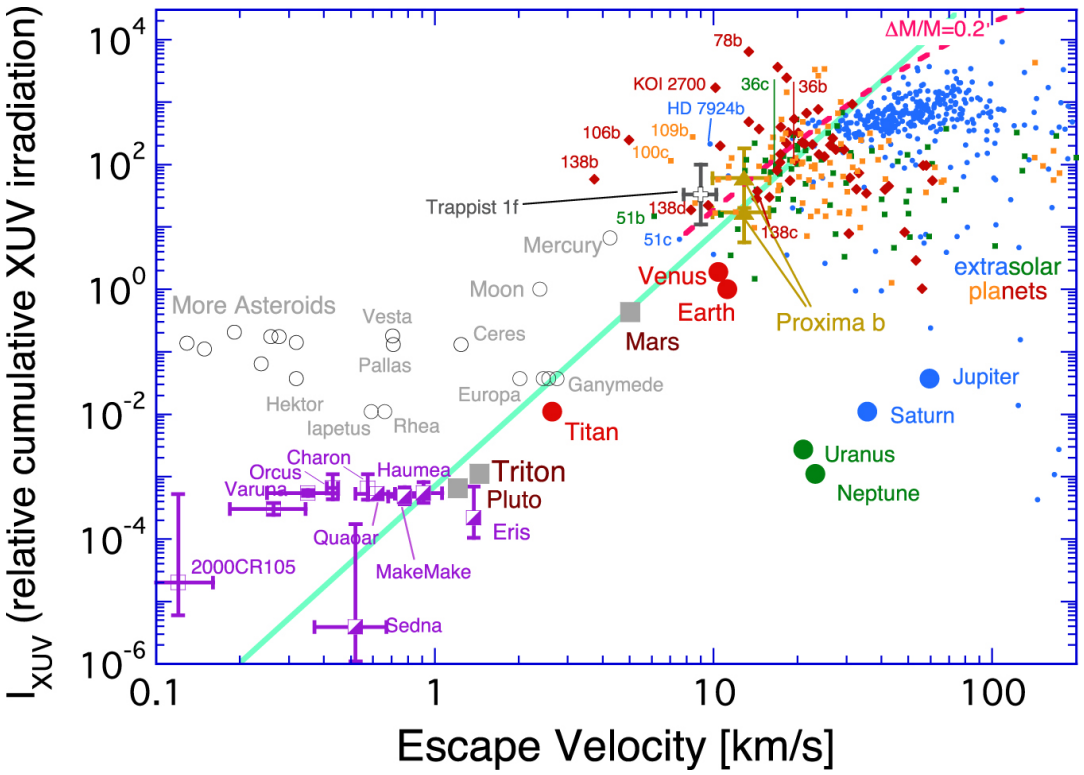

Fig. 1.6 Reproduced from Zahnle and Catling (2017), with an earlier version in Zahnle and Catling 2013. Uses an estimated cumulative XUV irradiation (normalized to Earth) plotted against planetary escape velocity v_{esc}. The solid "cosmic shoreline" (drawn by eye) follows the empirical relation $I_{XUV} \propto v_{esc}^4$, approximately separating planets that retain atmospheres (below/to the right) from those likely airless (above/to the left). Solar System bodies are shown with filled symbols if they have thick (> 1 bar) atmospheres, open symbols if they are airless, and crosses if their atmospheres are thin (< 1 bar). Exoplanets are plotted as coloured symbols (by radius class), while hot, strongly irradiated extrasolar giant planets (EGPs) are additionally compared to a dashed magenta curve indicating energy-limited XUV-driven escape, labelled by the fractional mass lost $\Delta M/M$. Selected exoplanets are annotated for reference.

a range of 1 bar atmospheres (Piaulet-Ghorayeb et al., 2025). In this sense, though each individual result is uncertain, taken altogether *JWST* has delivered a powerful validation of the escape-dominated paradigm.

There are exceptions to this *have-nots* trend with some tentative atmospheric detections announced for super-Earths orbiting mid M-dwarfs, namely L98-59 d (Gressier et al., 2024a; Banerjee et al., 2024) and LHS 1140 b (Cadieux et al., 2024). Tentative features of H_2S and SO_2 were retrieved in L 98-59 d's spectrum (Banerjee et al., 2024), while LHS-1140 b had a spectrum consistent with an N_2 rich atmosphere. However, the coupled-interior atmosphere modelling of Nicholls et al. (2025c) suggested L 98-59 d as a permanently molten sulfur-world, while LHS-1140 b has been suggested to be a water-world (Cadieux et al., 2024), so these may not be recognisably terrestrial. For a terrestrial-type atmosphere, the secondary eclipse of LHS 1478 b, which rules out a dark bare rock to $2-3\sigma$ is the most promising result (August et al., 2024; Connors et al., 2025) and has just been observed across a further five transits (August et al., 2025). While the most intriguing suggestions of atmospheres are those on ultra-short-period lava worlds, including K2-141 b, 55 Cancri e and TOI-431 b (Zieba et al., 2022; Hu et al., 2024; Monaghan et al., 2025).

So far, it has been difficult for the escape modelling community to match the wealth and pace of observations. Much of the key parameter space for photoevaporation-driven evolution of rocky planets is little explored. For example, Nakayama et al. (2022) only consider the effect of atomic line cooling for an Earth-sized planet, exposed to up to 4 Watts per metre squared of XUV flux. While the key parameter space is super-Earths and their aeronomy at even higher XUV fluxes. So, comprehensive attempts at predicting, or even postdicting, these possibly lost atmospheres from first principles modelling is not yet underway. This thesis takes a step forward in filling this gap and will discuss the properties of a range of the rocky planets that already have atmospheric characterisation.

Announced in October 2024, the *Rocky Worlds* Director's Discretionary Time (DDT) programme allocates 500 hours on *JWST* and 250 hours on *HST* to "definitively identify which M-dwarf rocky planets have atmospheres" (Redfield et al., 2024). In addition, the *Charting the Cosmic Shoreline* program (Cycle 4, GO 7073; PI: Lustig-Yaeger) has been awarded 250 hours on *JWST* to obtain transmission spectra of three multi-planet M-dwarf systems with sufficient precision to robustly detect N_2-rich atmospheres. This modern use of discretionary and large-programme time recalls an earlier effort: in December 1995, the Hubble Space Telescope devoted ten consecutive days of DDT to the Hubble Deep Field, producing an image of the most distant galaxies and revolutionising our understanding of the Universe (Williams et al., 1996). What will be the iconic result of today's effort in rocky exoplanet astronomy?

1.5 An Overview of this Thesis

The thesis presents four chapters of original results, outlined below:

Chapter 2 derives and characterises the solution space for escaping planetary atmospheres under a polytropic equation of state, explicitly linking the polytropic index to XUV heating. We show how the Knudsen onset in collisionality uniquely determines the transonic solution, establishing a threshold XUV flux required to sustain predominantly neutral outflow from high mean–molecular–weight atmospheres. This framework is applied to a hypothetical XUV-driven evaporation of nitrogen atmospheres from Earth and Mars in the Sun's active pre-main-sequence.

Chapter 3 adopts a three-level atom model for electron–impact excitation of forbidden lines, exploring its role in the energetics of the neutral Knudsen onset during transonic escape. Building on Nakayama et al. (2022), we assess whether efficient atomic line cooling can protect a hydrostatic atmosphere from instability under rising XUV flux, which increases upper–atmosphere ionisation. This leads to the identification of a global ion outflow regime

for super–Earths, where Coulomb collisions maintain pressure gradients in tenuous flows, and to alternative XUV–flux thresholds set by a collisional–radiative thermostat. After applying this framework to TRAPPIST-1 b and LHS-1140 b/c, we integrate the results into a broader picture of escaping secondary atmospheres and propose a two–branch cosmic shoreline for rocky exoplanets.

Chapter 4 applies the analytic results from Chapters 2–3 (altogether reported in Chatterjee and Pierrehumbert 2024) to the evolution of individual exoplanet systems and the rocky–planet population as a whole. We present new cosmic shorelines that arise directly from our models. These form part of the broader and more comprehensive set published in Ji et al. (2025), which combines our analytic framework with additional modelling approaches.

Chapter 5 shifts focus to the development of numerical tools for simulating subsonic and transonic atmospheric escape. We present and validate a hydrodynamic solver based on the semi-Lagrangian Constrained Interpolation Profile (CIP) algorithm, and introduce molecular–kinetic treatments with the direct simulation Monte Carlo (DSMC) method, including proof-of-concept simulations that bridge collisional and collisionless regimes.

Finally, Chapter 6 summarises the main results and examines their implications for atmospheric loss as a bottleneck to the occurrence of observable Earth-like habitats, placing the findings in the broader context of exoplanetary and astrophysical research.

2

Modelling Escaping Planetary Atmospheres with a Polytropic Structure

This chapter is a modified version of the first half of Chatterjee and Pierrehumbert (2024)

2.1 Introduction

Meeting the conditions for the hydrodynamic escape of secondary atmospheres may divide the airless from the airy rocky exoplanet populations, metaphorically described as the Cosmic Shoreline (Zahnle and Catling, 2017). Secondary atmospheres can form in the continuous transition from an escaping nebular atmosphere, evolve from an initial

high-molecular-weight atmosphere, or be revived by volcanism from a bare rock (e.g., Kite and Barnett, 2020; Krissansen-Totton et al., 2024). We focus on modeling the retention of nitrogen-dominated atmospheres because this is crucial for assessing the potential for Earth-like habitats orbiting M-dwarfs (Lammer et al., 2019). The physics governing the escape of CO_2-dominated atmospheres is similar but differences arise due to infrared cooling lines and photochemistry (e.g., Tian, 2009; Van Looveren et al., 2024). Though some insight can be carried over to the escape of steam-dominated atmospheres, the shift in dynamics due to the hydrogen ions in the upper atmosphere is outside the scope of the present study and we refer the reader to the literature devoted to this topic (e.g., Johnstone, 2020; Yoshida et al., 2022; García Muñoz et al., 2024).

We have already seen how the easier escape of hydrogen compared to nitrogen based on the exobase temperature required for significant Jeans escape (see Fig. 1.3). We can also compare the temperature required at the sonic point r_{sc}, where the velocity must roughly equal half the local escape velocity v_{esc}. So, greater gravitational acceleration $g(r)$ or higher mean molecular mass μ of the flow requires higher atmospheric temperatures because $T_{sc} \propto g(r_{sc}) r_{sc} \mu$. Atmospheric escape from Earth for an atomic nitrogen sonic flow requires a temperature of roughly 15 000 K, while for atomic hydrogen less than 1000 K is sufficient.

So that the pressure gradient force can accelerate an outflow to sound speed, the flow must remain collisional— the exobase should be above the sonic altitude. There is a corresponding threshold in XUV flux to meet this Knudsen onset, which we name after the dimensionless number for collisionality (Knudsen, 1909). This was called the transonic criterion by Johnson et al. (2013a,b), who explored the critical heating with molecular-kinetic simulations, with a focus on heating deposited in a single layer. However with increasing ionization, the rapid Coulomb collisions make the Knudsen-onset less restrictive, leaving other conditions to be satisfied for transonic escape.

Generally, the increase in escape with the higher temperatures generated by an increasing XUV flux limits the ionization fractions in an upper atmosphere. However, ions and electrons can still dominate if XUV heating can be efficiently radiated away. In which case, ambipolar motion will reduce the temperatures required for rapid escape: the Coulomb attraction of the electrons drags out the ions, effectively halving their mean molecular weight and so doubling their scale height (Bauer and Lammer, 2004). Earth's ambipolar electrostatic field was recently measured in-situ for the first time by the Endurance rocket (Collinson et al., 2024). The debated protective effects of planetary magnetic fields are beyond the scope of the present study.

2.1.1 Analytic and Numerical Modeling

Johnstone et al. (2019) time-stepped the discretised multispecies Navier-Stokes Equations with radiative transfer and photochemistry to solve for the steady-state escape of Earth's atmosphere under the raised XUV output of the Young Sun. This approach, henceforth referred to as a hydrocode, is the most comprehensive. However, its conclusions are still vulnerable to neglected physics, which in this case was the forbidden line cooling later found to be important by Nakayama et al. (2022), and the computational expense is prohibitive for broader studies. At the opposite end of complexity, there is the energy-limited parameterization, adapted from Watson et al. (1981), which calculates the mass loss rate via the total XUV heating needed to accelerate atmospheric layers to escape velocity with some fixed efficiency.

The work reported here uses a polytropic approximation for the atmospheric structure to bridge the modeling gap:

$$\left(\frac{\rho}{\rho_0}\right)^{\gamma-1} = \frac{T}{T_0},\ 0 < \gamma \leq \gamma_a, \tag{2.1}$$

comparing the density ρ and temperature T to reference values (ρ_0, T_0), for example, at the thermobase. By varying the polytropic index γ between adiabatic expansion γ_a (e.g.

monatomic $\gamma_a = 5/3$), Parker's isothermal wind $\gamma = 1$, and thermal inversions $\gamma < 1$, we unify a range of idealized planetary outflows. The polytropic equation of state is widely used but is best known for solutions to stellar structure (e.g., Chandrasekhar, 1931). We adopt and generalize results from application of polytropes to the transonic solar wind, including the exact algebraic solution to the dimensionless problem from Holzer and Axford (1970) and extend approximations to the dimensional problem from Lamers and Cassinelli (1999).

The other dimensionless parameter required to define polytropic solutions is the hydrodynamic escape parameter λ_0, which is the ratio of gravitational to thermal energy at the base of the flow. We show that $\lambda_0 \gg 1$ for high-molecular-weight atmospheres allows a priori specification of the sonic altitude and the base-to-sonic ratios of flow properties. Owen and Jackson (2012) use a polytropic model for hydrogen outflow from close-in hot Jupiters with $\lambda_0 \to \infty$ and γ set by the slope of the photoionization equilibrium function. We show how γ determines the profile of local polytropic heating to drive a given steepness of thermospheric inversion and relate γ to the XUV flux given a fixed λ_0. Owen and Jackson (2012) extended their model to an altitude-dependent γ via a pretabulated function; such a formulation may not be possible for metal outflows and is not explored in the present study.

Exploring the transition from subsonic escape with direct simulation of particles (DSMC, Bird, 1994), Johnson et al. (2013a,b) developed an analytic criterion for the minimum XUV heating to drive transonic outflow. We use the Knudsen onset to self-consistently specify a unique transonic γ_{on} polytropic outflow launched from a base characterized by λ_0. We provide analytic expressions for the global thermomechanical efficiency and scale height at the sonic point. The polytropic index γ_{on} yields a threshold XUV flux approximately constrained by a global energy-limit and local heating at the sonic point.

In Chapter 4, we extend this framework to include the atomic line emission (Nakayama et al., 2022), which finds the thermosphere optically thin, so an analytic formulation is still possible with a three-level atom model. When the cooling is found to exceed the polytropic

heating in the Knudsen onset, conditions are not favourable for allowing predominantly neutral outflow, and a further mass loss model is developed based on the action of a collisional radiative thermostat.

2.2 Polytropic model of atmospheric escape

A compressible fluid in 1D requires four equations to solve for four unknowns: transport of mass, momentum, and energy, with an equation of state to calculate density, pressure, velocity, and temperature. The polytropic relation (Eqn 2.3) takes the place of the momentum equation. However, the momentum equation is still key to understanding the flow solution. In this section, we build on previous work to derive an analytic solution space for the structure of escaping atmospheres.

2.2.1 Character of XUV-driven Transonic Expansion into Space

A planetary atmosphere, driven by XUV heating, expands outward from the thermobase, meets the stellar wind, and matches its dynamic pressure, yielding a subsonic breeze with a mass loss rate proportional to the 'inlet-outlet' pressure difference. Continuously reducing the pressure imposed by the stellar wind allows further outward acceleration of the atmosphere driven by the pressure gradient until the flow becomes supersonic at a critical pressure. Once the flow is transonic, the mass loss rate has reached a maximum independent of the upper boundary conditions: any forcing downstream of the sonic altitude cannot influence the upstream flow (Pierrehumbert, 2010b). A subsonic breeze transporting gas up to the exobase is also possible, yielding ballistic escape from a drifting Maxwellian (Volkov et al., 2011).

The spherically symmetric steady compressible Euler Equations admit a range of flow solutions in a point-mass gravitational potential, illustrated in the Mach-radius phase plane

in Figure 2.1. The integral curves of the associated autonomous system form a saddle geometry centred around the sonic point: $\mathcal{M} = 1$, $u_{sc} = \sqrt{fRT_{sc}}$, $r = r_{sc}$, where f is an order unity dimensionless prefactor, and R is the specific gas constant. Under quasistatic variation of the boundary conditions, the time-dependent Euler solution relaxes to the appropriate steady accretion or outflow branches; when no smooth connection exists, Rankine–Hugoniot shocks join the branches (Velli, 1994).

The mass flux of the outflow must be radially uniform, and the momentum equation can then be written as a compressibility-weighted acceleration outwards, provided by a pressure-gradient force split into an adiabatic and a diabatic component:

$$(u^2 - c_a^2)\frac{1}{u}\frac{\mathrm{d}u}{\mathrm{d}r} = \frac{2c_a^2}{r^2}\left(r - \frac{GM}{2c_a^2}\right) - (\gamma_a - 1)4\pi r^2 q_v, \tag{2.2}$$

with radius r, radial velocity u, adiabatic sound speed $c_a = \sqrt{\gamma_a RT}$, net volumetric heating rate q_v, density ρ, and planet mass M.

For volumetric heating prescribed as a function of radius only, the velocity gradient is unbounded where the flow velocity equals the adiabatic sound speed unless the radius satisfies $r_{sc} = GM/2u_{sc,a}^2$. However, $q_v(r)$ is not representative of planetary atmospheres: if the flow is perturbed, the density changes, which would displace the distribution of stellar heating such that heating is implicitly also a function of the velocity gradient. To find the sonic point for $q_v(r, \frac{\mathrm{d}u}{\mathrm{d}r})$ in general, if one exists at all, the energy and momentum equations can be written as an autonomous system of decoupled first-order ODEs (Bauer and Carter, 2021). The central reduction of the present study is to an approximately polytropic atmospheric structure, given by

$$\left(\frac{\rho}{\rho_0}\right)^{\gamma-1} = \frac{T}{T_0},\ u_{sc} = \sqrt{\gamma RT_{sc}}\ \&\ r_{sc} = \frac{GM}{2u_{sc}^2}. \tag{2.3}$$

This equation generalises from the $\gamma = \gamma_a$ adiabatic expansion to a polytropic expansion where $0 < \gamma < \gamma_a$, corresponding to implicit inclusion of distributed heating given by

$$q_\gamma \cdot 4\pi r^2 \rho = \Phi_{\rm hyd} \cdot \left(\frac{\gamma_a}{\gamma_a - 1} + \frac{\gamma}{1-\gamma} \right) R \frac{{\rm d}T}{{\rm d}r}, \tag{2.4}$$

where $\Phi_{\rm hyd}$ is the mass loss rate and q_γ is the polytropic model's implicit specific heating per unit mass. The polytropic solution ($\Gamma = \gamma$) will be consistent with a diabatic (γ_a, q) solution at each altitude:

$$\Phi_{\rm hyd} \cdot \frac{\rm d}{{\rm d}r} \left(\frac{u^2}{2} + \frac{c_\Gamma^2}{\Gamma - 1} - \frac{GM}{r} \right) = \begin{cases} 4\pi r^2 \rho q & : \Gamma = \gamma_a \\ 0 & : \Gamma = \gamma, \end{cases} \tag{2.5}$$

if $q = q_\gamma$. The differently framed flows have the same velocity and gravitational potential but different internal energies. The physical interpretation of Eqns (2.4 & 2.5) is that the total heating in each local spherical shell drives the transport of specific internal energy at each altitude. The shift of the saddle point from the adiabatic u/c_a to the polytropic Mach number u/c_γ is due to a regularising perturbation from the imposition of polytropic heating, as the temperature becomes implicitly dependent on the velocity gradient through the implicit heating. This shift in the sonic point is comparable to that from conduction regularization (e.g., Hong et al., 2014). Note that the classic analytic solution of the isothermal Parker Wind also requires implicit heating to accelerate the flow, which the XUV section of stellar irradiation often provides.

A hydrodynamic upper atmosphere, not limited by the supply of the escaping component from the lower atmosphere, will often escape limited by the energy input (e.g., Watson et al., 1981). The absorbed stellar XUV lifts gas out of the planet's gravitational well with an efficiency η:

$$\Phi_{\rm hyd} \frac{GM_p}{r_0} = \eta \cdot \pi r_{abs}^2 \frac{\mathcal{L}_{\rm XUV}}{4\pi a^2}, \tag{2.6}$$

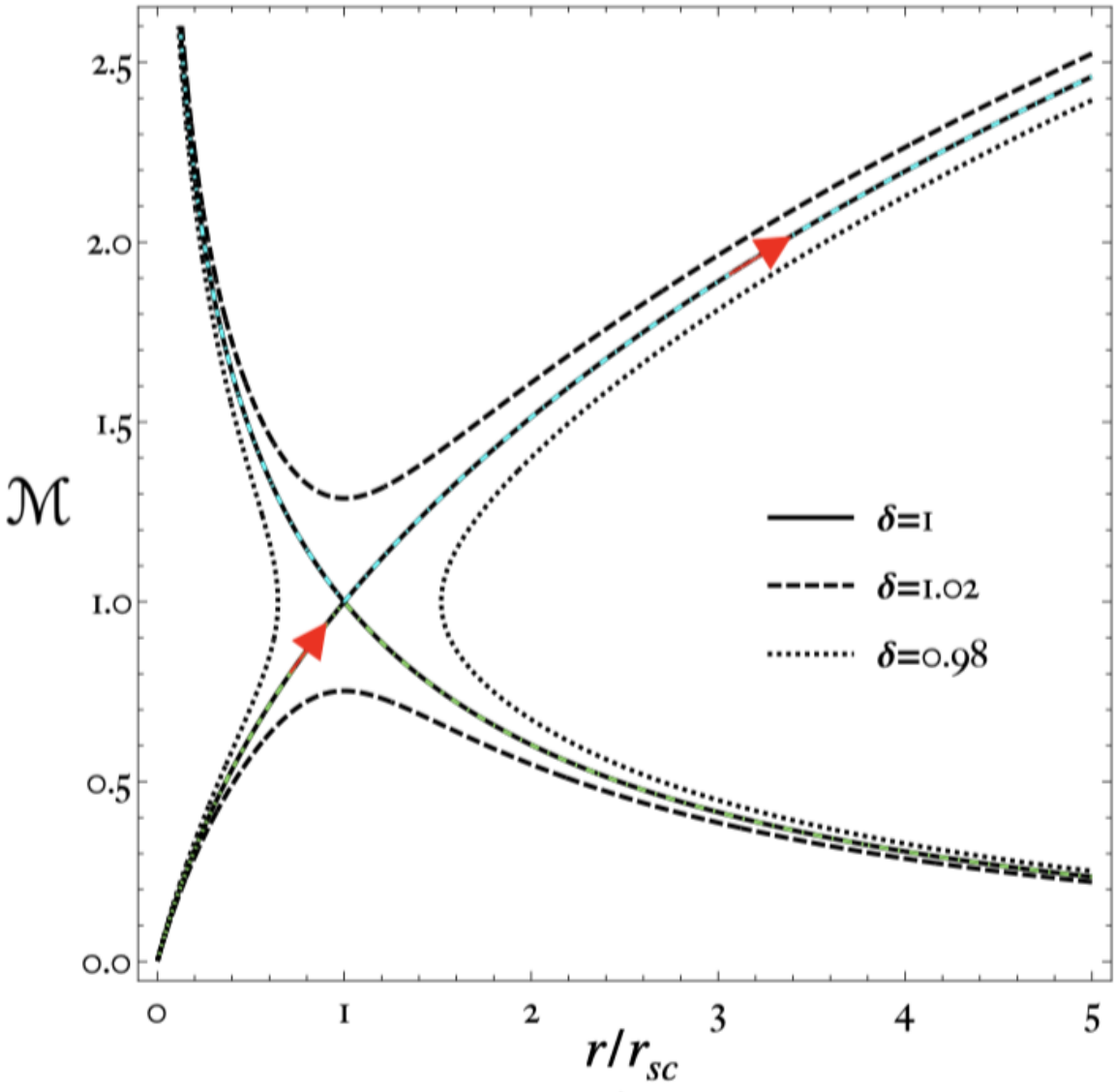

Fig. 2.1 Contour plot of Mach number $\mathcal{M}$ against dimensionless radius r/r_{sc} for a diatomic adiabatic expansion ($\gamma_a = 1.4$) example solutions: transonic ($\delta = 1$), subsonic/supersonic ($\delta = 1.02$), and double-valued ($\delta = 0.98$). The transonic escape solution is highlighted with red arrows. The transonic contours' upper and lower branches are highlighted with a dot-dashed line of cyan and green, respectively. δ relates to the entropy differences between different types of solutions (see Eqn 2.10).

where the planet's solid surface radius is r_0, orbiting with semi-major axis a; $\mathcal{L}_{\rm XUV}$ is the star's XUV luminosity with a peak absorption at planetary radius r_{abs}. In the energy-limited parametrization, a physics-based derivation of η and r_{abs} is neglected. We address two of the major limitations of the energy-limited parametrization (Gronoff et al., 2020b) by evaluating the escape regime via the Knudsen onset and evaluating the atmospheric profiles with polytropic solutions. For hydrogen escape, an alternative prescription for advancing beyond the ELP used a grid of hydrocode models to construct fits for mass loss rates (Kubyshkina et al., 2018).

The present study breaks down the efficiency η into a product of the thermomechanical, photoreaction and cooling efficiencies:

$$\eta = \eta_\gamma \eta_{\rm pr} \eta_{\rm c}, \tag{2.7a}$$

$$\eta_\gamma \approx \frac{2\gamma r_{sc}}{r_0}\left(\frac{\gamma_a}{\gamma_a - 1} + \frac{\gamma}{1-\gamma}\right)^{-1} \tag{2.7b}$$

The thermo-mechanical η_γ efficiency of polytropic escape is derived by integrating the implicit heating up to the sonic point (Eqn 2.4) and comparing to the heating needed to lift the mass out of the gravitational well. The thermal energy at the base is neglected, so Equation (2.7b) is approximate, but an exact comparison as a function of the boundary conditions is straightforward. The photoreaction efficiency accounts for the excess energies of photoionization and photodissociation. The cooling efficiency represents how much of the available XUV-heating is converted into line cooling from the thermosphere, which will be explored in Section 3.3.

2.2.2 Polytropic Approximation to Atmospheric Structure and Escape

Polytropic atmospheric structure spans a range of idealized hydrostatic and hydrodynamic vertical equilibria. Holzer and Axford (1970), following on from the work of Parker, provided

an algebraic solution to the dimensionless problem for the polytropic solar wind. Our work extends the calculation to solve the dimensional problem, folding it into the framework for high-molecular-weight transonic escape of planetary atmospheres. Conservation of mass and the Bernoulli equation for energy link the sonic flow properties to the rest of the flow as:

$$\rho u r^2 = \rho_{sc} u_{sc} r_{sc}^2, \tag{2.8a}$$

$$\frac{u^2}{2} + \frac{c^2}{\gamma - 1} - \frac{GM}{r} = \left(\frac{5-3\gamma}{\gamma-1}\right)\frac{u_{sc}^2}{2}, \tag{2.8b}$$

where we have simplified the energy at the sonic point using Equation (2.3). This pair of equations can be expressed in terms of two unknowns, the Mach number $\mathcal{M} = u/c_\gamma$ and dimensionless radius $\xi = r/r_{sc}$, yielding

$$\left(\frac{c^2}{u_{sc}^2}\right)^{\frac{\gamma+1}{\gamma-1}} \mathcal{M}^2 \xi^4 = 1, \tag{2.9a}$$

$$\frac{c^2}{u_{sc}^2}\left(\frac{\mathcal{M}^2}{2} + \frac{1}{\gamma-1}\right) = \frac{1}{2}\left(\frac{5-3\gamma}{\gamma-1}\right) + \frac{2}{\xi}. \tag{2.9b}$$

To find the implicit algebraic solution, $\frac{c^2}{u_c^2}$ can be eliminated from Equation (2.9b) by substitution of Equation (2.9a). The governing equation

$$2\delta\left(\frac{1}{\gamma-1} + \frac{\mathcal{M}^2}{2}\right)\left(\mathcal{M}^2\right)^{-\frac{\gamma-1}{\gamma+1}} = \left(\frac{5-3\gamma}{\gamma-1} + \frac{4}{\xi}\right)\xi^{4\left(\frac{\gamma-1}{\gamma+1}\right)} \tag{2.10}$$

can be found numerically as a contour, where the transonic outflow is selected from amongst accretion and multivalued solutions (Fig 2.1) via specifying a constant of integration $\delta = 1$ (Holzer and Axford, 1970). Related to entropy, we have reinserted δ so that Equation (2.10) is in its most general form[1]. The form of solution mirrors the isothermal Parker Wind, except that most scientific computational libraries have a pre-tabulated function for the Parker

[1]
$$\delta = \exp\left(\frac{2\gamma}{\gamma+1}\frac{s - s_{sc}}{c_p}\right) \tag{2.11}$$

contours, called the Lambert W-Function (Cranmer, 2004). Equation (2.10) also recovers the isothermal solution in the limit $\gamma \to 1$ with the Bernoulli definition of the exponential; see discussion of Equation (2.21).

The above solution for the Mach profile is the seed for the solution to all other profiles. To calculate the dimensionless temperature, conservation of mass (Eqn 2.9a) can be used directly. The temperature profile can be fed into the polytropic relationship (Eqn 2.3) to determine the dimensionless density profile. Lastly, a combination of the temperature and Mach number profiles yields the dimensionless velocity profile via energy conservation (Eqn 2.9b).

The hydrodynamic escape parameter is defined as the ratio of gravitational energy to thermal energy at the base of the flow (e.g., Watson et al., 1981):

$$\lambda(r_0) = \lambda_0 = \frac{GM}{RT_0 r_0} \tag{2.12}$$

and is the other dimensionless parameter for the polytropic model. We will refer to an escape temperature analogous to the concept from protoplanetary disc photoevaporation (e.g., Owen and Jackson, 2012). It is defined as the temperature necessary at some altitude for the isothermal sound speed to equal half the escape velocity, or equivalently, $\lambda(r) = 2$:

$$T_{\rm esc}(r) = \frac{\mu}{4k_B} v_{\rm esc}(r)^2. \tag{2.13}$$

At the escape temperature, the sonic point of an isothermal hydrodynamic flow would be reached (Pierrehumbert, 2010a), while if the top of a hydrostatic atmosphere were at this temperature it would collapse into a blow-off state (Öpik, 1963). Moreover, if the temperature at the exobase is a half to a third of the escape temperature, a hydrostatic equilibrium would be unstable and expand hydrodynamically (Tian et al., 2008).

Although these profiles can hypothetically be calculated for a planetary atmosphere with any (γ, λ_0), for a well-behaved steady-state solution, the planetary wind should launch highly subsonic. Thus, the $\mathcal{M}^2$ term in energy conservation can be neglected to provide a simple approximation for the sonic radius, where

$$\xi_0 \approx \frac{\frac{4\gamma}{\lambda_0} - 4(\gamma - 1)}{5 - 3\gamma} = \xi_0^{\mathrm{itr},1}, \tag{2.14}$$

specifying the dimensional profile and collapsing the degeneracy in the sonic point through a single iteration in the first approximation $\xi_0^{\mathrm{itr},1}$ (Lamers and Cassinelli, 1999). In the context of flows which start with appreciable Mach numbers, one can find the ${\mathscr{M}^2}_{\mathrm{itr},1}$ via the Equations (2.14 & 2.10), to find the second approximation, given by

$$\xi_0^{\mathrm{itr},2} = \frac{\frac{4\gamma}{\lambda_0}\left(\frac{1}{2}{\mathcal{M}^2}_{\mathrm{itr},1} + \frac{1}{\gamma - 1}\right) - 4}{\frac{5-3\gamma}{\gamma-1}}. \tag{2.15}$$

This allows full specification of, for example, adiabatic diatomic expansion, usually after only one iteration. The equations for the sonic point radius can be compared to Equation (13) from Owen and Jackson (2012), which assumed $\gamma < 1, \lambda_0 \to \infty$.

Neatly, the approximate mass flux can be found immediately using the first iteration (Eqn 2.14) - without needing to compute the contour. The mass loss rate, given by $4\pi\rho u r^2$ and expressed in terms of γ, λ_0 and the lower boundary, becomes

$$\Phi_{\mathrm{hyd}} = 4\pi\rho_0 r_0^2 \left(\frac{v_{\mathrm{esc}}(r_0)}{2}\right)\left(\frac{\lambda_0}{2\gamma}\right)^{1/(\gamma-1)}\left(\frac{4\gamma/\lambda_0 - 4(\gamma-1)}{5-3\gamma}\right)^{\frac{5-3\gamma}{2(\gamma-1)}}. \tag{2.16}$$

which has also been applied to stellar winds (Lamers and Cassinelli, 1999). Lastly, Equation (2.14) allows simple determination of all sonic-to-base ratios for flow launching highly

subsonic:

$$\frac{T_{sc}}{T_0} = \frac{\lambda_0 \xi_0}{2\gamma}, \tag{2.17a}$$

$$\frac{\rho_{sc}}{\rho_0} = \left(\frac{T_{sc}}{T_0}\right)^{1/(\gamma-1)} \tag{2.17b}$$

$$\frac{u_{sc}}{u_0} = \frac{\rho_0}{\rho_{sc}} \xi_0^2. \tag{2.17c}$$

For tightly bound atmospheres, where $\lambda_0 \gg 1$, and $\gamma < 1$, $1/\xi_0$ is of order unity and the term with the strongest dependence on γ arises from the density (see Eqn. 2.17b). On varying γ, the mass loss rate and the fuel required from XUV heating, thus scale as $\propto \lambda_0^{1/(\gamma-1)}$. In general, however, the XUV flux cannot be directly inferred from γ, because both dimensional parameters and the non-linear dependence on λ_0 play significant roles. The broader landscape of γ is examined in more detail in Figures 2.2 and 3.6.

2.2.3 Polytropic Solution Space

Figure 2.2 presents the solution space of vertical equilibrium for polytropic atmospheres. We devote significant discussion to the space of regions in (γ, λ_0) so that Figure 2.2 can be used as a touchpoint to understand idealized solutions to escape. It is instructive to follow the thermodynamic expansion of a parcel lifted through the atmosphere.

For $\lambda_0/\gamma > 1/(\gamma-1)$, the sum of the thermal energy at the base with the integrated heating is insufficient to give the parcel enough energy to escape the planet's gravitational well so that the atmosphere will be hydrostatic. An air parcel will cool as it rises, and its density will tend to zero on reaching a finite terminus of the atmosphere. The cooling will be less for $\gamma \to 1$, where $\gamma < \gamma_a$ entails implicit heating throughout the atmosphere. The pink region of Figure 2.2 thus marks where only a finite hydrostatic atmosphere is consistent.

Moving leftwards, the blue region $\lambda_0/\gamma < 1/(\gamma-1)$ in Figure 2.2 marks where transonic escape solutions exist, and finite hydrostatic atmospheres are inconsistent. There are no

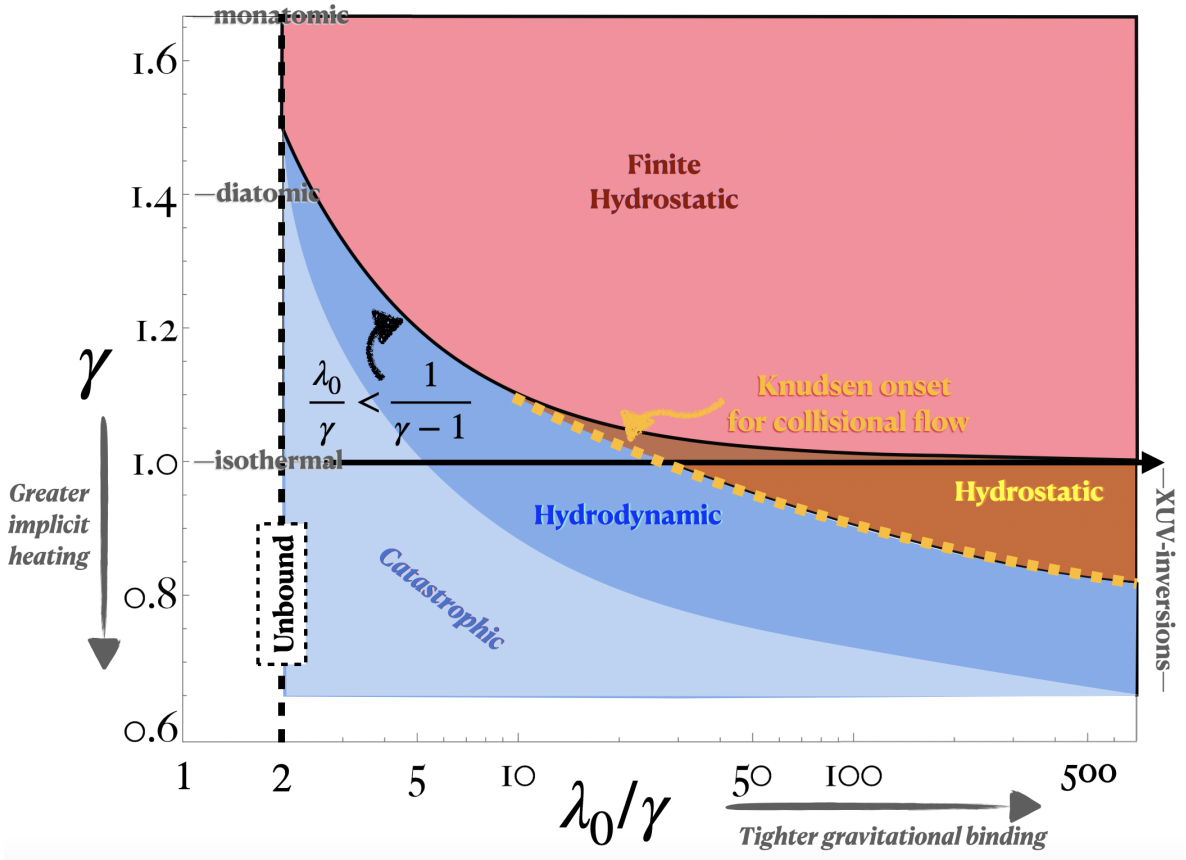

Fig. 2.2 Steady-state polytropic solutions space for vertical atmospheric equilibrium. For $\frac{\lambda_0}{\gamma} > \frac{1}{\gamma-1}$, the equilibrium is hydrostatic with density reaching zero at a finite height (pink). Implicit heating throughout the atmosphere reduces γ from an adiabat γ_a. For $2 < \frac{\lambda_0}{\gamma} < \frac{1}{\gamma-1}$, the thermal energy at the base in addition to the implicit heating is large enough to drive an accelerating transonic flow in principle (blue hydrodynamic region). The supersonic at the base constraint $\lambda_0 = 2$ is represented by the dashed vertical line and labelled 'unbound'. The blue region of consistent steady state does not extend all the way to this line, however, because the flow launch should have $\mathcal{M} \ll 1$, otherwise the escape is 'catastrophic' (light blue). On failure of the hydrodynamic assumption at the sonic point, XUV-driven inversions ($\gamma < 1$) give way to hydrostatic atmospheres that would be infinite except for the formation of an exobase (brown region). The yellow line is then the Knudsen onset for collisional flow given by $\mathrm{Kn}_{sc}^{\mathcal{N}} \sim 1$ (see Section 2.3).

consistent hydrodynamic escape solutions for $\gamma > 3/2$, as such flows would be decelerating from the base and only preserve uniform mass transport outwards because the spherical surface area increases with the radius. The $\gamma = 1.4$ diatomic adiabatic expansion permits an accelerating transonic solution with an unrealistic velocity profile. The near field limit $\xi \ll 1$ of Equation (2.10) combined with Equation (2.9a) yields $u_0/u_{sc} \approx 1.3\sqrt{\mathcal{M}_0} = \sqrt{2\xi_0}$, so that even as far out as $r_{sc} = 40r_0$, which allows $\mathcal{M}_0 = 1/20$, the sonic velocity is only $3\times$ the base velocity in the diatomic case. Then, the atmosphere above the base is lost on the timescale of days.

Reducing γ down towards 1 through the implicit imposition of heating allows the flow to be driven from a lower temperature base and for acceleration to sonic velocity orders of magnitude greater than base velocity, yielding loss timescales for the thermosphere on a timescale of thousands of years or more. Replenishment of the thermosphere by the lower atmosphere enables a quasi-steady-state hydrodynamic escape solution that evolves over a loss timescale of about a million years, with atmospheric pressure either decreasing or being maintained by outgassing.

In an isothermal expansion $\gamma = 1$, the gas does work but heat flows in to keep the temperature the same. For $\gamma < 1$, a rising parcel heats as it expands up a thermospheric inversion due to the implicit heating outweighing adiabatic cooling. The model mass loss then increases linearly with the XUV flux, apart from a small variation in the thermomechanical efficiency, consistent with the energy limit.

Two exceptional regions show where mass loss is catastrophically fast in light blue and where the hypothetical flow becomes collisionless before reaching sound speed in brown. The catastrophic region begins where an atmosphere would be unbound at $\lambda_0 \leq 2$. Even for higher λ_0, increasing XUV flux reduces γ so that sound speed is reached in a dense layer (Eqn 2.17b), yielding too-rapid mass loss for a valid steady state of a planetary atmosphere. In the limit of large λ_0, a hydrodynamic atmosphere would find the exobase below the hypothetical

sonic altitude. The Knudsen onset (yellow-line), which will be discussed in detail in the following section, entails a minimum steepness of polytropic inversion $\gamma_{\rm on}$, which must be generated by a threshold XUV flux to drive transonic hydrodynamic escape.

2.2.4 Lower Boundary Conditions

The role of lower boundary conditions varies with the polytropic index. For adiabatic thermally driven escape, any gas at the bottom of the potential well has enough thermal energy to escape, so the mass loss is set by the base density. Similarly, isothermal planetary winds are set by lower-boundary assumptions with large uncertainties and degenerate scenarios arise; see core-powered mass loss (e.g., Tang et al., 2024). Steep inversions ($\gamma < 1$) are the only analytic solutions that are consistent with the dynamics of the energy limit. The densities in the flow (base or sonic) are restricted to yield a mass loss less than the XUV heating available. We adopt mesopause-like densities for the lower boundary of secondary atmospheres. We note that a spectrum richer in shorter wavelengths will launch the flow from deeper into the atmosphere, all else being equal. As will be discussed in Section 2.3.4, when the base density is varied by an order of magnitude, the profiles are only moderately sensitive, and the mass loss rate is quite insensitive, remaining within the error already anticipated by the analytic approximation.

2.3 XUV-flux Threshold for Transonic Escape

In this section, we will calculate whether there is an onset of transonic escape of hypothetical nitrogen atmospheres from Earth and Mars on ramping up XUV insolation to that experienced in the early pre-main sequence. Given best estimates of lower boundary conditions, we derive how imposing a Knudsen number equal to one at the sonic point specifies a unique polytropic solution to atmospheric escape. The corresponding threshold in XUV flux to

drive the transonic outflow defines a conservative regime of applicability for energy-limited parametrization. Our ansatz is predominantly neutral outflow with XUV heating fueling advection. In Sections 3.2 & 3.4 we will relax these assumptions.

2.3.1 Knudsen Onset

A Knudsen number equal to one at the sonic point will specify the escape of a polytropic atmosphere sustainable for an XUV flux that defines an energetic threshold for transonic escape. The Knudsen number (Knudsen, 1909) describes the collisionality of a flow, which is calculated for an atmosphere as the ratio of the mean free path to the local scale height of the atmosphere. We derive the scale height using L'hopital's rule for the sonic velocity gradient (Lamers and Cassinelli, 1999), then substitute into the radial derivative of equation (2.8a), to yield

$$\left[\frac{1}{\rho}\left(\frac{\mathrm{d}\rho}{\mathrm{d}r}\right)_{sc}\right]^{-1} = -\frac{(1+\gamma)r_{sc}}{4+\sqrt{2}\sqrt{5-3\gamma}}. \tag{2.18}$$

The mean free path is the average distance a particle will travel before its next collision. It can be calculated as the reciprocal of the product of the collision cross-section σ_C and the number density up to a factor of order unity. Thus, the Knudsen number in the polytropic model can be expressed as

$$\mathrm{Kn}_{sc} = \frac{4+\sqrt{2}\sqrt{5-3\gamma}}{\sqrt{2}(1+\gamma)\sigma_{\mathrm{C}}\cdot n(r_{sc})\cdot r_{sc}} \tag{2.19}$$

The model exobase separates a collisional thermosphere below (Kn < 1) from the collisionless exophere above (Kn > 1). We compare our criterion for transonic escape with the numerical and analytic calculations of Johnson et al. (2013a) in Section 2.4. We note that Owen and Jackson (2012) found ballistic escape from some more massive Hot Jupiters on the basis of non-existence of a collisional sonic point but did not explicitly relate this to their polytropic model or XUV flux.

The Knudsen onset for transonic escape should be taken with two caveats:

1. Collisionality increases with greater ionization due to the greater cross-sections of ion-atom charge exchange and high-frequency atom-electron collisions. To establish a general method to calculate the onset of transonic escape, we choose to work with the neutral onset $\mathrm{Kn}_{sc}^{\mathcal{N}} \sim 1$, using the neutral collision cross-section $\sigma_{\mathrm{C}}^{\mathcal{N}}$; reasonable when advection-dominated and weakly ionized.

2. In a bulk outflow, the nominal exobase forming before the hypothetical sonic point is consistent with the upper boundary fulfilling the flux constraints of a drifting-Maxwellian Jeans escape (Volkov et al., 2011; Erwin et al., 2013). The energy limit might apply for $\mathrm{Kn}_{sc} \in [1,3]$, or extend even further (Johnson et al., 2013a), but characterizing the non-linear transition requires both DSMC and hydrocode modeling, so it is beyond the scope of the present study.

Thus, for characterizing rapid mass loss, the neutral onset is highly conservative.

The crux of the polytropic framework is to estimate the threshold XUV flux needed to drive (Eqn 2.4) transonic hydrodynamic escape for atmospheres of varying gravitational binding and composition. Temperatures and ion production should not be so extreme that line-cooling chokes off the flow, which will be discussed in Section 3.2. The onset XUV flux is determined by the mass loss rate (Eqn 2.16) for the polytropic atmosphere γ_{on} where $\mathrm{Kn}_{sc} = 1$:

$$F_{\mathrm{XUV}}^{\mathrm{on}} = \frac{\Phi_{\mathrm{hyd}}(\gamma_{\mathrm{on}}; \lambda_0, r_0, n_0, \mu, \sigma_C^{\mathcal{N}})\, v_{\mathrm{esc},0}^2}{2\pi r_{abs}^2 \eta_\gamma \eta_{\mathrm{pr}} \eta_{\mathrm{c}}}, \tag{2.20}$$

mediated by the thermomechanical efficiency η_γ (Eqn 2.7b), the photoreaction efficiency η_{pr} and the cooling efficiency η_{c}. The greater the collisionality required at the sonic point, the smaller γ_{on} becomes, with the XUV flux rising proportionally with the mass loss rate beyond the onset values.

To find γ as a function of Kn_{sc}, we substitute the sonic-to-base density ratio (Eqn 2.17b) into Equation (2.19):

$$\frac{(1+\gamma)(5-3\gamma)\lambda_0}{4(4+\sqrt{2}\sqrt{5-3\gamma})(\gamma-\lambda_0\gamma+\lambda_0)}\cdot\left(\frac{(5-3\gamma)\gamma}{2\gamma+2\lambda_0(1-\gamma)}\right)^{1/(1-\gamma)}-\left(\sqrt{2}\mathrm{Kn}_{sc}\sigma_{\mathrm{C}}n_0r_0\right)^{-1}=0, \quad (2.21)$$

which defines a dummy function ψ, such that the neutral onset is given by $\gamma_{\mathrm{on}} = \psi\left(\mathrm{Kn}_{sc}=1;\lambda_0,r_0,n_0,\sigma_C^{\mathcal{N}}\right)$. The parameters after the semicolon in ψ are specified as constants for a particular planetary atmosphere in a given regime. We can use the original Bernoulli definition of the exponential $\lim_{j\to\infty}\left(1+\frac{x}{j}\right)^j = \mathrm{e}^x$, to recover the isothermal limit, of Equation (2.21) with $j = 1/(1-\gamma)$

$$\lim_{j\to\infty}\left(\frac{1+\frac{3}{2j}}{1+\frac{\lambda_0}{j}}\right)^j \propto \frac{\lambda_0}{6}\cdot\mathrm{e}^{3/2-\lambda_0} = \left(\sqrt{2}\mathrm{Kn}_{sc}\sigma_{\mathrm{C}}\cdot n(r_0)\cdot r_0\right)^{-1}, \quad (2.22)$$

where the derivation requires Taylor expansion of the denominator. We note that the isothermal solution restricts Kn_{sc} to be specified by the lower boundary conditions. In the polytropic framework, given the best-estimate base density and neutral cross sections, γ_{on} is found implicitly through Equation (2.21) and selects the contour for the atmospheric structure (Eqn 2.10). The corresponding flux is given by Equation (2.20), with a further estimate needed for the absorption radius.

The underlying equations (2.20–2.21) should be approximately consistent with local heating rates, especially at the sonic point. Assuming the flow at the sonic point is optically thin to incoming XUV, a physical estimate of XUV heating per unit mass at the sonic point is

$$\overline{q_{sc}} \approx a_\theta \sum_\lambda \eta_{pr}(\lambda)F_{\mathrm{xuv}}(\lambda)\sigma_\lambda/m, \quad (2.23)$$

where m is the atomic mass, σ_λ and $\eta_{pr}(\lambda)$ are the photoabsorption cross-section and photoreaction efficiency as a function of wavelength (e.g., Huebner and Mukherjee, 2015).

The prefactor a_θ is equal to unity if consider the heating at the substellar point, or equal to cos(66°) to account for global averaging of the XUV flux Johnstone et al. (2019). The polytropic model heating per unit mass at the sonic point is given by

$$q_{sc,\gamma} = \left(\frac{\gamma_a}{\gamma_a - 1} + \frac{\gamma}{1-\gamma}\right) \frac{4 + \sqrt{2}\sqrt{5-3\gamma}}{(1+\gamma)\cdot(1-\gamma)^{-1}} \frac{RT_{sc}u_{sc}}{r_{sc}}, \tag{2.24}$$

calculated from substituting the sonic density temperature gradient, found by chain rule from Equation (2.18), into Equation (2.4). Again, the isothermal limit of $q_{sc} = 3u_{sc}^3/r_{sc}$ can be recovered. The XUV flux found by matching Equation (2.23) with (2.24) will not necessarily agree with the onset flux (Eqn 2.20). There is broad agreement in the cases we explore; however, the atmospheric structure can be useful regardless. We will now discuss the physical inputs for Equation (2.20).

2.3.2 Photoevaporation of Nitrogen Thermospheres by Active Stars

Differential rotation in a star's convective envelope generates a magnetic field that confines and heats coronal plasma to millions of kelvin, resulting in XUV emission from metal lines and the free-free continuum. Stars are initially saturated in X-ray emission relative to bolometric luminosity, later losing angular momentum through magnetic breaking of the stellar wind until converging onto a main-sequence activity track for a given mass (Vilhu, 1984). Depending on the initial rotation rates of F, G, and K stars, their saturated phase lasts around 10 – 300 million years, compared to billions of years for the lower mass M-dwarfs due to their persistently long convective turnover timescale (Johnstone et al., 2021).

The evolution of the Sun's XUV flux at 1 AU (Catling and Kasting, 2017; Ribas et al., 2005) is given by

$$F_{\rm xuv}(\tau_{\rm age}) \approx 23.3 \times 10^{-3} {\tau_{\rm age}}^{-1.23}\ \mathrm{W\ m^{-2}}, \tag{2.25}$$

where $\tau_{\rm age}$ is in GYrs, $F_{\rm XUV,\oplus} \approx 4 \times 10^{-3}\,{\rm W\,m^{-2}}$. The XUV flux in the Sun's early pre-main-sequence is then $F_{\rm XUV}(\oplus, 0.1\ {\rm GYr}) \approx 0.4\,{\rm W\,m^{-2}} \approx 100 F_{\rm xuv,\oplus}$, but could have been several times higher if initial rotation was rapid (Johnstone et al., 2021). Variability in the solar cycle leads to a factor of 2 difference between the EUV of the quiet and active Sun (Huebner and Mukherjee, 2015). Turning to a $0.09 M_\odot$ M-dwarf, the XUV flux at TRAPPIST-1 b (0.011 AU) during its early pre-main-sequence may have been $\gtrsim 10^4 F_{\rm XUV,\oplus}$ and today it is $\sim 10^3 F_{\rm XUV,\oplus}$ (Fleming et al., 2020). While for the M-dwarf super-Earths LHS 1140 c (0.027 AU) and LHS 1140 b (0.09 AU) the XUV fluxes today are approximately $100\times$ and $10\times F_{\rm XUV,\oplus}$, with b currently in the habitable zone (Spinelli et al., 2023; Cadieux et al., 2024).

At the base of the thermosphere, photodissociation of dinitrogen produces atomic nitrogen that is advected upwards, while N_2 is replenished from the lower-atmosphere reservoir. For an energy-limited onset we expect that photoionization of atomic nitrogen is balanced by the advection of ions downstream along a gradient of increasing ionization fraction. Ion-electron recombination plays a minor role in these conditions (see Sec 3.2). The flow accelerates sharply, with density dropping to keep mass flux roughly uniform. We expect a relatively sharp N_2/N front followed by an extended N/ N^+ front up to the sonic point where, with onset XUV fluxes, the ionization fraction should remain minor, as is found in Johnstone et al. (2019).

The reaction pathways for XUV absorption are summarized in Table **??**, with data from Huebner and Mukherjee (2015). Photodissociation to neutral atoms does not efficiently heat the thermosphere because absorption is constrained by the potential energy of bound states of dinitrogen (e.g., Heays et al., 2017). To find the global efficiency of heating by photoreactions, when ion-electron recombination and dissociative recombination of nitrogen are low, one can make the approximation that every two atoms lost must have come from a photodissociation event and every ion lost from a photoionization event. Thus, weighting the average excess energies, the global photoreaction heating efficiency is

Table 2.1 Nitrogen Photoabsorption Reactions

Photoreaction	ΔE (eV)	λ_v (nm)	Excess energy (eV)	η_{pr}
$N_2 + \gamma \rightarrow N_2^+ + e^-$	15.7	79.2	21.4	0.58
$N_2 + \gamma \rightarrow N + N$	12.5	99.2	3.38	0.21
$N_2 + \gamma \rightarrow N^+ + N + e^-$	24.4	25.0	32.4	0.57
$N + \gamma \rightarrow N^+ + e^-$	14.6	85.1	19.0	0.57
$N^+ + \gamma \rightarrow N^{2+} + e^-$	29.2	42.5	17.3	0.37

Note: ΔE & λ_v are the threshold energy and corresponding wavelength of incoming EUV photons for the given pathway. The excess energy is the average photon energy above the dissociation or ionization threshold and has been calculated in the Modern Solar Spectrum in a period of high activity with data taken from PHIDRATES Huebner and Mukherjee (2015). The photoreaction efficiency η_{pr} is calculated as excess energy divided by the sum of excess energy and threshold energy.

$\eta_{pr}(f_+^{sc} = 0.1) \approx 0.21 + 2 \times 0.1 \times 0.57 \approx 1/3$, where f_+ is the ionization fraction. For comparison, this photoreaction efficiency is approximately equal to the EUV heating efficiency found by France et al. (2020) for typical Earth-Sun conditions. We note that the efficiency of the *local* heating at the sonic point is determined by excess photoionization energy only, yielding $\eta_{pr,sc} \approx 0.6$.

Oxygen has a lower dissociation energy than nitrogen, with absorption extending in the UV to ~200 nm. The model of Johnstone et al. (2019) includes UV in their XUV spectrum, tripling the energy available in their $\approx 60 F^*_{\mathrm{XUV},\oplus}$. Focusing attention on a pure nitrogen atmosphere allows us to safely neglect detailed photochemistry and means the XUV spectrum mostly overlaps with that driving hydrogen escape. Apart from order unity variation in efficiency, the polytropic heating is agnostic to what composes the XUV spectrum, so fluxes quoted in Wm^{-2} are unaffected. However, the dynamics of oxygen line cooling compared to nitrogen is more heterogenous so we will make direct comparison in Section 3.2.

The neutral collision cross-section given by $\sigma_C(\mathrm{N-N}, 10^4\ \mathrm{K}) = 3.9 \times 10^{-20}\ \mathrm{m}^2$ (Kislyakova et al., 2019). Charge-exchange is effective enough that even for a weakly ionized plasma, it could more than double the total cross-section: $\sigma_C(\mathrm{N-N+}, 10^4\mathrm{K}) = 5 \times 10^{-19}\ \mathrm{m}^2$ (Laricchiuta et al., 2009). The electron-neutral cross section can be found somewhere inbetween

$\sigma_C(\mathrm{N}-\mathrm{e}^-, 10^4\ \mathrm{K}) = 2\times10^{-19}\ \mathrm{m}^2$. For a species mixture, an effective collision cross-section against the bulk density can be considered:

$$\sigma_{\mathrm{C}} = \sum_k \frac{n_k \sigma_{k,\mathrm{C}}}{n}. \tag{2.26}$$

Considering an ionization fraction ~ 0.1 we find $\sigma_C(\mathrm{N}-\mathrm{all}, 10^4\ \mathrm{K}) = 1.1\times10^{-19}\ \mathrm{m}^2 \sim 3\times\sigma_C^{\mathrm{N}}$.

2.3.3 Young Sun Earth

This section presents a model of the Knudsen onset transonic outflow of Earth's atmosphere prescribed to be pure nitrogen, which may have been energetically feasible in the raised XUV output of the Young Sun. Though the Early Earth is thought to have had a CO_2-rich atmosphere (e.g., Lammer et al., 2018), nitrogen's role in habitability makes this an interesting exo-Earth scenario. Somewhat coincidentally, the escape rate of the Johnstone et al. (2019) hydrodynamic simulations of Young Sun Earth turns out to be close to the neutral onset that we here derive from the polytropic framework, offering the opportunity for intercomparison of atmospheric profiles. Though we note that the collisional onset within the hydrocode model could be different, depending on collision cross-section, the scale height and definition of the sound speed.

The lower boundary is set to a thermobase-like altitude of 75 km with an inventory of $10^{15}\mathrm{cm}^{-3}$ nitrogen atoms and a temperature of 250 K, yielding $\lambda_0 = 416$ noting $M_\oplus$ =5.97 × 10^{24} kg and $R_\oplus$ =6.378 × 10^6 m (equatorial). Calculated with Equation (2.21), the neutral onset $\gamma_{\mathrm{on}} = 0.77$ provides enough implicit heating for the scale height to develop such that the outflow remains collisional out to the sonic point. This corresponds to almost 9 orders of magnitude change in number density from the base to the sonic radius (Fig 2.3). The sonic radius is calculated as 2.9× the planetary radius (Eqn 2.14), or at an altitude of approximately 12 200 km. The temperature monotonically increases to 23 300 K at the sonic radius, yielding a sonic-to-base temperature ratio of 93× (Eqn 2.17a). The velocity is

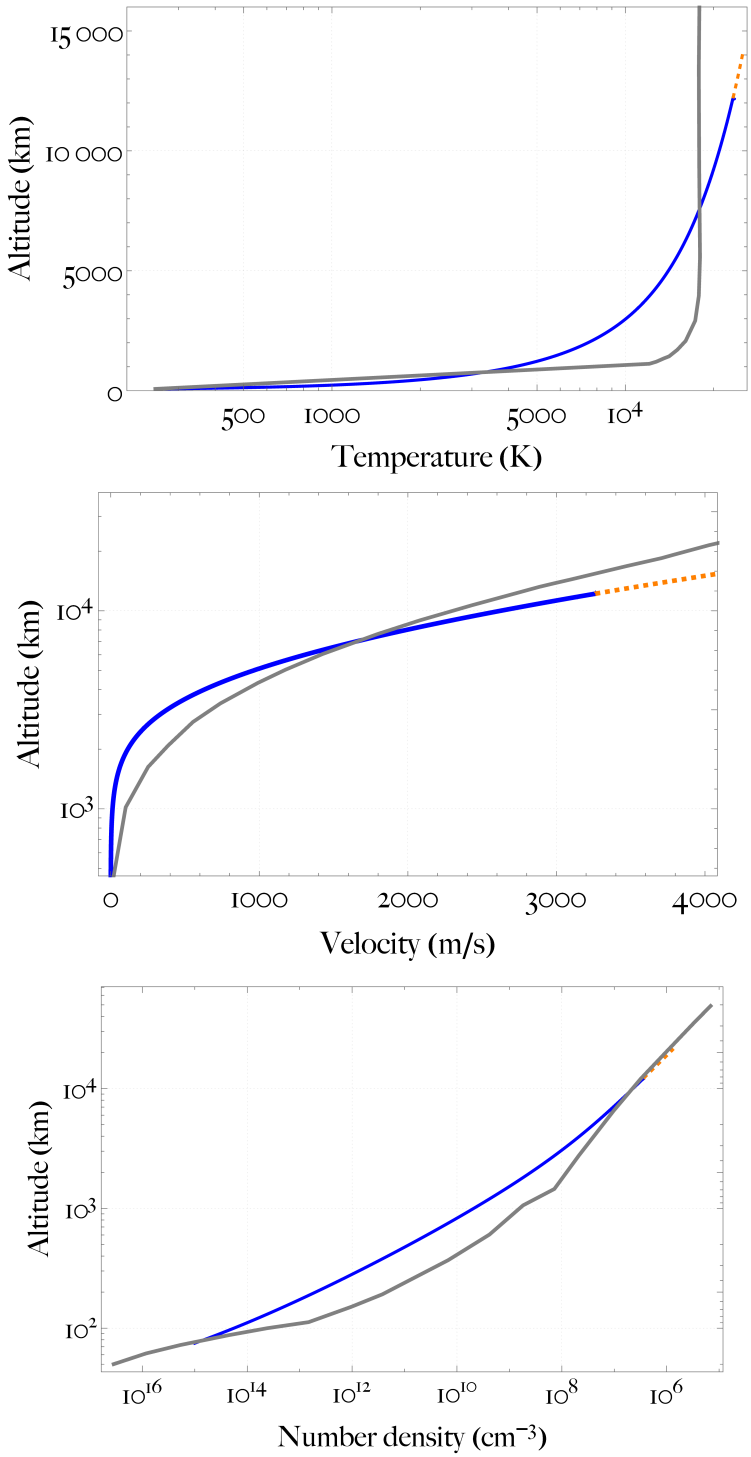

Fig. 2.3 The polytropic onset solution $(\lambda_0, \gamma_{\rm on}) = (416, 0.77)$ for the temperature, velocity and number density profiles (blue) for an Earth-like planet hosting a pure nitrogen thermosphere. The dashed-orange line begins at the sonic level $r_{sc} \approx 2.9 R_\oplus$. The hydrocode profiles from Johnstone et al. (2019) are presented for comparison in grey. The XUV flux required to drive the transonic hydrodynamic escape is estimated $F^{\rm on}_{\rm XUV}({\rm YSE}) \approx 0.84\,{\rm W\,m^{-2}}$, or equivalently, $\gtrsim 200 F_{\rm XUV,\oplus}$.

inappreciable until a couple of thousand kilometers in altitude before rising steeply to the sonic speed at $3.3\,\mathrm{km\,s^{-1}}$ — the total change in Mach number is seven orders of magnitude. Past the sonic radius, a dashed line shows a continuation of the polytropic solution for each profile in Figure 2.3. However, the behaviour and forcing downstream of the sonic point do not affect the mass loss rate or the atmospheric structure upstream.

The polytropic model for Young-Sun Earth onset (Eqns 2.16 & 2.21) yields a mass loss rate of $1 \times 10^9\,\mathrm{g\,s^{-1}}$ or 4×10^{31} atoms/s. Based on this rate, six bars of an N_2 atmosphere could be lost in a million years. As noted by Johnstone et al. (2019), the discussion of fluxes is always up to an order unity factor as studies use different averaging conventions and a range of spectral models. The flux-receiving cross-section has a larger area than the projected surface of the planet (πR_{pl}^2) - larger due to heating being significant out to a few planetary radii. We approximate the geometric factor $R_{abs} = \sqrt{2}R_{pl}$ (Eqn 2.6) following Catling and Kasting (2017). We also account for the thermomechanical efficiency of the hydrodynamic expansion $\eta_{0.77} \approx 0.76$ and the efficiency of heating via photoelectrons $\eta_{pr} \approx 1/3$. Altogether, we find the flux incident on the sub-stellar column needed to trigger the onset of transonic hydrodynamic escape (Eqn 2.20) to be $F_{\mathrm{XUV}}^{\mathrm{on}}(\mathrm{YSE}) \approx 0.84\,\mathrm{W\,m^{-2}}$, equivalent to $\gtrsim 200 F_{\mathrm{XUV},\oplus}$. However, a subsonic onset of bulk outflow may be possible for fluxes an order of magnitude lower $\sim 20 F_{\mathrm{xuv},\oplus}$. Accounting for the uncertainty in the initial rotation rate of the Sun (Johnstone et al., 2021) and neglecting non-LTE cooling for now, the transonic escape of a thick secondary atmosphere during the saturated phase is plausible.

The $\gamma_{\mathrm{on}} = 0.77$ mass loss rate happens to be $1/2\times$ the rate in Johnstone et al. (2019), so broadly similar profiles might be expected. Figure 2.3 displays the curves calculated with `KOMPOT` from Johnstone et al. (2019) for comparison. A limitation of the polytropic models is the neglecting of the photodissocation front, instead considering an inventory of nitrogen atoms. Consequently, the mean molecular weight in the first few scale heights can be underestimated to as low as half of its true value. However, the steeper-then-flatter pattern

converges to a similar density where the polytropic atmosphere goes sonic to within a factor of two. The temperature profiles are similar, but the comparison highlights how the single polytropic index γ cannot account for the differential steepness in the middle and upper atmospheres, namely the photodissociation heating peak is neglected. Furthermore, the sustained temperature inversion for $\gamma = 0.77$ results in an increased sonic temperature. The velocity profiles are comparable, though the hydrocode-calculated acceleration is greater than the polytropic near the base and lesser at the sonic point.

Altogether, the polytropic approximation naturally produces, without fitting, profiles that bear key similarities to a detailed hydrocode solution (Johnstone et al., 2019) at a similar XUV flux. Had we attempted an isothermal Knudsen onset (Eqn 2.22), we would have faced the (λ_0, n_0) degeneracy, or the problem of how to choose the sonic radius. For the thermobase density of 10^{15}cm^{-3}, the isothermal Knudsen onset (Eqn 2.22) would find an almost unrecognizable solution: $r_{sc} = \frac{\lambda_0}{2} R_{pl} \approx 11 R_{pl}$, $T \approx 4100$ K — leading to a mass loss rate about 5× higher than the polytropic case. Though reducing the base density of the Parker wind would allow a hotter and less extended outflow to maintain $\text{Kn}_{sc} = 1$, one must then use ad hoc fitting to produce a realistic profile.

2.3.4 Young Sun Mars

ollowing the last section, we now present a model of evaporation of a nitrogen from Mars in the raised XUV output of the Young Sun. Early Mars may have had more than 0.1 bars of nitrogen (Hu and Thomas, 2022). However, our primary motivation is to gain insight into exo-Mars planets and the landscape of high molecular weight escape. Follow-up work of coupling the polytropic model to a chemical kinetics code with a CO_2 photochemistry network is in progress (Blumenthal et al., in prep).

For a base temperature 200 K, noting $M = 6.39 \times 10^{23}$ kg and $R = 3.39 \times 10^6$ m (equatorial), the escape parameter for Mars is $\lambda_0 = 105$. For a thermobase inventory of 10^{14} cm^{-3} nitrogen

atoms, Equation (2.21) yields $\gamma_{\rm on} = 0.826$. Reducing the base temperature from 200 K to 150 K increases $\lambda_0 = 140$ and a steeper inversion of $\gamma_{\rm on} = 0.80$ is required to remain collisional out to the sonic point. On the other hand, increasing the base density to 10^{15} cm^{-3} allows a less steep inversion of $\gamma_{\rm on} = 0.86$. For $\gamma_{\rm on} = 0.826$, the sonic radius is 3.5× the planetary radius or at an altitude of approximately 8500 km (Fig 2.4). The temperature monotonically increases to 3600 K at the sonic radius, yielding a sonic-to-base temperature ratio of 18×.

The indicative Young-Sun Mars transonic onset (Eqn 2.20) yields a mass loss rate of 3×10^8 g s^{-1} or 1.3×10^{31} atoms per second or 2 bars of N_2 per million years. Using the same efficiency factors as from the Earth model, the flux incident on the sub-stellar column $F^{\rm on}_{\rm XUV}({\rm YSE}) \approx 0.2\,{\rm W\,m^{-2}}$, equivalent to $\gtrsim 50 F_{\rm XUV,\oplus}$ or 100× Modern Day Mars XUV. The sonic temperatures in the $\gamma_{\rm on} = 0.80$ and $\gamma_{\rm on} = 0.86$ cases are 3100 K and 4200 K, respectively. The resultant difference in mass loss is less than 10 % due to the square-root dependence of the sonic velocity on temperature, showing a relative insensitivity to the lower boundary conditions. While for the isothermal Knudsen onset, if we halve the (base) temperature, the sonic radius doubles, the mass loss rate increases by $\sqrt{2}$, and the ratio of base-to-sonic density is increased orders of magnitude by a factor of $e^{2r_{sc}/R_{pl}}$.

Tian et al. (2009) found hydrostatic instability and rapid escape of a CO_2 atmosphere on Early Mars for ~ 20× Modern Day Mars XUV. However, this is not inconsistent with the higher XUV required for transonic onset reported here because subsonic outflow could be driven at those lower fluxes. In conclusion, the hypothetical transonic loss of a nitrogen atmosphere from Mars in the saturated phase of the Young Sun would have been possible. Furthermore, the atmosphere of an Exo-Mars in the Habitable Zone of an M dwarf is not expected to survive on geological timescales.

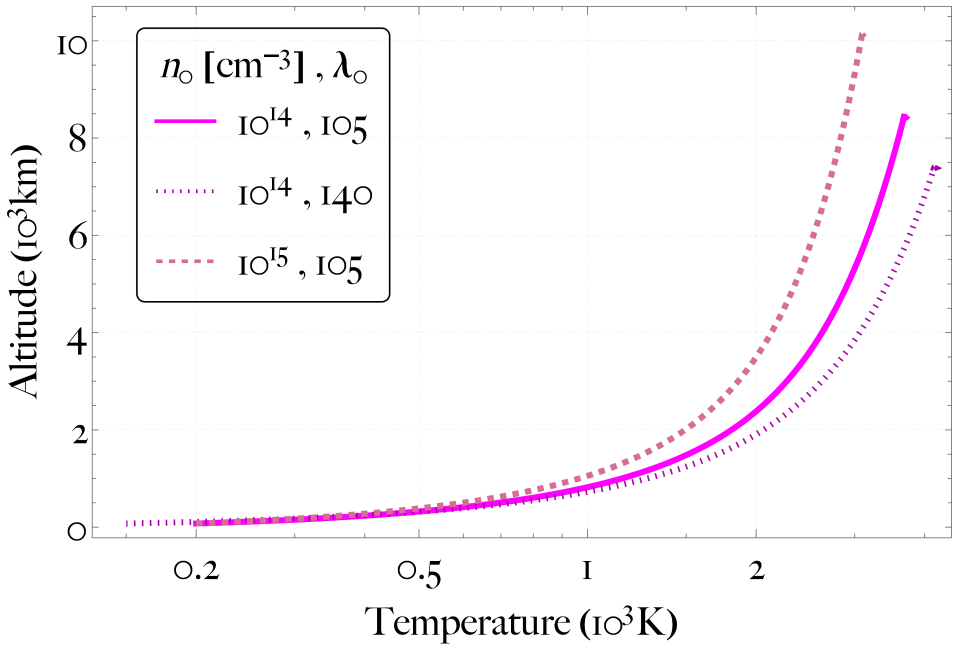

Fig. 2.4 Temperature profiles for hypothetical nitrogen escape from Young-Sun Mars $(T_0, n_0, \lambda_0, \gamma_{on}) = (200\,\mathrm{K}, 10^{14}\,\mathrm{cm}^{-3}, 105, 0.826)$ (solid), $(150\,\mathrm{K}, 10^{14}\,\mathrm{cm}^{-3}, 140, 0.8)$ (dashed), $(200\,\mathrm{K}, 10^{15}\,\mathrm{cm}^{-3}, 105, 0.86)$ (dotted).

2.4 Comparison with Johnson et al. (2013a,b)

The analytic transonic criterion of Johnson et al. (2013a) was employed by Gronoff et al. (2020b) to evaluate the propensity for atmospheric escape across a survey of planets. Notably, the Direct simulation Monte Carlo models from Johnson et al. (2013a) suggest that the energy-limited mass loss rate applies well at onset and for a range of subsonic flow at smaller XUV fluxes. However, (Johnson et al., 2013a) explore a limited set of assumptions and regimes, so determining the general extent to which the energy limit remains valid before transitioning non-linearly to a roughly Jeans-type escape remains a key unresolved question in the field. On comparing Equation (2.20) with "Equation (10)" from Johnson et al. (2013a), we see that each calculation estimates the total net heating required to drive transonic outflow at an order-unity Knudsen number at the sonic point. For Young-Sun Earth, Johnson et al. (2013a,b) identify the transonic onset at $\gtrsim 100 F_{\mathrm{XUV},\oplus}$, consistent with

our results. The polytropic model presented here further enables analytic determination of the sonic scale height and velocity, as well as evaluation of the thermomechanical and line cooling efficiency from the atmospheric structure. We also incorporate a critical estimate for the photoreaction efficiency factor of a nitrogen atmosphere (see Table **??**). In the next chapter, we refine the transonic criterion by analyzing the breakdown of neutral Knudsen-onset assumptions with high escape temperatures and efficient atomic line cooling.

3

The Role of Atomic Line Cooling in Escaping Secondary Atmospheres

This chapter is a modified version of the latter part of Chatterjee and Pierrehumbert 2024.

3.1 Introduction

The photoevaporation of secondary atmospheres represents a novel astrophysical regime in that it is a 'metal' flow— not dominated by hydrogen. The hydrodynamic escape of hydrogen atmospheres has been observed from Hot Jupiters since Vidal-Madjar et al. (2003, 2004) and theoretical modelling was used to predict the bimodality in the radius distribution of sub-Neptunes (Owen and Wu, 2013; Lopez and Fortney, 2013; Fulton et al., 2017). For

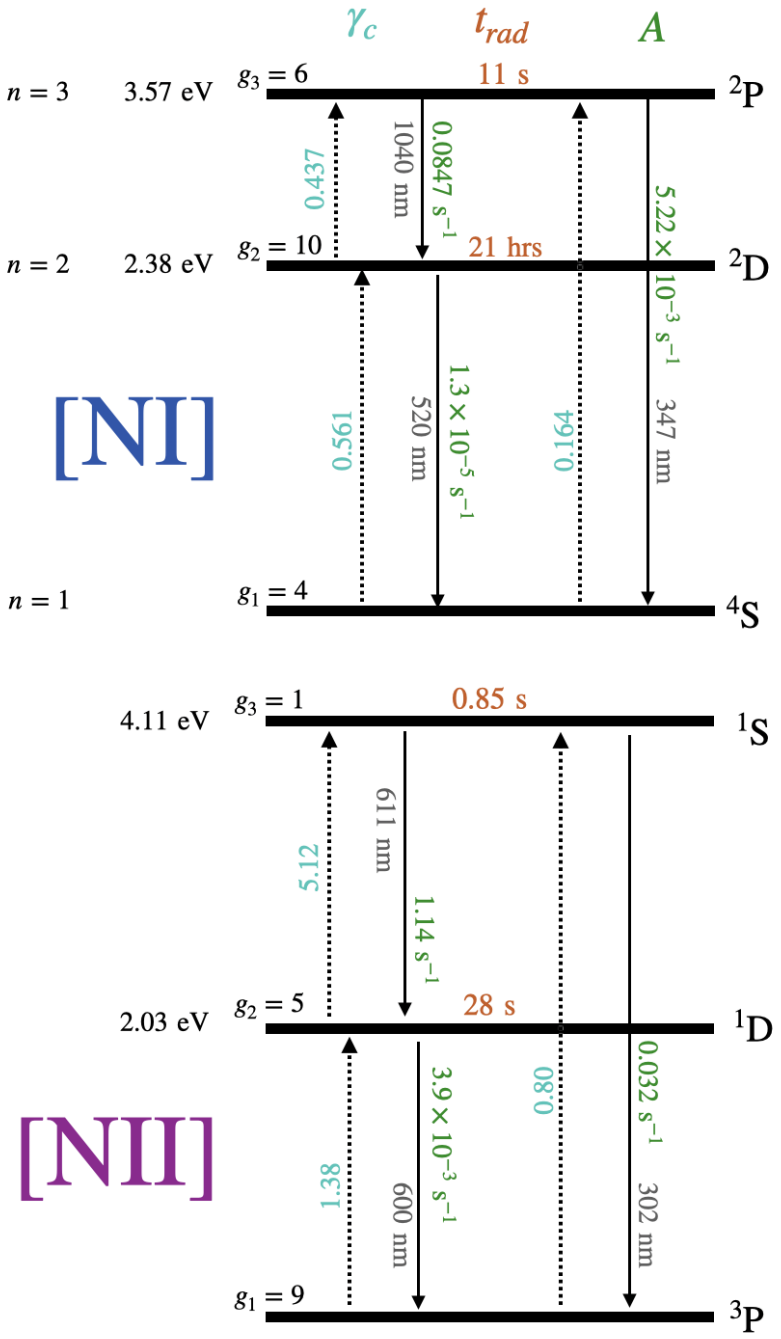

Fig. 3.1 Grotrian level diagram for the first three levels of neutral and singly ionised nitrogen. The coefficients for the collsional excitation γ_C, the radiative lifetime of the level t_{rad} and the transition Einstein-A from Nakayama et al. (2022) are displayed.

evaporation of hydrogen envelopes from close-in giant planets, XUV heating competes with cooling from electron-impact excitation of the $HI_{Ly\alpha}$ emission from 10.2 eV above ground and by radiative recombination of ions with electrons (e.g., Murray-Clay et al., 2009).

Groundbreaking simulations by Nakayama et al. (2022) demonstrated that cooling via collisional excitation of the metastable states of N, C, and O—each with excitation energies around 1 eV to 4 eV, making them more accessible than $HI_{Ly\alpha}$—was sufficient to maintain temperatures low enough for an Earth-like atmosphere to remain hydrostatic under 1000× current Solar XUV flux. Their inclusion of efficient atomic cooling revised the resistance of Earth's atmosphere to XUV-driven hydrodynamic escape by orders of magnitude (Tian et al., 2008) and offers more favorable prospects for Earth-sized exoplanets orbiting M-dwarfs retaining atmospheres. However, the present study reports that the assessment of Jeans escape by Nakayama et al. (2022) to determine hydrostatic instability only partially accounts for the increasing ionization of the neutral exobase and neglects the eventual supplanting by the ion-exobase.

We also note that consistency of the unexplored hydrodynamic equilibrium is not necessarily mutually exclusive with a consistent hydrostatic equilibrium as they occupy different regimes: ionization-recombination and ionization-advection balances, respectively. The work reported here first explores predominantly neutral hydrodynamic escape before introducing a new regime of global ion outflow controlled by a collisional-radiative thermostat. This thermostatic feedback, which can be inferred from the simulations of Nakayama et al. (2022), can be compared to that due to line cooling of minor-abundance metals in a photoionisation-equilibrated hydrogen flow such as found in stellar winds (Drew, 1985), planetary nebula (Seaton, 1960) and even galaxy clusters (Ferland et al., 2009).

3.2 Accounting for Non-LTE Cooling

The previous section discussed the conditions required for the transonic escape of secondary atmospheres for Mars-to-Earth-sized planets while neglecting the effects of forbidden line cooling. We will now test the primacy of atomic line cooling in the evolution of secondary atmospheres found by Nakayama et al. (2022), but for the hydrodynamic rather than hydrostatic regime. We introduce the simplifying approximation of a three-level model of electron-impact excitation of forbidden lines that cool directly to space. The non-LTE radiative transfer of molecular lines, shown to be important in escaping steam atmospheres (García Muñoz et al., 2024), is not discussed here.

3.2.1 Three-level Model for Electron Excitation of Atomic Lines

The polytropic framework admits atomic and molecular cooling estimates diagnosed from the atmospheric structure. For a polytropic solution to represent a consistent, steady state, the line cooling rate per unit mass should be lower than the polytropic heating throughout the extent of the atmosphere. The total line cooling luminosity informs the efficiency factor for the energy limit. Collisions between atoms, molecules, electrons, and ions excite vibrational, rotational modes, and electronic states, which can be relaxed by further collisions or by spontaneous emission of light. Electronic states are available to ambient temperatures of 0.1 eV to 1 eV, equivalent to 10^3 K to 10^4 K, or greater. In Local Thermodynamic Equilibrium (LTE), the photons are honorary gas particles, meaning that the local emission per unit mass depends only on a single temperature field and is independent of local densities. Maintained by collisions, the well-known Boltzmann formula gives the population ratio between levels j and i: $\frac{n_j}{n_i} = \frac{g_i}{g_j} \exp\{-E_{ji}/k_B T\}$, where E_{ji} is the excitation energy, g_i, g_j are the level density of states and k_B is the Boltzmann constant (e.g., Feynman et al., 2011). The resulting

volumetric cooling rate from some level j to a lower level i via spontaneous emission is given by $Q_{ji} = \frac{n_i g_i}{g_j} \exp\{-E_{ji}/k_B T\} A_{ji} E_{ji}$.

Atomic excitation is dominated by electron impacts because electron thermal velocities are $\sim \sqrt{m_i/m_e}$ (≈ 160 for N) times larger than ion velocities, fast enough to produce sudden (non-adiabatic) excitation of bound electrons (Hertel and Schulz, 2015). In contrast, heavy-particle collisions occur on timescales long compared to the intrinsic electronic timescale ($\sim h/E_{ji}$), leading to adiabatic motion and an exponential suppression of electronic excitation in N–N or N^+–N collisions in the low-velocity limit. Heavy-particle de-excitation, however, is exothermic and can proceed through adiabatic evolution of a transient quasi-molecule. Although such heavy-particle quenching of excited states may reduce the efficiency of atomic line cooling under certain conditions, calculation of the effect is beyond the scope of the present study.

Another density regime is the coronal limit, where collisional excitations are in dynamic balance with spontaneous emission - a simple non-LTE limit. The volumetric cooling rate then becomes independent of A_{ul} in the two-level atom approximation: every electron excited to the upper level spontaneously decays, so that

$$Q_{ul}^{(2)} = n_l C_{lu} E_{ul}, \tag{3.1a}$$

$$C_{lu} = \gamma_{\rm C} n_e \frac{8.629 \times 10^{-6}}{g_l \sqrt{T}} \exp\left(-\frac{E_{lu}}{k_B T}\right), \tag{3.1b}$$

where C_{lu} is collisional excitation coefficient from the lower l to upper level u and $\gamma_{\rm C}$ is the effective collision strength; the formula takes number densities in cm^3 and temperatures in K (Nakayama et al., 2022). An important note is that the two-level coronal cooling scales as the density squared $\propto n_l n_e$. The two-level critical density $n_{cr}^{(2)}$ separating the LTE and coronal regimes is given by

$$n_{cr}^{(2)} = \frac{A_{ul}}{C_{ul}}, \tag{3.2}$$

where the collisional deexcitation coefficient is

$$C_{ul} = \gamma_{\rm C} n_e \frac{8.629 \times 10^{-6}}{g_u \sqrt{T}}, \tag{3.3}$$

and if $n_e \ll n_{cr}^{(2)}$ the plasma will be in the coronal regime.

In this sub-section, we will explore in detail the states of the neutral nitrogen atom (NI) described by three quantum numbers: principal, orbital angular momentum and intrinsic angular momentum. This accounts for interparticle electrostatics through spin-spin and orbit-orbit coupling but neglects spin-orbit coupling and the associated fine structure. The first three levels of NI are displayed in Figure 3.1 adopting term notation, along with those of NII. All data are taken from Nakayama et al. (2022), including those of the oxygen lines in OI and OII, which we will sometimes reference for comparison.

The longest wavelength electric-dipole-allowed transition to ground is a strong line called the resonance line. The NI resonance line is ${}^4P \rightarrow {}^4S$ with $E_{41} = 10.3\,\text{eV}$, $\lambda_\nu^{\circlearrowleft} = 120\,\text{nm}$ and a radiative lifetime of just 3 ns. However, terrestrial upper atmospheres rank, in terms of astrophysical line sources, as warm $\sim 10^4\,\text{K}$ and tenuous $n_e \ll 10^{10}\,\text{cm}^{-3}$, so the resonance line is dramatically underactivated compared to when in hot and dense conditions that make up LTE. Consequently, the low-lying, electric-dipole-forbidden transitions, which are shown in Figure 3.1, dominate. At temperatures up to 20 000 K, a three-level atom is sufficient to model the collisional-radiative non-equilibrium explicitly. The first two excited states have long radiative lifetimes, but in the three-level coronal limit, the cooling contribution is only weakly dependent on the Einstein-A.

We can approximately model [NI] as a three-level atom excited by electron impact, as has been done for fine structure of the NII ground state by Goldsmith et al. (2015). The populations of these three levels depend on the collisional and radiative Einstein coefficients

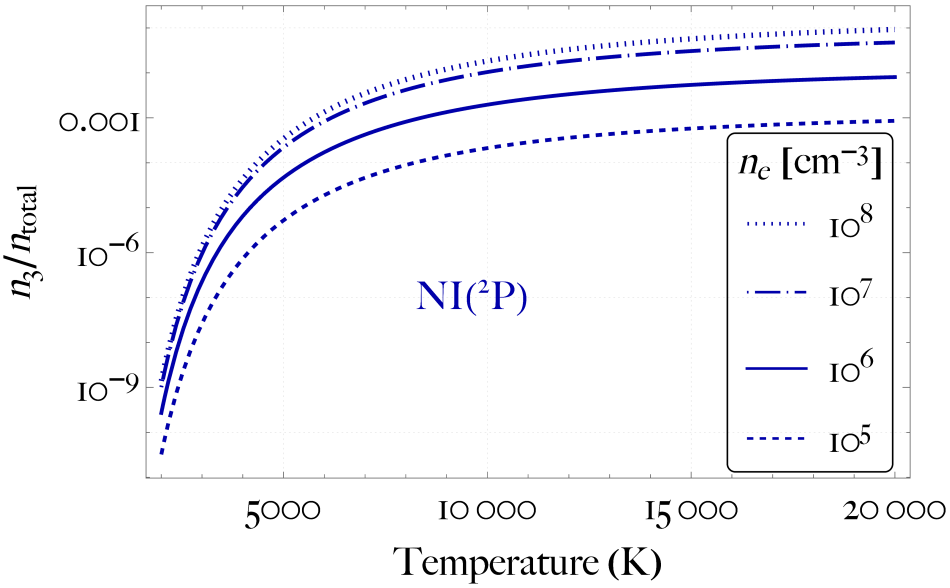

Fig. 3.2 The ratio of nitrogen atoms excited two levels above ground n_3 to the total population n_{total} plotted as a function of temperature and electron density; calculated with a three-level atom approximation (Eqn 3.4). Note that the cooling luminosity in each line is directly proportional to the number of atoms in each excited level.

such that

$$\begin{aligned} -(A_{32}+C_{32}+C_{31})\,n_3 + C_{23}\,n_2 + C_{13}\,n_1 &= 0 \\ (A_{32}+C_{32})\,n_3 - (A_{21}+C_{21}+C_{23})\,n_2 + C_{12}\,n_1 &= 0 \\ C_{31}\,n_3 + (A_{21}+C_{21})\,n_2 - (C_{12}+C_{13})\,n_1 &= 0 \\ n_3 + n_2 + n_1 &= n_{total} \end{aligned} \tag{3.4}$$

Reduction of these equations to the population ratios yields a dependence only on the electron density and temperature as displayed in Figure 3.2. The three-level critical densities differ from the two-level model. The population of the third level only begins to be independent of density around $n_3^{cr} \sim 10^8\,\mathrm{cm}^{-3}$, which is about an order of magnitude greater than that found with the inadequate two-level model. We have neglected photochemical production of excited states which should be reasonable for nitrogen atmospheres but might be major in a carbon dioxide atmosphere.

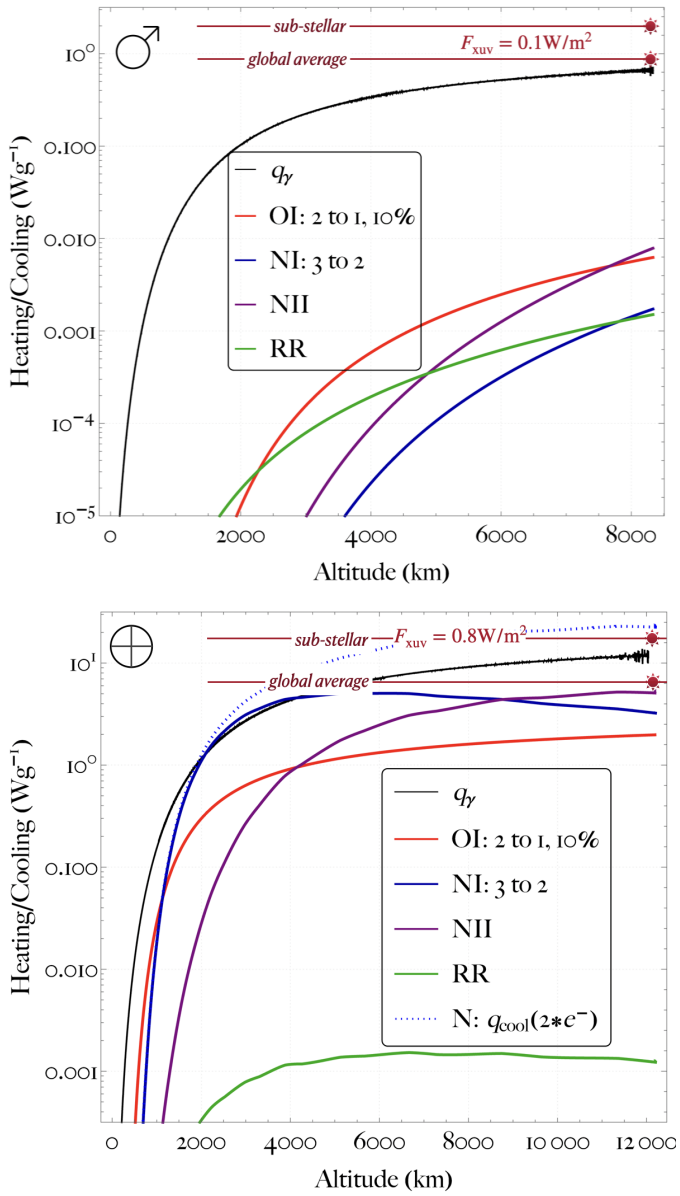

Fig. 3.3 Polytropic heating (q_γ in black; see Eqn 2.4) compared to forbidden line cooling (blue, red and purple; see Eqn 3.4) and recombination cooling (green) per unit mass. Displayed optically thin heating expected from the incoming sub-stellar and globally averaged XUV flux of (see Eqn 2.23). In blue is the cooling from the auroral transition of NI and in red is the cooling effect of mixing in 10% oxygen, which is dominated by the nebular transition. Lastly, in green is the cooling from radiative recombination of N^+. (A) Young Sun Mars $(n_0, \lambda_0, \gamma_{on}) = (10^{14}\,cm^{-3}, 105, 0.826)$. Cooling is calculated by assuming an upper-bound uniform free electron density of $10^6\,cm^{-3}$ and corresponding density of N^+ (NII) by quasineutrality. (B) Cooling for the Young Sun Earth hydrodynamic onset is calculated using electron profile from Johnstone et al. (2019), which peaks at $10^{6.5}$ electrons cm^{-3}. The effect of doubling the estimated electron densities on the total line cooling from nitrogen is shown in dashed-blue ($q_{cool}(2 \times e^-)$).

Exploring [NI] in Figure 3.1, the long radiative lifetime of the first excited level at 2.4 eV above ground (indexed 2) of NI at 21 hours means that the $2(^2D) \rightarrow 1(^4S)$ 'nebular' forbidden transition is a poor cooling mechanism. The second excited level, or third level of the atom, contributes two lines at $E_{31} = 3.6$ eV: the 'transauroral' transition $3(^2P) \rightarrow 1(^4S)$ has transition rate $A_{31} = 5.22 \times 10^{-3}\,\mathrm{s}^{-1}$, which is minor compared to the $3(^2P) \rightarrow 2(^2D)$ 'auroral' transition with $A_{32} = 8.47 \times 10^{-2}\,\mathrm{s}^{-1}$. Thus, the third excited level has a lifetime of 12 s and cooling is dominated from the first three levels by $[\mathrm{NI}]^{3\rightarrow 2}_{1.04\mu\mathrm{m}}$ with $E_{32} = 1.2$ eV.

We use a cool-to-space approximation as the forbidden lines make up a small optical depth due to their small Einstein-A (López-Puertas and Taylor, 2001). We calculate the optical depth assuming Doppler broadening only:

$$\tau_{\nu_{ul}} = \left(\frac{hc_l}{E_{ul}}\right)^3 \frac{\sqrt{\gamma} g_u N}{8\pi^{3/2} g_l} \frac{A_{ul}}{c_\gamma}, \tag{3.5}$$

where N is the total column density above the thermobase, h Planck's constant and c_l the speed of light (Kunc and Soon, 1989). The escape probability formulation used in Nakayama et al. (2022) is not necessary for this regime as line photons propagated below the thermobase are lost as blackbody radiation - still contributing a net cooling to the thermosphere.

3.3 Is Line cooling Minor in the Weakly ionized Onset of Hydrodynamic Escape?

3.3.1 Young Sun Mars

The heating at the sonic point in the polytropic onset model for Young Sun Mars $(10^{14}\,\mathrm{cm}^{-3}, 105, 0.826)$ is consistent to within a factor of two of the optically thin heating expected from the incoming globally averaged XUV flux of $0.1\,\mathrm{W\,m}^{-2}$ (see Eqns 2.24-2.23). Figure 3.3 shows how in an advection-dominated nitrogen flow at these temperatures,

atomic line cooling is not significant compared to the heating required for model Knudsen onset. We assume an upper-bound uniform free electron density of $10^6\,\mathrm{cm}^{-3}$. NI is inefficient at cooling compared to CI and OI at these temperatures. For example, the Einstein coefficient for the $2 \rightarrow 1$ transition is approximately 700× larger for OI than NI, explaining how a 10% mixing ratio of oxygen would dominate the cooling. However, the model heating is more than 10× the OI cooling, so we would still expect consistent onset hydrodynamic escape even for a pure oxygen thermosphere. Radiative recombination (see Section 3.4) contributes the greatets cooling below 2000 km. Mars, with a gravitational binding atmosphere a fifth of Earth's, thus represents well the limit where line cooling is not the controlling factor in the retention of a secondary atmosphere.

3.3.2 Young Sun Earth

The Knudsen-onset from the polytopic model for a nitrogen-dominated atmosphere ($10^{15}\,\mathrm{cm}^{-3}$, 416, 0.77) is again within a factor of two of the optically thin heating expected from the incoming globally averaged XUV flux of $0.8\,\mathrm{W\,m}^{-2}$ found to be required in Section 2.3.3. However, compared to Mars, the hotter aeronomy required to escape Earth's gravitational well results in significant line cooling. The electron density profile used for all the curves is from Johnstone et al. (2019), where we also double the electron density in the profile as a sensitivity test. The profile has a peak electron density of $3 \times 10^6\,\mathrm{cm}^{-3}$, above which the density decreases towards the sonic point and beyond.

The contributions to cooling are as follows. The blue curves in Figure 3.3 show cooling from the auroral transition of neutral nitrogen. In addition, the cooling effect from mixing in 10% atomic oxygen is shown through the dominant nebular transition of OI in red. Figure 3.3 shows how cooling is minor at the sonic point compared to the XUV heating. The auroral cooling of NI at 1040 nm in blue almost matches the implicit heating in the middle atmosphere. The NII cooling assumes nitrogen ion density equal to the electron

density by quasineutrality. Due to shorter radiative lifetimes (see Fig 3.1), the line cooling of NII becomes dominant at the sonic point despite being a minor fraction. The OI nebular line dominates at the bottom of the atmosphere, where temperatures are low. Radiative recombination of atomic ions and electrons is minor in the upper atmosphere.

Though the cooling integrated over the model atmosphere is minor, the comparable heating and cooling in the middle atmosphere leads us to set the efficiency sub-factor from cooling as $\eta_c = 0.5$. So, overall efficiency of the outflow $\eta \approx \eta_\gamma \eta_{\rm pr} \eta_c \approx 0.13$. An XUV flux twice as intense, corresponding to $\sim 400 F_{\rm XUV,\oplus}$, is then enough to account for non-LTE cooling. When the ionization fraction is doubled compared to Johnstone et al. (2019) the total nitrogen cooling dominates over the $\sim 200 F_{\rm XUV,\oplus}$ polytropic heating in the atmosphere above 3000 km (Fig 3.3). To explore these sensitivities, we will next explore the dynamics of hydrodynamic escape and hydrostatic instability with freely varying electron densities in an analytic model of the collisional-radiative thermostat.

3.4 Collisional-radiative Thermostat and Global Ion Outflow

We now focus our attention towards the dynamics of predominantly ionized outflow. We show that the large escape velocity of super-Earths means that an XUV-driven global ion outflow is the only route towards rapid escape of a secondary atmosphere. The formulation of ion-electron effects in the instability of forced hydrostatic atmospheres is also key to understanding the differing conclusion of the present study from that of Nakayama et al. (2022).

3.4.1 Plasma Escape Temperature

Higher ionization fractions lead to greater line cooling, reducing the tendency of an atmosphere to escape. The counter-effect, hitherto unremarked upon in the context of global

loss of secondary atmospheres, is the increase in sound speed in an ionized atmosphere, or equivalently, the reduction in effective mean molecular weight, and thus a reduced escape temperature via $GM\mu/(k_B T_{esc} r) = 2$ (see Eqn 2.13). An ambipolar electrostatic field couples the plasma, reducing escape of electrons and promoting escape of ions (e.g., Bauer and Lammer, 2004; Koskinen et al., 2013).

The ion-acoustic speed of sound for a quasineutral mixture without secondary ionization is

$$c_{i-a}^2 = \frac{\gamma_e f_+ k_B T_e + \gamma_i f_+ k_B T_i + (1-f_+)\gamma_n k_B T_n}{f_+ m_e + f_+ m_i + (1-f_+) m_n}, \tag{3.6}$$

where f_+ is the ionization fraction, and m_e, m_i and m_n refer to the electron, ion and neutral atom masses respectively (e.g., Chen, 2016). We can assume ion-electron thermalization and approximately isothermal outflow in these high XUV flux conditions, such that neutral, ion and electron temperatures and ratios of specific heat are equal $T_i \approx T_e, \gamma_i = \gamma_e = 1$. The ion-acoustic sound speed can then be simplified to

$$c_{i-a}^2 \approx \frac{(1+f_+) k_B T_i}{m_i}. \tag{3.7}$$

Thus, the mean molecular weight will be given by

$$\mu(f_+) \approx \frac{m_i}{1+f_+}, \tag{3.8}$$

so for $f_+ = 0.5$ or 1, the mean molecular weight is 2/3 or 1/2 the neutral equivalent. We define the local *plasma* escape temperature as the escape temperature when the local ionization fraction is roughly unity:

$$T_{\rm esc}(f_+ = 1) = \frac{m_i}{2} \frac{v_{\rm esc}(r)^2}{4 k_B} = \frac{T_{\rm esc}(f_+ = 0)}{2}. \tag{3.9}$$

As displayed in Figure 3.5, the escape temperature for neutral outflow from Earth is approximately 18 000 K but for a fully ionized atmosphere only 9000 K. This simple derivation captures the principal physics, but ionospheric processes are highly non-linear and this effect could also be enhanced (Collinson et al., 2024). Rocky exoplanet ionospheres are ripe for research.

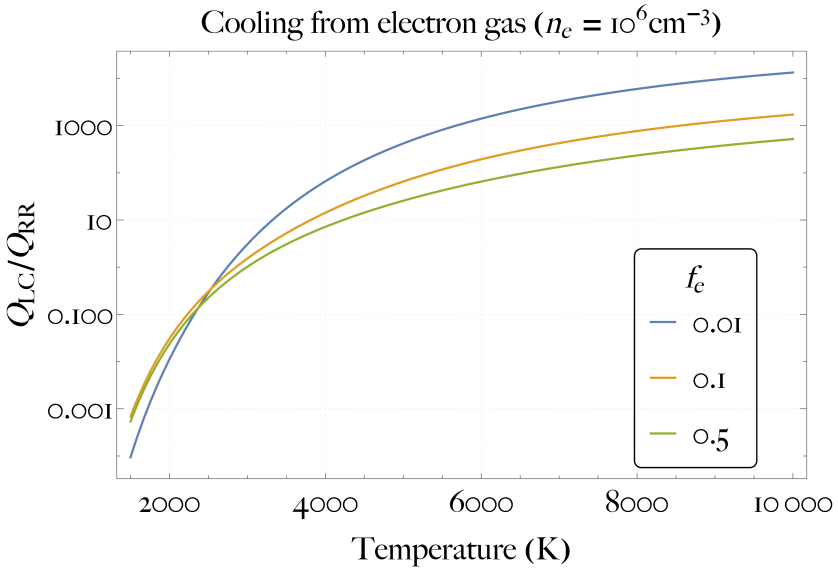

Fig. 3.4 Ratio of local cooling luminosities from excitation of atomic lines Q_{LC} and ion-electron radiative recombination Q_{RR}. The electron density is 10^6 cm^{-3}. The density of neutral nitrogen atoms is varied from 10^8 cm^{-3} (blue) and 10^7 cm^{-3} (orange) and 10^6 cm^{-3} (green) at temperatures from 1500 K to 10 000 K. This is roughly equivalent to ionisation fractions of $f_+ = 0.01, 0.1, 0.5$.

3.4.2 Ion-Electron Recombination

In the lower and upper layers of Earth's ionosphere, the primary sinks of photoelectrons are dissociative recombination of molecular ions and ambipolar diffusion, respectively (Bauer and Lammer, 2004). These mechanisms require a background of molecular and neutral species, which close the chemical network via charge transfer. The radiative recombination of ions and electrons, though significant in the F2 layer, remains minor throughout the atmosphere (Solomon, 2010). However, under the raised XUV fluxes that yield extended

ionospheres and greater total electron content, radiative recombination can become the primary sink for photoelectrons (e.g., Nakayama et al., 2022).

To introduce the role of recombination, we first compare the dynamics of radiative-recombination cooling with atomic line cooling. The rate of dielectronic recombination, which proceeds via a metastable intermediate, was calculated with a fit from Zatsarinny et al. (2004, 2005) and found to be minor for 200 K $< T <$ 20 000 K, only matching the radiative recombination rate at ≈ 27 000 K. Hence, dielectronic recombination is negligible for the conditions considered in this study. The derivation of radiative recombination (RR) rates takes advantage of photoionization cross-section data, being the time-reversed process, and is fit with the following formula from Badnell (2006):

$$\alpha_{\mathrm{RR}}(T) = A\left[\sqrt{T/T_0}\left(1+\sqrt{T/T_0}\right)^{1-B-C\exp(-T/T_2)} + \left(1+\sqrt{T/T_1}\right)^{1-B-C\exp(-T/T_2)}\right]^{-1}, \quad (3.10)$$

where $(T_0, T_1, T_2, A, B, C) = (9.467\times10^{-2}\,\mathrm{K}, 2.954\times10^{6}\,\mathrm{K}, 6.379\times10^{4}\,\mathrm{K}, 6.387\times10^{-10}\,\mathrm{cm^3\,s^{-1}}$, 0.7308, 0.2440). The timescale of thermalization via collisions t_{th} remains shorter than the recombination timescale t_{RR} even when the photoionization rate $1/t_{pi}$ is fast, $t_{th} \ll t_{RR} \sim t_{pi}$, meaning that for each creation of a photoelectron, a *thermal* electron and an ion recombine. The average photon energy from recombination to N is $\sim h\nu_{\mathrm{I}} + 3k_B T_e/2$, but the thermal loss from the electron gas is only the continuum part $Q_{RR} \propto 3k_B T_e/2$. In radiative recombination, cooling is less than total emission because the potential energy an atom gains during ionization is retained, rather than being transferred to the electron gas. Accordingly, the ionization potential is considered as an inefficiency of photoionization heating $\eta_{pi} \approx 1 - \nu_{\mathrm{I}}/\overline{\nu}$ throughout our calculations. An exact formula for recombination cooling can be found in Tucker and Gould (1966).

We compare the ratio of the volumetric line cooling to RR cooling in Figure 3.4 for varying ionization fractions f_+. Recombination is dominant by several orders of magnitude at ~10^3 K, with excitation of atomic lines increasing steeply with temperature until matching

recombination at ~3000 K and going on to dominate by up to several orders of magnitude at 10^4 K. Nakayama et al. (2022) calculate radiative recombination via an unspecified prescription and do not discuss its dynamics in detail, so direct comparison is unavailable. However, their conclusion that the key role of forbidden-line cooling in escape is not superseded by recombination cooling agrees with the work reported here.

3.4.3 The Thermostat of Photoionization versus Line Cooling

In this sub-section, we explore how photoionization both heats the atmosphere but also generates free electrons that excite greater line cooling. We consider quasineutral nitrogen layers in the upper atmosphere that are optically thin to incoming XUV photons. The rate ions are advected away, through either acceleration in bulk outflow or molecular diffusion, can be included such that the transport equation for N becomes

$$\frac{F_{\rm XUV}\overline{\sigma_{\nu_{\rm I}}}}{h\overline{\nu_{\rm I}}} n_{\rm N} \approx n_e \alpha_{\rm RR} n_{\rm N^+} + nu\frac{{\rm d}f_+}{{\rm d}r}, \tag{3.11}$$

where $f_+ = \frac{n_{\rm N^+}}{n}$ and we have implemented a monochromatic approximation at the front (e.g., **?**). The mean of energy of photons producing singly and doubly ionized nitrogen is $h\overline{\nu_{\rm I}} \approx 33.6$ eV and $h\overline{\nu_{\rm II}} \approx 56.5$ eV, and the mean absorption cross section are similar: $\overline{\sigma_{\nu_{\rm I}}} \approx \overline{\sigma_{\nu_{\rm II}}} \approx 10^{-17}$ cm^2 evaluated for a Modern Active Sun Spectrum (Huebner and Mukherjee, 2015).

The cooling from the forbidden line cooling of NI and NII must balance the net heating from photoionization:

$$n\epsilon F^{\theta}_{\rm XUV}\left(f_+\frac{\Delta\nu_{\rm II}}{\overline{\nu_{\rm II}}}\overline{\sigma_{\nu_{\rm II}}} + (1-f_+)\frac{\Delta\nu_{\rm I}}{\overline{\nu_{\rm I}}}\overline{\sigma_{\nu_{\rm I}}}\right) \approx \sum_{\rm NI}^{\rm NII}\sum_{j,i>j}^{1\to3} n_i(T,n_e)A_{ij}E_{ij}\,, \tag{3.12}$$

where the average excess energies $\Delta\nu_{\rm I,II} = \overline{\nu_{\rm I,II}} - 3k_BT_e/2 - h\nu_{\rm I,II}$ and the number densities $n_i(T,n_e)$ are solutions from the three-level model (Eqn 3.4). The efficiency prefactor ϵ is the

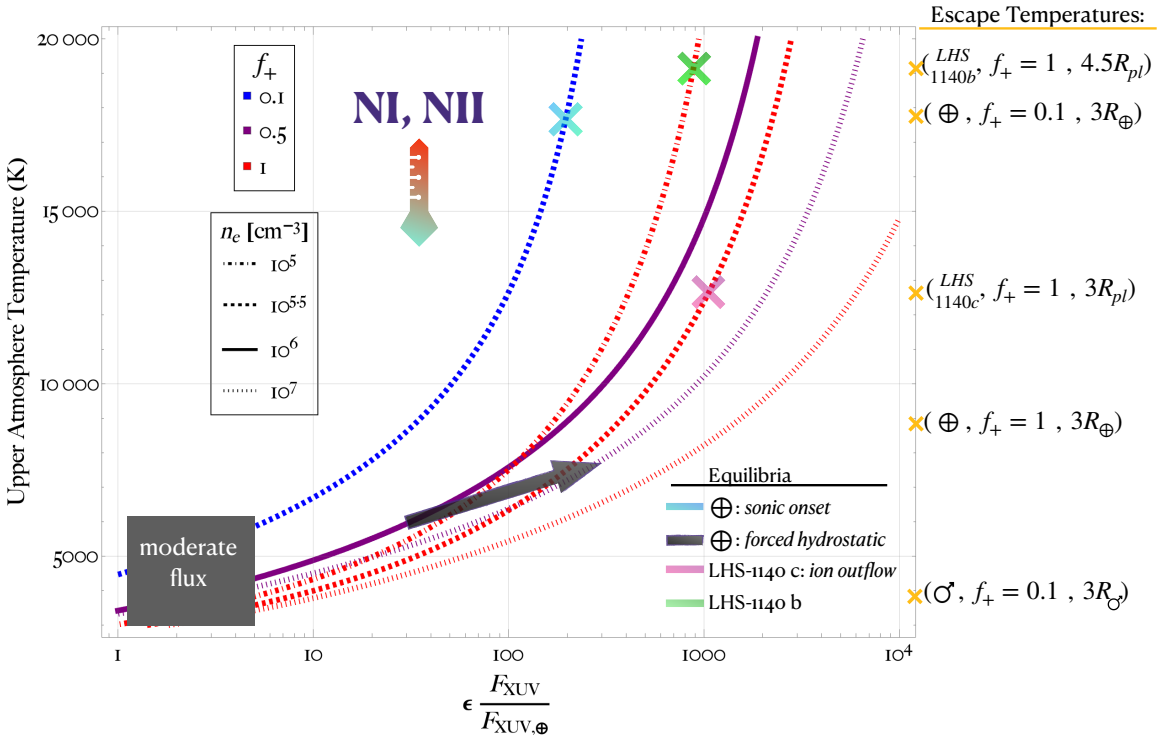

Fig. 3.5 The upper atmosphere temperatures determined locally by the collisional-radiative thermostat as a function of XUV flux relative to Modern Solar conditions and electron densities. The escape temperatures are shown for each planet with a range of ionization fractions f_+ (Eqns 2.13 & 3.8). *Note for interpretation that a hydrostatic exobase at greater than half the escape temperature is unstable and the sonic point of a hydrodynamic outflow will approximately reach the escape temperature.* A range of ionization fractions $0.1 - 1$ and local electron densities $10^5 - 10^7$ cm^{-3} are identified by legends on the lefthand side. Advection reduces the energy available from XUV heating, along with thermal conduction and the assumed minor optical attenuation; expressed in the prefactor ϵ. The blue cross highlights a local equilibrium at the sonic point roughly consistent with the Young Sun Earth polytropic onset at $\approx 400 F_{XUV,\oplus}$ (see Section 2.3.3). The black arrow illustrates a feedback between photoionization and line cooling on temperature relevant to Nakayama et al. (2022). However, if the hydrostatic Earth-like atmosphere reaches high ionization fractions in the black-arrow evolution it becomes unstable to escape. The pink and green crosses roughly indicate the XUV fluxes required to drive global ion outflow from LHS 1140 c and LHS 1140 b based on their plasma escape temperatures. Exoplanet data are taken from Cadieux et al. (2024). Transonic mass loss rates are proportional to sonic-point densities (Eqn 3.13).

fraction of local heating sunk into line cooling, as opposed to advection $Q_{\rm adv}$ and conduction $Q_{\rm cond}$. Minor optical attenuation is also represented in $\epsilon \approx e^{-\tau}(1-(Q_{\rm cond}+Q_{\rm adv})/Q_{\rm XUV})$, where $\tau \lesssim 1$. Even if advection is major for the transport of ions, it may have a minor contribution to the energy balance. Thermal conduction down the thermospheric inversion can contribute significant cooling locally, but the front may also be found where the temperature profile has flattened. Thus, ϵ takes values $\sim 0.1-1$.

The collisional-radiative thermostat effect of Equation (3.12) is illustrated in Figure 3.5. For fixed electron density, order of magnitude changes in the XUV flux cause order unity changes in the temperature generated. However, higher XUV flux results in a greater electron density in the front, which increases line cooling and feedbacks on the temperature; see forced-hydrostatic evolution (black arrow, Fig 3.5). Optically thin absorption is proportional to the electron density (via the total density), while the line cooling dependence has a proportionality closer to the square of the electron density, which is exact in the two-level coronal model (Eqn 3.1b). Increasing electron density has a more marginal effect when approaching the critical density for LTE (see Sec 3.3), which is sometimes referred to as quenching (Bauer and Lammer, 2004). For the transonic outflow equilibria, the mass loss rate can be interpolated from Figure 3.5 using

$$\Phi_{hyd} \simeq 4\pi r_{sc}^2 (m_i n_e / f_+)\sqrt{k_B T_{sc}/\mu}\,. \tag{3.13}$$

3.4.4 Comparison to Nakayama et al. (2022)

The collisional-radiative thermostat (Eqn 3.12) offers a broad physical explanation of the surprisingly uniform temperature dynamics of the exobase at high XUV fluxes in Nakayama et al. (2022): a feedback between forbidden line cooling and photoionization heating mediated by electron density. Nakayama et al. (2022) calculate that for $500F_{\rm XUV,\oplus}$ the ionization front $f_+ = 0.5$ occurs at an altitude of ~ 3000 km, reaching a peak temperature of

5500 K. The ionization front temperatures for $50 \rightarrow 1000 F_{\mathrm{XUV},\oplus}$ are within a 500 K temperature interval, indicating a thermostatic effect must be present. In Figure 3.5, we explore a reduced model of the ionization with the forced hydrostatic arrow taking the range $(\epsilon F_{\mathrm{XUV}},\ n,\ f_e) : (30,\ 10^6\ \mathrm{cm}^{-3},\ 0.5) \rightarrow (300,\ 10^7\ \mathrm{cm}^{-3},\ 0.5)$. Equation 3.12 yields $T_{stat} : 6000 \rightarrow 8000$ K and above the front ionization fractions reach unity. Compared to Nakayama et al. (2022), the excess temperature can be partially explained through oxygen line cooling, which is neglected in our model.

However, the present study does not concur with Nakayama et al. (2022) that the thermostat allows survival of an Earth-like atmosphere up to $1000 F_{\mathrm{XUV},\oplus}$. Though the forced-hydrostatic Earth-like equilibrium in Figure 3.5 remains at less than half of the fixed-neutral escape temperature, it is the plasma escape temperature that should be considered for ionization fractions close to unity (Eqn 3.9). The forced-hydrostatic evolution in Figure 3.5 exceeds half the plasma escape temperature, almost reaching it, and would outflow. In general, the intermediate free evolution from hydrostatic instability to hydrodynamic escape could occur through the Coulomb-collisional expansion of ions and electrons aloft of a neutral N-exobase, which drags the atmosphere through the exobase in a drifting Maxwellian (Volkov et al., 2011).

We also highlight the apparent lack of sensitivity of the height of the model exobase to increasing XUV flux in Nakayama et al. (2022). On the flux increasing by a factor of ten from $50 \rightarrow 500 F_{\mathrm{XUV},\oplus}$, the apparent height increases only by 20%, or roughly a single local scale height. We expect that the increase of peak electron density with XUV flux should push the exobase significantly further out because (1) the scale height increases with the reduction of mean molecular weight from ambipolar diffusion and (2) the more frequent electron-neutral and ion-neutral collisions allow the neutral-N exobase to form at orders of magnitude lower densities. Moreover, at $500 F_{\mathrm{XUV},\oplus}$ Nakayama et al. (2022) find the ionization fraction at the top of the atmosphere to be unity, so that before the mean free path of nitrogen atoms grows

large enough for ballistic escape, the atmosphere is ionized enough that formation of a neutral exobase is precluded.

The polytropic model and the transonic onset equilibrium for Young-Sun Earth in Figure 3.5 roughly agree that $400F_{\mathrm{XUV},\oplus}$ provides enough heating to drive escape at the neutral onset as a conservative estimate. So, together with the instability of the forced hydrostatic equilibrium (Fig 3.5) relative to the plasma escape temperature, our idealized modeling offers a consistent picture.

Table 3.1 Equilibria and Escape Rates of Photoevaporating Nitrogen Atmospheres

Transonic:	$\times F_{\mathrm{XUV},\oplus}$	Vertical eqm	Primary balance	f_+	Consistent	Comment	Φ_{hyd} (bar/Myr)
YS Mars	50	hydrodynamic	ionization-advection	$\lesssim 0.1$	✓	$q_\gamma \gg q_c$, EL	2
YS Earth	400	hydrostatic	ionization-recombination	$\lesssim 1$	×	→ ion outflow	6
		hydrodynamic	ionization-advection	~ 0.1	✓*	$q_\gamma \gtrsim q_c$	
LHS-1140 c	1000	hydrodynamic	ioniz.-adv.-recom.	~ 1	✓ (?)	$1.9 \times M_\oplus$	~ 1.2
LHS-1140 b	2000	hydrodynamic	ioniz.-adv.-recom.	~ 1	✓ (?)	$5.6 \times M_\oplus$	~ 0.9

Note: YS stands for the Young Sun scenarios modelled. q_γ and q_c refer to local XUV-heating and atomic line cooling. EL means the simple energy-limit applies. The "→ ion outflow" line marks the transient switch from an unstable hydrostatic state. "Ioniz.-adv.-recom." denotes ionization balanced by advection + recombination (steady global ion outflow). Numbers are analytic best guesses; see PHIDRATES database Huebner and Mukherjee (2015) and text for details.

3.4.5 TRAPPIST 1-b: Airless

TRAPPIST-1 b has radius $1.16 R_\oplus$ and mass $1.37 M_\oplus$ (Agol et al., 2021). Its escape velocity is then $12.2\,\mathrm{km\,s^{-1}}$, less than 10 % different from Earth, so we expect a similar escape regime for similar XUV fluxes. We do not plot TRAPPIST-1 b's escape temperatures in Figure 3.5 because they are similar to Earth's.

At significantly higher XUV fluxes than Young Sun Earth, the dominant balance of photoionization is expected to be from radiative recombination as opposed to advection; this has been considered in the photoevaporation of hydrogen envelopes (e.g., **?**Owen and Jackson, 2012). Furthermore, the transonic mass loss rate is not expected to rise in proportion to XUV flux indefinitely due to the limited penetration of XUV heating and the increasing severity of temperature inversion required against the effects of conduction and line cooling. To calculate the XUV flux for which mass loss rates plateau would require a hydrocode with the correct photochemistry and electrodynamics, so is beyond the scope of this work. However, a hypothetical atmosphere of nitrogen could outflow from TRAPPIST-1 b at $(\epsilon F_{\mathrm{XUV}},\ n,\ f_+) : (10^{3.5},\ 10^7\,\mathrm{cm^{-3}},\ 1)$ (Fig 3.5) with a close-in sonic point, possibly a detached D-type shock (Spitzer, 1978).

Thus, unless TRAPPIST-1 b formed extremely volatile rich, it is unlikely that any atmosphere would remain today. Indeed, Van Looveren et al. (2024) calculate that even the present-day fluxes of ionizing radiation in the TRAPPIST-1 planetary system are intense enough to preclude the retention of any Earth-like or Venus-like atmosphere. However, we note that they use a forced-hydrostatic Jeans prescription of escape that does not include the key electric-dipole-forbidden lines.

3.4.6 LHS 1140 b and c: Airy?

The escape temperature for a predominantly neutral flow from LHS 1140 c ($1.9M_\oplus$, $1.27R_\oplus$, 0.027 AU) would be $\gtrsim$ 22 000 K due to the 1.5× tighter gravitational binding that of Earth. However, temperatures would be kept lower by the collisional-radiative thermostat under rising XUV fluxes even for greater than $1000F_{\mathrm{XUV},\oplus}$, so transonic escape with a significant neutral fraction is prevented. The ion-acoustic speed in an ion outflow allows the plasma escape temperature to be half as large as the neutral. The pink cross in Figure 3.5 explores a hypothetical sonic point with an electron density of $10^{5.5}$ cm^{-3} requiring an XUV flux of $10^3 F_{\mathrm{XUV},\oplus}$ to drive escape of one bar every million years. We estimate $\epsilon \sim 1$, assuming that advection is only a minor sink at this flux and the terminal profile to be relatively isothermal. Thus, escape would not be driven for LHS 1140 c with its contemporary instellation of $10^2 F_{\mathrm{XUV},\oplus}$ (Spinelli et al., 2023), but a secondary atmosphere formed in the early pre-main-sequence with $\gtrsim 10^3 \times F_{\mathrm{XUV},\oplus}$ could well have been lost.

The companion planet LHS 1140 b ($5.6M_\oplus$, $1.7R_\oplus$, 0.09 AU) has a 3× deeper gravitational well than Earth, so the neutral escape temperature would be in the ballpark of $\gtrsim$50 000 K. As a result, only an ion outflow is feasible for the hydrodynamic escape of a secondary atmosphere from a 'radius valley' planet. Inspecting the green cross in Figure 3.5, even if the sonic point could form as far out as $4.5R_{pl}$, then assuming $\epsilon \sim 0.5$ and an electron density 10^5 cm^{-3} an XUV flux of $2000F_{\mathrm{XUV},\oplus}$ would be required. Since temperature must rise steeply to reach $\sim 2\times10^4$ K, thermal conduction is expected to be significant and we estimate $\epsilon \sim 0.5$. If escape at lower densities is possible, the required flux would be reduced but so would the escape rate (Eqn 3.13). In the LHS 1140 system, planet b only receives one twelth of the instellation of c. So, a thick secondary atmosphere is unlikely to be photoevaporated even accounting for early pre-main-sequence fluxes.

Whether LHS 1140 c would retain a thick secondary atmosphere is sensitive to its initial conditions, but LHS 1140 b should have retained its atmosphere, consistent with observa-

tions from Cadieux et al. (2024). For cool rocky planets orbiting low-mass stars, the higher escape temperatures of super-Earths compared to sub-Earths is crucial to prospects for the retention of secondary atmospheres.

3.5 Discussion

The rapid escape of heavier species is usually only considered in drag-off by hydrogen, so the direct hydrodynamic escape of a nitrogen or carbon dioxide atmosphere is often left out of atmospheric evolution studies of rocky planets (e.g., Teixeira et al., 2023). In fact, for a planet with a thick secondary atmosphere, such as Venus, other erosion mechanisms are generally too slow or variable, leaving direct hydrodynamic escape as the main route to airlessness (e.g., Gronoff et al., 2020b). Early *JWST* observations are revealing a pattern of cool rocky worlds that are airless or thinly blanketed. Thus, observations and theory suggest that atmospheric retention could be a major bottleneck in the occurrence of observable Earth-like habitats $\eta_\oplus$ (e.g., Scherf et al., 2022).

3.5.1 Landscape of High Molecular Weight Escape

The polytropic framework allows a comparative planetology perspective, with the resulting insight resolvable into the simplified representation of the range of governing physics. Figure 3.6 has λ_0 on the horizontal axis: the ratio of gravitational binding to the thermal reservoir at the mesopause. On the vertical axis is γ describing the steepness of the temperature inversion, which is implicitly determined by XUV instellation (Eqn 2.21). Ratios of base to sonic densities, temperatures, and radii can be read from Figure 3.6. The diagram can be used as a visual aid to see for which star-planet conditions hydrodynamic escape will be possible.

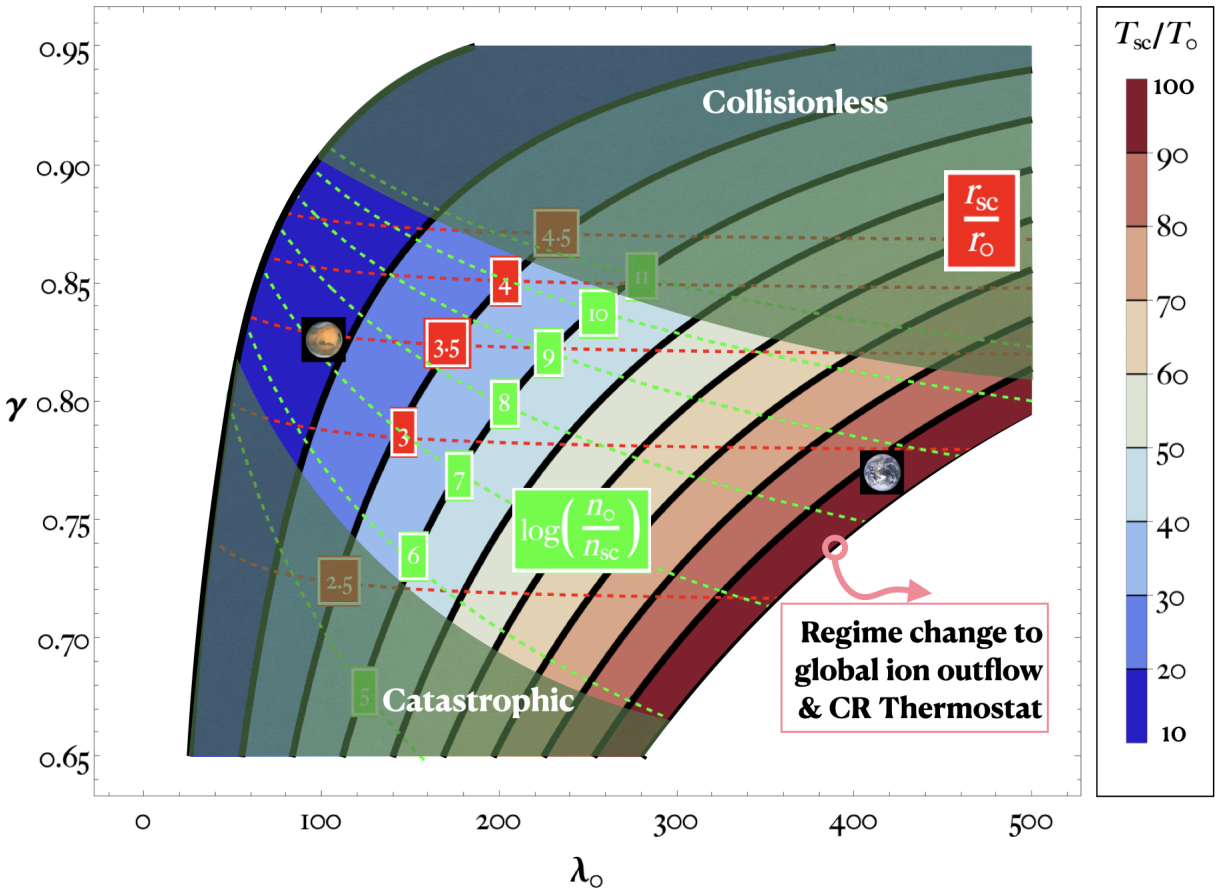

Fig. 3.6 Regime diagram for high molecular weight escape in terms of the polytropic index $0.65 \leq \gamma \leq 0.95$ and the hydrodynamic escape parameter $20 \leq \lambda_0 \leq 500$. The heat map indicates the ratio of sonic to base temperatures $10 - 100$. Contours of uniform ratio of sonic to base radius (red-dashed) and uniform sonic to base density in log units (green dashed). The Young Sun Earth (c.f. Figures 2.3 & 3.3) and Young Sun Mars (see Figures 2.4 & **??**) calculations are represented by images of each planet. This figure can be compared to the solution space of polytropic solutions (Fig 2.2). For large enough λ_0, the polytropic model of steep XUV inversions breaks down because line cooling will begin to dominate over advection. The overlaying pink patch is to illustrate that the shift is broad and dependent on boundary conditions and dimensional parameters. Rightward of the transition, the collisional radiative thermostat will control the resulting global ion outflow (see Section 3.4).

The pairwise base-to-sonic ratios in log units map to the proportionally varying Knudsen number at the sonic point if holding base density constant. The right-hand edge where collisional onset may be possible is roughly marked as where the sonic density is ten orders of magnitude smaller than at the base. On the $\log[n_0/n_{sc}] = 10$ contour itself, extremely deep penetration of XUV would be required for the flow to launch the outflow from that dense portion of the atmosphere. The left-hand edge is given by the $\log[n_0/n_{sc}] = 6$ contour, where the sonic Knudsen number would likely be more than an order of magnitude smaller than at onset. In this high XUV-flux limit, the assumption of predominantly neutral outflow is likely to break down. Furthermore, the mass loss will be catastrophically fast.

In the region marked out between $6 < \log[n_0/n_{sc}] < 10$, the sonic radii vary between two and four times the planetary radius. The base to sonic temperature ratio is given by $T_{sc} = \frac{\lambda_0 r_0 T_0}{2\gamma r_{sc}}$, and is a proxy for when line cooling will become significant in the atmospheres of temperate rocky planets. Accordingly, the consistency of transonic hydrodynamic escape is clear-cut for XUV-evaporation of a thick nitrogen atmosphere on a Mars-like planet due to the lower gravitational binding of the atmosphere. Transonic hydrodynamic escape of the nitrogen atmosphere can be driven with upper atmosphere temperatures staying below 4000K, low enough for negligible line cooling. The threshold XUV flux for collisional onset for Mars is calculated as 100× Modern Day Mars XUV, which we highlight as overly conservative compared to previous studies (e.g., Tian et al., 2009), and would entail a rapid loss rate of 20 bars per million years. For much lower XUV fluxes, the threshold for instability of a hydrostatic nitrogen atmosphere at ~ 2000 K would be exceeded.

For the gravitational binding of the Earth's atmosphere and a cool mesopause, the temperatures monotonically increased to roughly 23 000 K at the sonic point at Knudsen neutral onset. Auroral line cooling from $[\mathrm{NI}]^{3\rightarrow2}_{1.04\mu\mathrm{m}}$ and $[\mathrm{NII}]^{3\rightarrow2}_{611\mathrm{nm}}$ almost matches the polytropic heating regionally. Accounting for line cooling through $\eta_c = 0.5$ in the energy limit (Eqns 2.6 and 2.7b), we find the hydrodynamic loss of six bars of nitrogen per million years for 400×

Modern Day Solar XUV irradiation. To build confidence in this result, we checked agreement from opposite perspective of the line cooling balancing XUV heating with advection being an efficiency factor. We also reanalyzed the hydrostatic thermosphere profiles of Nakayama et al. (2022), finding instability at $500F_{\mathrm{XUV},\oplus}$, possibly lower, while accounting for the effect of ion-electron interactions on the mean molecular weight as captured by the plasma escape temperature (Section 3.4.1). Earth can be viewed as occupying yet another sweet spot where the energy limit starts to break down, and the collisional-radiative thermostat takes over for the loss of secondary atmospheres.

The upper-atmosphere temperatures required to rapidly escape planetary atmospheres with gravitational binding greater than Earth's are prohibitive for the case of predominantly neutral outflow. We hypothesize that even higher XUV fluxes can instead lead to global ion outflow, with atomic line cooling controlling the rate of escape and the collisional regime extending to greater altitudes. Accordingly, a steep polytropic inversion from the thermobase is a poor model. This is highlighted with the righthand regime change in Figure 3.6.

An onset of rapid escape can be found by matching the collisional-radiative thermostated sonic point with the plasma escape temperature, which is more easily achieved due to the twice-as-fast ion-acoustic sound speed (Eqn 3.6). The plasma escape temperature of the super-Earth LHS 1140 c ($1.9M_{\oplus}$) at three planetary radii is roughly 13 000 K. Sonic point analysis suggests an uncertain mass loss rate of a bar of nitrogen every million years on exposure to $\sim 10^3 F_{\mathrm{XUV},\oplus}$ (Figure 3.5). However, more detailed modeling is required to characterize the super-Earth regime beyond the result that escape is appreciably more difficult than from Earth and should take the form of an ion outflow.

Overall, within model uncertainty, Modern Earth's atmosphere might well survive in the XUV-irradiation environment of the Young Sun, depending on its initial rotation rate. However, if placed in the habitable zone of an active M-dwarf, our analysis suggests that the protective effect of the line cooling is overwhelmed, and a thick secondary atmosphere

would likely be lost. Thus, from the perspective of escape, no substantial atmospheres are expected on the TRAPPIST-1 planets unless they formed extremely volatile rich. More advanced modeling and further observations will constrain the reality. For super-Earths orbiting M-dwarfs, the zone of atmospheric retention is larger, making them the most promising observational targets for detecting features of an Earth-like habitat.

3.6 Summary

The emerging dynamics of the work reported here suggests a non-uniform trend for separating airless and airy planets in the space of XUV flux/fluence against a power law in escape velocity. At this stage, we venture to make some broad predictions for the cosmic shoreline in contrast with Zahnle and Catling (2017), which are further considered in Chapter 5. The nonlinear onset and rapid rates of transonic outflow suggest that the key parameter governing the escape of secondary atmospheres is the peak XUV flux experienced at different ages [1], rather than the lifetime fluence:

1. The activity of a star enhances its X-ray luminosity $\sim 3\times$ above the long-term average at each evolutionary stage for $\sim 10\%$ of the time (Johnstone et al., 2021). So, if the *average* main-sequence XUV flux is greater than one third of the threshold for transonic escape, a secondary atmosphere is unlikely to survive or be revived.

2. Otherwise, if main sequence XUV fluxes are low enough that a secondary atmosphere would remain hydrostatic throughout, then its survival will depend on an interplay between stellar wind erosion, volcanic activity and impacts (Kite and Barnett, 2020).

3. Accretion of an envelop of nebular hydrogen, by weathering some or all of the saturated phase of coronal activity on the pre-main-sequence, enhances prospects for retention

[1] This statement, as originally formulated, was envisaged for atmospheres in the range of bars to a hundred bars. For extremely thick envelopes, however, the decisive quantity is instead the integrated lifetime fluence above the threshold for rapid escape, as discussed in Chapter 5

of Earth-like or Venus-like atmosphere. However, where significant metals are lost in hydrogen escape, or the saturated phase last long enough to escape hydrogen and residual secondary components, then the mantle could be catastrophically depleted in volatiles, precluding later revival.

4. We expect the sub-Earth and super-Earth regimes to present as a two-part cosmic shoreline. For rocky planets with escape velocities larger than Earth's, the escape rate and threshold XUV flux are governed by the collisional-radiative thermostat, whereas for smaller escape velocities, the rates are energy-limited with a Knudsen onset.

Model mass losses for a range of planets spanning the cosmic shoreline are summarised in Table 3.1. The large XUV flux requirements for transonic escape could be relaxed in the case of significant Joule heating (Cohen et al., 2024). Overall, the work reported in Chapters 2 & 3 marks the first 1D analytic modelling of the XUV-driven transonic escape of secondary atmospheres from rocky exoplanets. Our inclusion of both ion-electron effects and forbidden-line cooling sets a precedent for modelling global loss of secondary atmospheres. Future studies involving state-of-the-art photochemistry, self-consistent hydrodynamics and molecular-kinetics simulations will be crucial in theoretically constraining Eta-Earth and the Cosmic Shoreline.

4

Predicting the Fate of Rocky Exoplanet Atmospheres

This chapter presents adaptations of evolutionary calculations of atmospheric escape that I contributed to a series of papers: Section 4.2 (Taylor et al., 2025), Section 4.3 (Nicholls et al., 2025a), Section 4.4 (Ji et al., 2025).

4.1 Introduction

The previous chapters presented predictions of the XUV flux thresholds for transonic hydrodynamic escape across the size range of rocky exoplanets. The ensuing escape rates of order a bar every million years would deplete terrestrial atmospheres similar to those on Earth, Mars and Venus, on geological timescales. However, this does not account for the possibility of much greater volatile endowments, such as is consistent with the evo-

lution of sub-Neptunes to super-Earths across the radius valley. Furthermore, meeting the conditions for rapid escape may change over time, such that an atmosphere could be volcanically revived under a matured and less active star. Finally, we present the results that may be of broadest interest to the exoplanet community — a new cosmic shoreline based on adaptations of escape rates from the previous chapters.

4.2 GJ 357 b: JWST Transmission and Potential for an atmosphere

Efforts to detect rocky exoplanet atmospheres with the James Webb Space Telescope are hindered by several factors, including the intense irradiation environments of M-dwarf host stars, which can remove the atmospheres of highly volatile-rich planets (Ji et al., 2025), degeneracies inherent in secondary eclipse observations (Hammond et al., 2024), and stellar contamination in transmission spectra (Radica et al., 2025). This section discusses why, despite the non-detection of an atmosphere in the observations of GJ 357 b (Taylor et al., 2025), its highly inactive M-dwarf host star makes it a relatively strong candidate for follow-up observations aimed at detecting a retained high-MMW atmosphere.

The flat transmission spectrum reported in Taylor et al. (2025) is consistent with the theoretical expectation of escape of a primordial hydrogen atmosphere from GJ 357 b. Atmospheric retrievals reject atmospheres with metallicities $\lesssim$100× solar (~4 g/mol) with 3-σ confidence. The low mass of the host star (0.34 $M_{\odot}$) means GJ 357 b sees a long and intense saturated phase of ionising radiation, contributing to a large enough lifetime XUV fluence to, in principle, remove a volatile inventory greater than the present-day mass of the planet (e.g. Watson et al., 1981; Modirrousta-Galian et al., 2020). As such, GJ 357 b is placed on the airless side of the (XUV) cosmic shoreline (Zahnle and Catling, 2017). However, a high-molecular-weight atmosphere is more resilient to photoevaporation and could be outgassed later in

the star's evolution— its presence would also be consistent with the featureless spectrum from Taylor et al. (2025).

4.2.1 Evolution of Ionising Luminosity

To estimate the evolution of the photoevaporation regime of GJ 357 b we use MORS (Johnstone et al., 2021), a physical rotational evolution model of the high energy emission of stars that is constrained by observed rotational and X-ray distributions in stellar clusters. Direct measurements of the X-ray luminosity are also available with *XMM-Newton* from Modirrousta-Galian et al. (2020), which found $\log L_{\rm x}\left[\mathrm{ergs}^{-1}\right] = 25.73 \pm 0.23$ (grey diamond, Fig 4.1). At such a relatively small X-ray surface flux, the EUV emission is relatively enhanced: we calculate with scaling relations from Johnstone et al. (2021) that the corresponding total XUV luminosity is an order of magnitude higher (black diamond, Fig 4.1). Figure 4.1 shows that the measured X-ray luminosity is more than an order of magnitude below the main-sequence cycle-average for a star of mass $0.34 M_{\odot}$ following the lowest activity track available from MORS (blue, Fig 4.1; Johnstone et al., 2021). The purple track on Figure 4.1 shows the estimated intrinsic variability: the X-ray luminosity will exceed the long-term average by a factor of three roughly 10% of the evolution phase (Johnstone et al., 2021). Even the troughs of the (lowest activity tracks) variable X-ray evolution are significantly higher than the measured luminosity, showing that GJ 357 b is exceptionally inactive. However, though unlikely for a random sample, it is possible that GJ 357 was observed in an unusually quiescent period and that the long-term average is somewhat higher.

Modirrousta-Galian et al. (2020) estimated a minimum age of 5 Gyrs for GJ 357 based on the lower-bound X-ray activity track for a homogeneous grouping of M-dwarfs from Penz and Micela (2008), but this method of estimation does not account for GJ 357 being a mid-M star (M2.5V). We can estimate the age of GJ 357 based on when the rotation period from MORS evolves to that observed of roughly 80 days, which yields roughly 2.3 Gyrs. However,

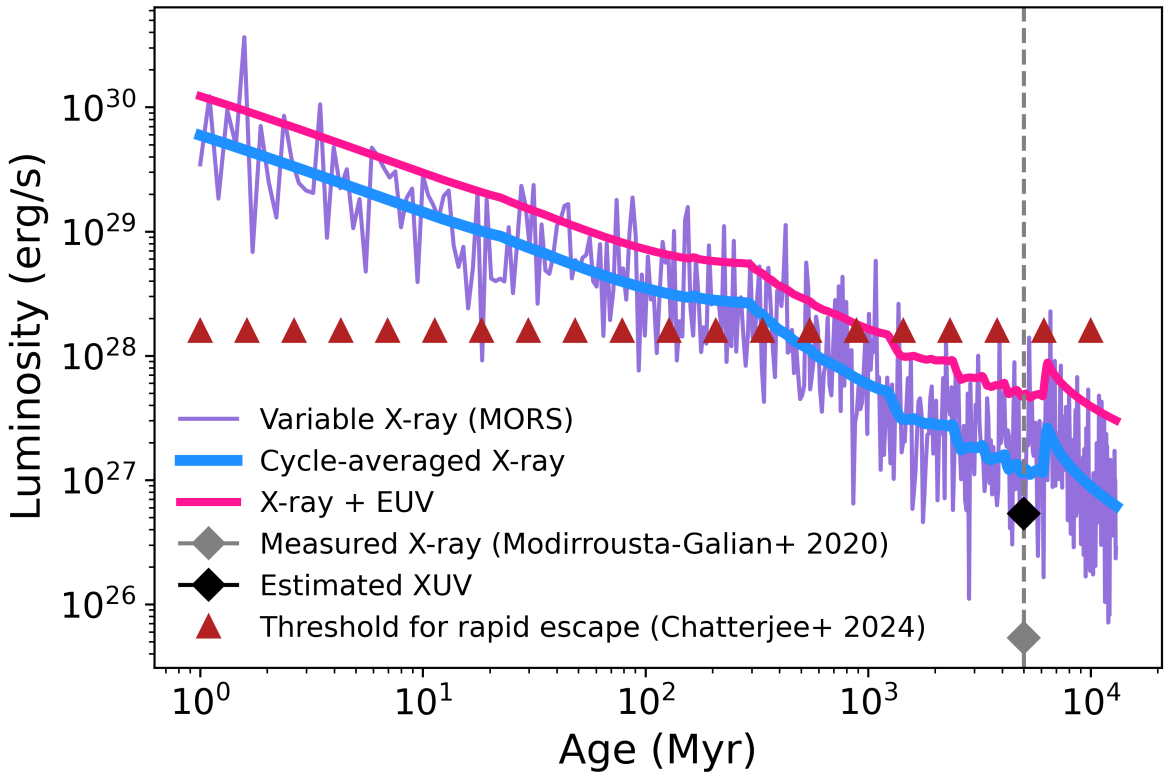

Fig. 4.1 Models of the evolution of the luminosity of GJ 357 in the X-ray and EUV bands. The *XMM-Newton measurement* of the X-luminosity (grey diamond) with the estimated age of 5 Gyrs are taken from Modirrousta-Galian et al. (2020). The XUV luminosity (black diamond) is estimated from the *XMM-Newton* measurement using scaling relationships from Johnstone et al. (2021). In blue, is the cycle-averaged lowest-activity X-ray track in the evolution of a model cluster of stars of mass $0.34 M_{\odot}$ in MORS (Johnstone et al., 2021). The threshold in the XUV luminosity for GJ 357 to drive the hypothetical transonic outflow of a secondary atmosphere on planet b is roughly $10^{28.2}$ erg/s. The MORS XUV luminosity (in pink) drops below the threshold for rapid escape (Chatterjee and Pierrehumbert, 2024) at approximately 10^3 Myrs.

given the MORS discrepancy with the measured X-ray luminosity, this estimate is also flawed. Finally, we can compare the observed $\log R'_{HK} = 5.53$ activity proxy (Marvin et al., 2023) to trends in an up-to-date M-dwarf sample from Engle (2023) to estimate a mean minimum age of 4 Gyrs.

Applying the model from (Chatterjee and Pierrehumbert, 2024, see Chapter 3) to an upper atmosphere on GJ 357 b dominated by carbon and oxygen, we find the threshold in ionising radiation to drive transonic escape is $\sim 10^3 F_{\mathrm{xuv},\oplus}$ with a rate of roughly a bar per two million years, where the present XUV flux at Earth is given by $F_{\mathrm{xuv},\oplus} \approx 4 \times 10^{-3}\,\mathrm{W\,m^{-2}}$. Note that if we instead took the lower bound on the mass of GJ 357 b of $1.53 M_\oplus$, the threshold would be reduced by less than a factor of 2, which is not enough to change the conclusions made here. Overall, the threshold estimate represents a middle ground between an extrapolation of **?**, which suggests rapid escape would not occur, and the range of atmospheric heating and dynamics that could enhance escape efficiency (e.g., Cohen et al., 2024). Thus, we argue that the possibility of buildup of a secondary atmosphere is limited to when GJ 357 b is old enough that ionising radiation fluxes have decayed significantly below the best estimate for the threshold for transonic escape (see Figure 4.1).

The cycle-averaged XUV luminosity from MORS does not meet the model threshold for bulk escape after one billion years (Fig 4.1). On taking into account the XUV variability, the MORS track would meet the threshold periodically afterwards. Thus, based on the *model* low-activity track for a star with the same mass as GJ 357 b, an accumulation of tens of millions of years meeting the threshold could lead to tens of bars of outgassed CO_2 being lost, making revival of a secondary atmosphere difficult. However, the *measured* exceptionally low activity means that the cycle-averaged XUV luminosity should have becomes sub-threshold earlier and the steeper time-decay required should severely limit the ability of variability to contribute rapid escape over billions of years. So GJ 357 is significantly more conducive to a retained secondary atmosphere compared to other M2.5V stars.

Flares are implicitly included in MORS but not in a time-resolved manner (Johnstone et al., 2021). High energy M-dwarf flares have been observed as more frequent and energetic than for the Sun (e.g. Loyd et al., 2018). However, even averages of measurements over hours lose resolution of flares due to extremely short cycles— Magaudda et al. (2022) found X-ray luminosities steady to within a factor of 2 for a large sample. So, in-depth studies of individual objects must be relied on, yielding an uncertain picture. One example of this is Barnard's star with an analysis of *Chandra* observations finding XUV fluxes raised by an average factor of 5 about 25% of the time compared to a flare-free state despite the star's advanced age of 10 Gyr (France et al., 2020). Although an equivalent flare enhancement on GJ 357 would still be insufficient to meet the threshold for rapid escape on its planet b, the result shows how the average XUV luminosity must be taken with variability on several timescales. Diamond-Lowe et al. (2024) see a peak X-ray luminosity enhanced by roughly an order of magnitude on M-dwarfs GJ 486 and LT 1445A resolved on a ksec timescale. But Diamond-Lowe et al. (2024) are unable to estimate an X-ray flare frequency and note that extrapolations to the EUV spectrum based on current models are likely to be overestimated, so again, it is unclear if a corresponding XUV variability on GJ 357 b would entail significant rapid escape.

4.2.2 Possible Evolution to a Retained Atmosphere

In the saturated phase, the loss of a massive primordial hydrogen envelope could strip a planet down to a bare rock. At this stage, volatile escape becomes limited by the rate of outgassing until XUV irradiation decreases below the threshold for rapid photoevaporation. Once this occurs, an atmosphere can gradually accumulate through volcanic activity. Noting that the MORS track significantly overestimates the present X-ray luminosity (Fig 4.1), we estimate that from 500 – 2000 Myr, a growing secondary atmosphere would likely only leak mass to space rather than escape as a hydrodynamic wind.

The predominant leak of atmospheric mass is likely to be from stellar wind erosion. To estimate this effect, we compare GJ 357 to the similar-sized but significantly more active star GJ 414 ($0.39 M_{\odot}$), for which an upper bound on stellar mass loss is constrained to be less than 10% of the Sun's rate (Wood et al., 2021). This upper bound aligns closely with the best estimate for the mass loss rate of TRAPPIST-1 (Dong et al., 2018). Accordingly, we infer the atmospheric escape rate by scaling from magnetohydrodynamic simulations of TRAPPIST-1 b's erosion at 1 bar/Gyr (Dong et al., 2018; Canto and Raga, 1991), adjusting for the $\sim 1/9$ lower wind flux at the $\sim 3\times$ greater semi-major axis of GJ 357 b. Finally, given that stellar wind strength is reduced around less active stars (Wood et al., 2021), we estimate that, GJ 357 b's atmospheric erosion rate would remain well below 0.1 bar/Gyr once on the main-sequence.

For a $1.84 M_{\oplus}$ stagnant-lid planet Dorn et al. (2018) find outgassing rates of ~ 10 bar/Gyr for an initial Earth-like mass concentration of radiogenic elements but with considerable sensitivity to various mantle properties. This is similar to the volcanism rate of Earth's midocean ridges, which was adopted by Kite and Barnett (2020) with scaling proportional to mantle depletion. Even though there is significant uncertainty, that the best guess for supply exceeds loss by two orders of magnitude provides some confidence that revival is a distinct possibility. Thus, from the perspective of star-planet interaction and evolution, it is possible that an atmosphere of several to several tens of bars is retained today.

4.2.3 Limitations

Along with the uncertain dynamics of rapid escape of secondary atmospheres, there are two major unknowns in this analysis. First, our modelling cannot rule out airlessness due to the possibility that GJ 357 is frequently in a highly energetic flare state (e.g. France et al., 2020; Diamond-Lowe et al., 2024). Though flares represent less of a problem for GJ 357 b than the overall M-dwarf rocky planet population due to the sub-threshold characteristics

already discussed. Second, a mantle depleted during the early phase of volatile loss could, in principle, entail later outgassing reduced to $\lesssim 0.1$ bar/Gyr. Krissansen-Totton et al. (2024) modelled how a long-lived magma ocean on TRAPPIST-1 b enabled catastrophic depletion of the mantle via photoevaporation. However, we note that present-day XUV irradiation of GJ 357 b is two orders of magnitude lower than at TRAPPIST-1 b and it would have seen a much shorter and less intense saturated phase, so an extrapolation to similar depletion would be pessimistic.

4.3 Escape in the L 98-59 system

L 98-59 is a bright M3V star hosting at least three transiting planets (Demangeon et al., 2021; Rajpaul et al., 2024). Planet d is an underdense super-Earth on an eccentric orbit so an atmosphere and tidal heating are expected. Gressier et al. (2024b) and Banerjee et al. (2024) observed the super-Earth L 98-59 d in transmission with JWST NIRspec, rejecting a flat line and finding strong evidence of a sulphur-dominated atmosphere, though stopping short of claiming a detection. (Bello-Arufe et al., 2025a) observed the rocky sub-Venus with a Bayesian retrieval finding strong evidence for an SO_2 atmosphere, but were to reject a flat line with frequentist statistics. Both situations would likely require extreme sulphur inventories of weight percent or more, which has precedence in the composition of Mercury (Namur et al., 2016) and enstatite chondrites (Keil, 1989).

We analyse the history of ionizing irradiation in the L 98-59 system to constrain the resulting escape of both primary and secondary atmospheres and to provide context for the atmospheric regulation of eccentricity-driven tidal heating (Nicholls et al., 2025a). Our approach incorporates the MORS model for stellar rotational evolution (Johnstone et al., 2021) and calculates energy-limited escape rates (Watson et al., 1981; Lehmer and Catling, 2017). We assume a low escape efficiency of $\eta = 10\%$, which corresponds well to hydrogen dominated atmospheres enriched in effective molecular coolants, such as water and hydrox-

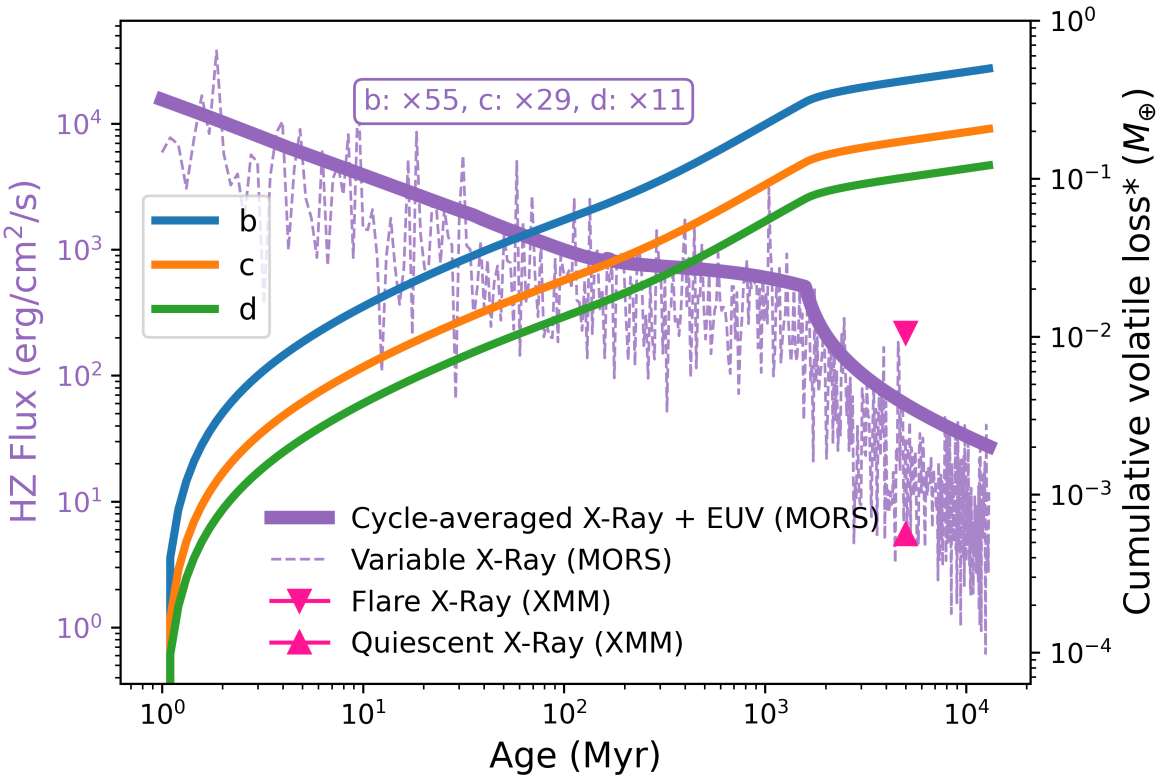

Fig. 4.2 Cycle-averaged XUV energy flux (solid purple line) and variable X-ray flux (dashed purple line) over time, scaled to a median habitable zone orbit of 0.163 AU. L 98-59 b/c/d experience 55, 29, and 11 times more XUV radiation flux than the habitable zone, respectively. Cumulative volatile losses for each planet (blue, orange, green lines) are plotted on the same time-axis. The cumulative volatile loss is an expression of the XUV fluence received by each planet, converted through an energy limited calculation.

ide (Yoshida et al., 2024). And an effective planetary cross section to incoming XUV flux at twice the present day transit cross section. Additionally, we consider XUV flux thresholds for the rapid escape of secondary atmospheres (Chatterjee and Pierrehumbert, 2024).

Accounting for long-term stellar variability, we show that the predicted X-ray flux displayed in Fig. 4.2 is consistent with XMM Newton measurements of the quiescent and flare states of L 98-59 (Behr et al., 2023). The solid purple line in Fig. 4.2 indicates that the cycle-averaged XUV flux in the habitable zone decreases from $10^{3.5}\times F_{\mathrm{XUV},\oplus}$ at birth to $10\times$ at 5 Gyr, where the present XUV flux at Earth is given by $F_{\mathrm{xuv},\oplus}\approx 4\times10^{-3}\,\mathrm{W\,m^{-2}}$. At the orbits of L 98-59 b/c/d, the XUV fluxes at 5 Gyr are $550\times$, $300\times$ and $100\times$ $F_{\mathrm{XUV},\oplus}$ respectively. These levels are sufficient for any hydrogen-dominated envelope hosted by b/c/d to undergo rapid escape up to the present day (Chatterjee and Pierrehumbert, 2024). To illustrate the intensity of escape, we plot the potential for cumulative volatile losses for planets of b/c/d, equivalent to roughly 40%, 16% and 10% of Earth's mass over 5 Gyr (Fig. 4.2). These large losses mean that hydrogen and metals are likely to have escaped from L 98-59 b, while escape from planets c/d may allow the retention of metals.

The only mechanism thought to provide significant protection from photoevaporation at such high XUV fluxes is the line cooling of metal atoms, as found by Nakayama et al. (2022) for an atmosphere similar to present-day Earth. This feature of cooling-limited escape could be crucial to the plausibility of atmospheric retention on super-Earths L 98-59 c/d. A comparison with the XUV threshold calculated for LHS 1140 c in Chatterjee and Pierrehumbert (2024), which is similar in gravitational binding to L 98-59 c/d, suggests that rapid escape of a metal-dominated atmosphere may not occur presently while the star is within a quiescent period. However, during flaring events, the XUV flux could increase by more than an order of magnitude, potentially triggering episodic rapid escape. Previous observations of M-dwarfs have found flare duty cycles up to 25% (France et al., 2020; Nicholls et al., 2023; Venot et al., 2016).

For the sub-Venus L 98-59 b, atmospheric escape of SO_2 is expected to fall between the Earth-like and Mars-like regimes explored in Chatterjee and Pierrehumbert (2024), where atomic line cooling fractionally reduces efficiency in the energy-limit. Consequently, at the present-day XUV flux shown in Fig. 4.2, the energy-limited escape of primary or secondary atmospheres will be comparable, with a shared conservative escape rate of approximately 15 bar/Myr. Over 5 billion years, the mass of a continuously escaping atmosphere would exceed the mass of the planet. For comparison, Bello-Arufe et al. (2025b) estimate an escape rate of 1 bar/Myr for secondary SO2 atmospheres, assuming a 1% efficiency as a lower bound.

We further modelled L 98-59 d, with a consistent time evolution of the planetary cross section to XUV, finding that initialisation with a huge hybrid atmosphere (wt percent in both hydrogen and sulphur) is consistent with present-day conditions (Nicholls et al., 2025c). However, the observations of L 98-59 b remain a puzzle— it is hard to conceive of a coupled interior-escape evolution whereby an SO_2 atmosphere survives or is revived to 5 billion years. These planets are also targets under consideration for the Rocky Worlds DDT and are considered in the following section.

4.4 Revisiting the Cosmic Shoreline

So far this chapter has presented individual cases of escape of rocky exoplanet atmospheres in the high-energy environment of evolving M-dwarfs. The next step is to consider the loss and survival of atmospheres in the population of rocky exoplanets as whole. Our aim is to identify where secondary atmospheres survive once time-integrated hydrodynamic loss is compared against initial volatile inventories. Ji et al. (2025) comprehensively revisit the cosmic shoreline by varying atmospheric escape prescriptions, volatile compositions and abundances in a Monte Carlo framework to show that a universal clear-cut shoreline is difficult to justify. We report here those simulations from Ji et al. (2025) directly based on the models reported in Chapters 2 & 3.

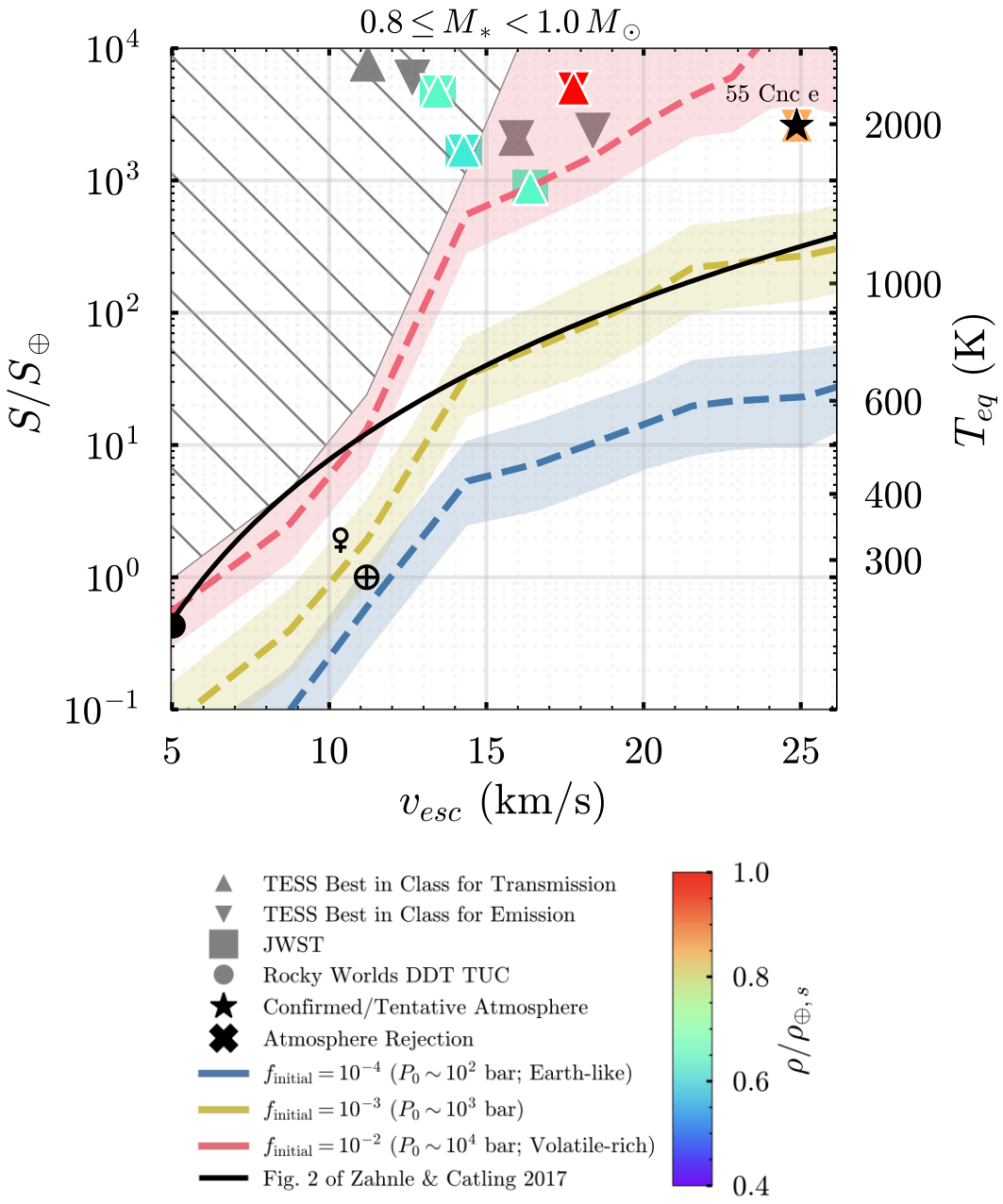

Fig. 4.3 Late G-dwarf and Early K-dwarf cosmic shorelines: Critical instellations for atmospheric retention vs planetary escape velocity probing a range of volatile abundances and uncertainties. Blue, yellow, and red lines mark the 90 % retention probability for initial volatile fractions of 10^{-4}, 10^{-3}, and 10^{-2} of the planetary mass, respectively. The shaded areas in each color show where the retention probability ranges from 50–99%. The $I_{\rm XUV} \propto v_{\rm esc}^4$ (Zahnle and Catling, 2017) is shown intersecting Mars in black. Highlighted are planets that are "best-in-class" for transmission and emission spectroscopy (Kempton et al., 2018; Hord et al., 2024), JWST targets (Nikolov et al., 2022) and DDT targets (Redfield et al., 2024). Planets are coloured by their density relative to Earth, accounting for gravitational compression, as shown in the colour bar. Where no mass measurement is available planets are coloured grey. The super-Earth 55 Cancri e has a tentative detection of a variable atmosphere (Hu et al., 2024).

$M_{p,\star}$ ($M_\oplus$)	0.11	1.00	1.9	5.6
$F_{xuv,\star}$ ($F_{xuv,\oplus}$)	50	400	1000	2000
Loss Rate, $\dot{C}_\star$ (kg/s)	3×10^5	10^6	2.2×10^5	3.4×10^5
Loss Rate per Surface Area (kg/m^2/s)	2.3×10^{-9}	2.0×10^{-9}	3.1×10^{-10}	2.6×10^{-10}
Energy Limited Range of F_{xuv} ($F_{xuv,\oplus}$)	5 – 500	126.5 – 1264.9	501.2 – 1995.2	1954.5 – 2046.6
	5 – 5000	126.5 – 12649.1	501.2 – 19952.6	1954.5 – 20465.8

Table 4.1 Adjusted escape rates from Chatterjee and Pierrehumbert (2024) for constraining an approximately energy limited regime of an N2-dominated atmosphere. Atmospheric escape rate as a function of XUV flux follows three regimes: negligible at low flux, energy-limited and proportional at intermediate flux (energy limited regime), and plateau at high flux due to atomic cooling. $F_{\mathrm{xuv},\star}$ (in units of Earth's present-day XUV flux, $F_{\mathrm{xuv},\oplus}$) and $\dot{C}_\star$ represent a reference point within the energy-limited regime. For F_{xuv} within the energy limited regime, the escape rate scales linearly: $\dot{C} = \dot{C}_\star \cdot \left(F_{xuv}/F_{xuv,\star}\right)$. The last two rows indicate the upper and lower limits of where the energy-limited regime transitions to the saturation regime, which corresponds to an uncertainty of a factor of 10.

Atmospheric retention depends on many factors beyond XUV irradiation, particularly the planet's initial volatile inventory. The observed "radius valley" (Fulton et al., 2017) implies that a gas-rich formation scenario may be the norm (Rogers and Owen, 2021). However, around M dwarfs, close-in sub-Neptunes are comparatively rare (Ment and Charbonneau, 2023). Coupled evolutionary modelling (Nicholls et al., 2025c) to reproduce the observed atmosphere of L 98-59 d required unusually large primordial inventories of sulphur (mass fractions exceeding 1%) and long-term volatile storage in a magma ocean (Dorn and Lichtenberg, 2021).

A broader point is that a life-supporting atmosphere may be limited to surface pressures of order 1 bar (Lammer et al., 2019). If retention from birth requires a much thicker volatile envelope, this creates a fine-tuning problem: rapid escape must either halt precisely when only a few bars remain or be replenished to the right thickness and composition. The simplest way to avoid this is for the planet to form around a slowly rotating Sun-like star, such that the XUV flux never exceeds the threshold for transonic escape of a secondary atmosphere. However, such a planet would lie beyond the observational reach of *JWST*.

Ji et al. (2025) perform a logistic regression analysis to determine the critical instellation at which a planet has a 99%, 90%, and 50% probability of retaining an atmosphere, which we

use to define the lower, middle, and upper bounds of the shaded region. For a given volatile abundance, instellations below these thresholds correspond to atmospheres that should be retained, while those above indicate a probable airlessness. We do not extend to a 1 % retention contour, since our aim is to probe planets across a wide age range and recover a genuine instellation–escape velocity parametrisation.

We reinterpret the cosmic shoreline and add physically motivated bounds on escape, guided by the results of Chapters 2 and 3, but rather than try to directly adopt the collisional–radiative thermostat formulation, we translate the key features into a simple parametrisation:

- *XUV flux and escape rate at transonic onset:* The fiducial values we implement for the escape rate are drawn from the tabulated onset solutions in Table 3.1, corresponding to the collisional Knudsen onset for Mars–to–Earth sized planets and the thermostat onset for super–Earths. For intermediate masses we linearly interpolate between the tabulated points. Although the dynamics at onset are not strictly energy–limited, this diagnostic follows the precedent of Ito and Ikoma (2020) in connecting to the more familiar energy budget picture.

- *Probe of subsonic onset:* Available hydrocode and DSMC studies suggest that appreciable escape can occur below the formal transonic threshold when advection dominates the energy balance. To capture this, we backward–extrapolate the onset curves into a low–flux regime. The steepness of this extrapolation is made mass–dependent: more massive planets require higher escape temperatures and experience stronger atomic line cooling, so the subsonic branch rises more sharply with flux. Understanding the onset of rapid escape, requires detailed molecular-kinetic simulations, with some preliminary discussion and results provided in Chapter 5.

- *Uncertain plateau of escape rate:* At high XUV fluxes, escape rates should not grow without bound. Based on the collisional-radiative thermost and saturation of the

ionisation fraction and total density at the sonic point, we implement a high-XUV-flux plateau in escape rate. The exact height and breadth of this plateau remain uncertain, so in practice we randomise the plateau value within the bounds listed in Table 4.1, probing this uncertainty through our Monte Carlo sampling.

Ji et al. (2025) consider a simple energy-limited solution and the thermospheric solutions from Tian et al. (2009); Tian (2009). The semi-analytic prescription implemented here can be thought of as the energy-limit accounting for non-linear behaviour through a threshold and a plateau motivated by available models.

We model stellar evolution using the bolometric luminosities and radii of Baraffe et al. (2015) together with stellar age distributions from Berger et al. (2020), imposing a maximum age $\tau_{\max}(M_*) = 10^{10}(M_*/M_\odot)^{-2.5}$ yr.For XUV evolution we sample between two prescriptions with equal probability : (i) Selsis et al. (2007) based on *ROSAT* data, which assumes a fixed saturation ratio $L_X/L_{\rm bol} = 10^{-3.2}$ followed by a power-law decline with constant index; and (ii) combining Jackson et al. (2012) (*ROSAT, Chandra, XMM–Newton*) above 0.5 $M_\odot$ and Guinan et al. (2016) (*HST, Chandra*) below 0.5 $M_\odot$, where both the saturation level and decline slope vary with stellar mass. Soft and hard EUV fluxes are estimated from X-ray measurements using the empirical scalings of King and Wheatley (2020), calibrated against solar *TIMED/SEE* data and stellar *EUVE* observations, with liberal uncertainties propagated through Monte Carlo sampling. To better understand the EUV emission of M dwarfs, there is a need for an EUV space observatory (France et al., 2022). Planet formation times are drawn log-uniformly between 10^6 and 10^8 yr.

Figures 4.3–4.7 show the hydrodynamic cosmic shorelines across stellar types. The volatile-rich shorelines (1 % by mass) are significantly more optimistic than the original $I_{\rm XUV} \propto v_{\rm esc}^4$ relation (Zahnle and Catling, 2017), whereas the volatile-poor shorelines are more pessimistic. Because of this degeneracy, we do not attempt a quantitative reassessment of "how much" retention has shifted; instead we highlight the most salient

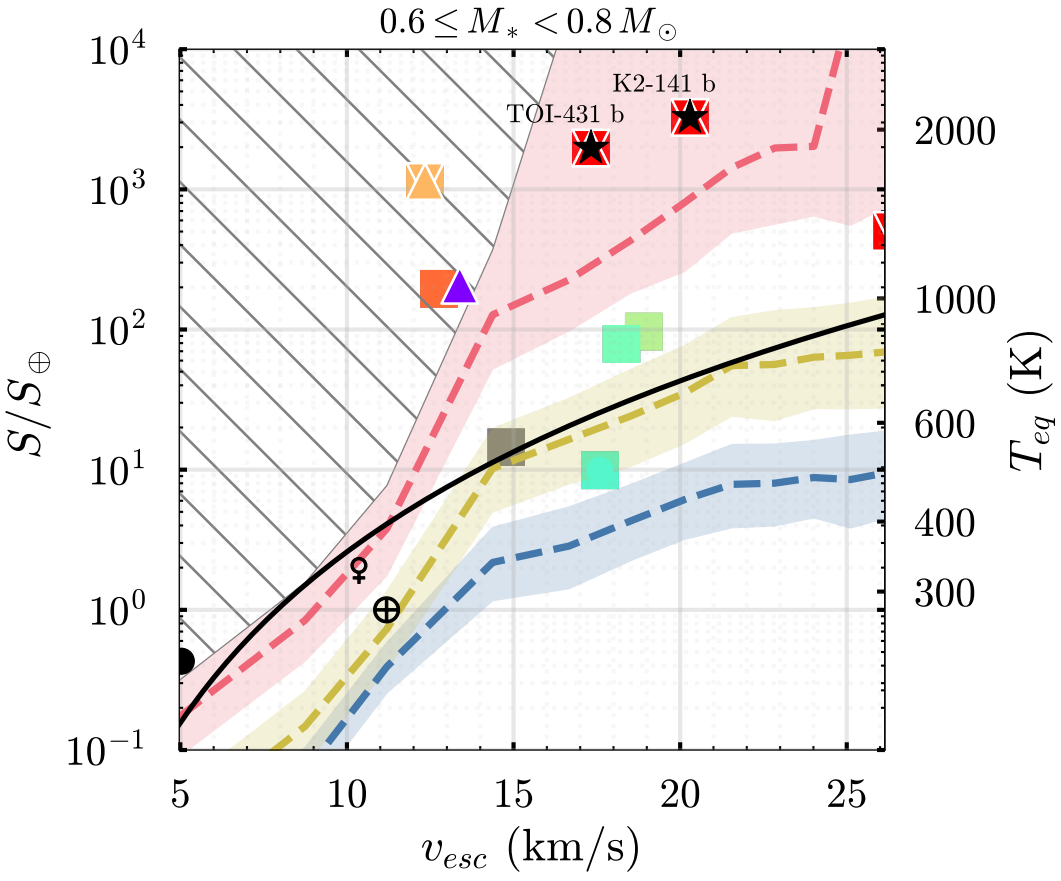

Fig. 4.4 Late-K dwarf Cosmic Shorelines: K2-141 b (*Spitzer*; Zieba et al., 2022) and TOI-431 b (Monaghan et al., 2025) have emission spectra that disfavour a bare rock scenario, implying the possible presence of an atmosphere. See Figure 4.3 for legend.

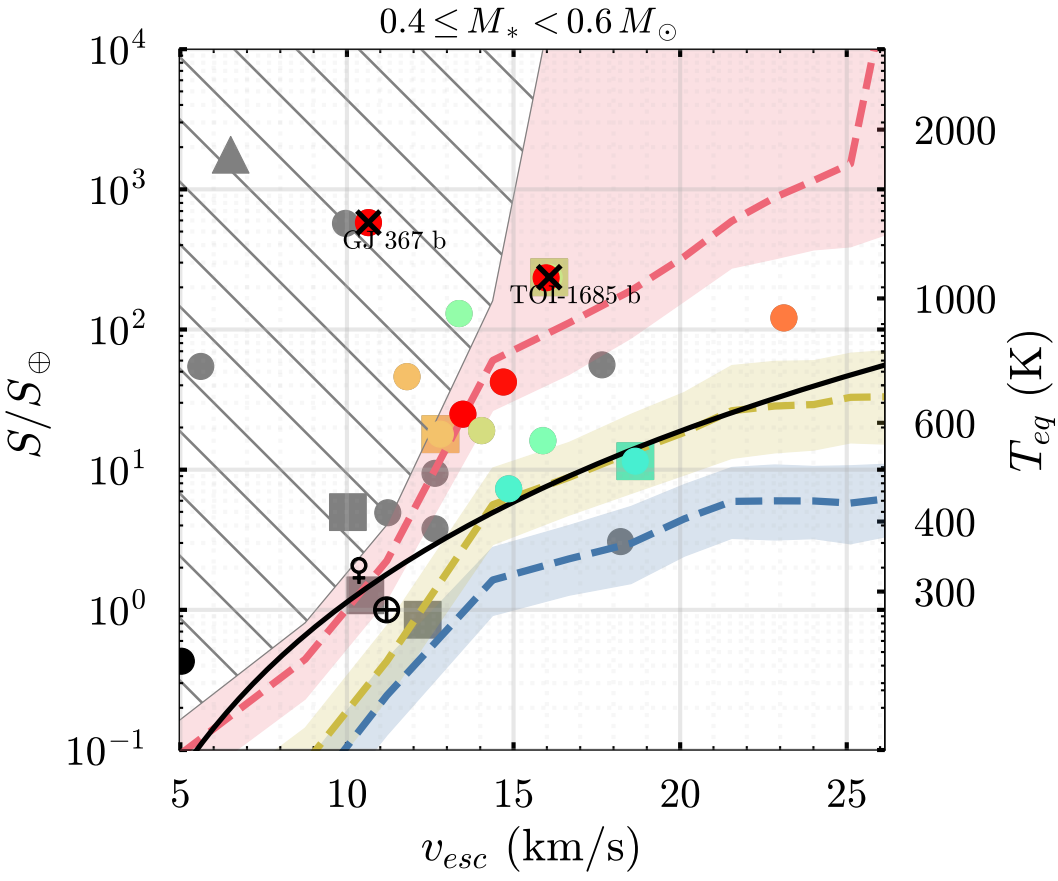

Fig. 4.5 Early-to-Mid M dwarf Cosmic Shorlines: GJ 367 b (Zhang et al., 2024) and TOI-1685 b (Luque et al., 2025; Fisher et al., 2025) have spectra consistent with bare rocks. See Figure 4.3 for the shared legend and its explanation.

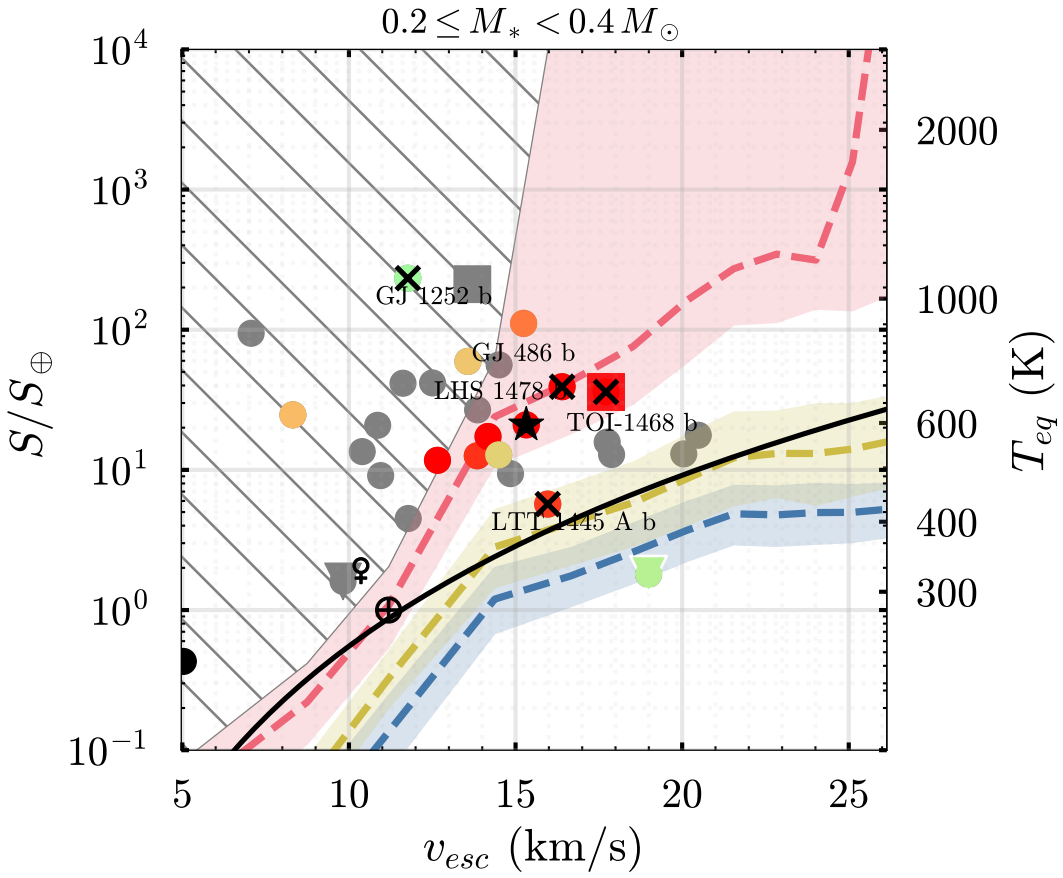

Fig. 4.6 Mid M-dwarf cosmic shorelines: GJ 1252 b (*Spitzer*; Crossfield et al., 2022), GJ 486 b (Mansfield et al., 2024), TOI-1468 b (Meier Valdés et al., 2025) and LTT 1445A b (Wachiraphan et al., 2025) have emission spectra consistent with bare rocks. The leftmost red point is GJ 357 b, which, as discussed in Section 4.2, has potential for volcanic revival on the main sequence due to its exceptionally low activity (Taylor et al., 2025). See Figure 4.3 for the shared legend and its explanation.

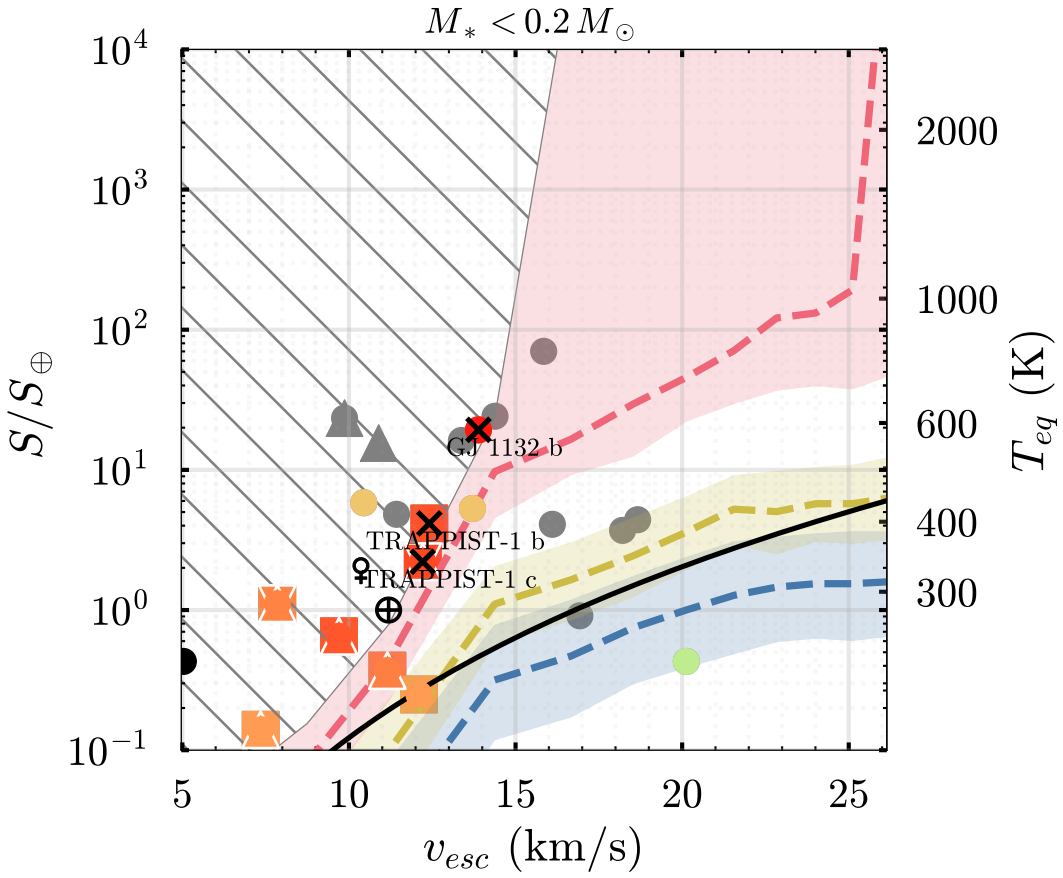

Fig. 4.7 Late-M dwarf cosmic shorelines: TRAPPIST-1 b and c (Ducrot et al., 2024; Gillon, 2024), and GJ 1132 b (Xue et al., 2024) have emission spectra consistent with a bare rocks, while atmospheres >1 bar have been ruled out for TRAPPIST-1 d (Piaulet-Ghorayeb et al., 2025). Above and below Earth's escape velocity, the $I_{\rm XUV} \propto v_{\rm esc}^4$ (Zahnle and Catling, 2017) hugs the 0.01 wt % (blue) and 0.1 wt % (yellow) volatile shorelines. See Figure 4.3 for the shared legend and its explanation.

qualitative changes. For a detailed intercomparison, the reader can refer to Ji et al. (2025), where a new metric for atmospheric retention is introduced and TOI-4559 b and TOI-771 b are identified as potentially rocky, high-observability targets that are likely to retain atmospheres.

One clear improvement over the original shoreline concerns the ultra-short-period planets with tentative atmospheric detections. K2-141 b (5.1 $M_\oplus$, 1.5 $R_\oplus$; 0.71 $M_\odot$), 55 Cancri e (8.8 $M_\oplus$, 1.9 $R_\oplus$; 0.91 $M_\odot$), and TOI-431 b (3.0 $M_\oplus$, 1.3 $R_\oplus$; 0.78 $M_\odot$) (Zieba et al., 2022; Hu et al., 2024; Monaghan et al., 2025) lie beyond the traditional cosmic shoreline yet remain below our airless boundary if they began with a volatile mass fraction of ~1 %. The detections are marginal, and for lower volatile fractions the shorelines indicate that these planets can still lose their atmospheres over time; however, such tightly bound atmospheres may be even more protected by efficient atomic-line cooling than estimated here.

The broader rocky-planet sample tells a mostly consistent story. Around late M dwarfs (Fig. 4.7), TRAPPIST-1 b (1.4 $M_\oplus$, 1.1 $R_\oplus$; 0.09 $M_\odot$) and c (1.3 $M_\oplus$, 1.1 $R_\oplus$), and GJ 1132 b (1.6 $M_\oplus$, 1.2 $R_\oplus$; 0.18 $M_\odot$) are consistent with bare rocks; for TRAPPIST-1 d (0.39 $M_\oplus$, 0.77 $R_\oplus$), atmospheres $\gtrsim$1 bar are ruled out (Ducrot et al., 2024; Gillon, 2024; Xue et al., 2024; Piaulet-Ghorayeb et al., 2025). Across early–mid M dwarfs, additional planets that have probably lost their atmospheres include GJ 1252 b (2.1 $M_\oplus$, 1.2 $R_\oplus$; 0.38 $M_\odot$), GJ 486 b (2.8 $M_\oplus$, 1.3 $R_\oplus$; 0.33 $M_\odot$), TOI-1468 b (2.6 $M_\oplus$, 1.2 $R_\oplus$; 0.55 $M_\odot$), and LTT 1445A b (2.9 $M_\oplus$, 1.3 $R_\oplus$; 0.26 $M_\odot$) (Crossfield et al., 2022; Mansfield et al., 2024; Meier Valdés et al., 2025; Wachiraphan et al., 2025). For G- and K-dwarf hosts, only the ultra-short-period population is currently within observational reach. An exception among M-dwarf systems is LHS 1478 b (2.3 $M_\oplus$, 1.2 $R_\oplus$; 0.33 $M_\odot$), which disfavors a bare-rock scenario at the 2–3σ level (August et al., 2024; Connors et al., 2025; August et al., 2025). Apart from LHS 1478 b and the ultra-short-period GK planets, the shorelines suggest that a 1 % volatile mass fraction is too large to be typical.

Because escape rates depend nonlinearly on XUV flux, cumulative loss is controlled by both the total exposure and the time history of stellar XUV. The sub-Earth shorelines bunch more tightly than a simple energy-limited scaling with instellation would predict, especially for late M dwarfs, owing to the nonlinear threshold for rapid escape. For late M dwarfs, the saturation phase is long and the subsequent decline gradual; as a result, only a factor of ~2 in instellation separates loss of 100 bar from 1,000 bar, or 1,000 bar from 10,000 bar. Thus, across two orders of magnitude in volatile mass—from $10^{-4}M_p$ to $10^{-2}M_p$—the critical instellations differ by less than an order of magnitude.

In hydrodynamic escape models, the shoreline's scaling with escape velocity is not uniform. With increasing stellar mass, the shoreline shifts toward higher instellation—not only because higher-mass stars deliver lower cumulative XUV (Zahnle and Catling, 2017), but also because of nonlinearities in how escape responds to XUV forcing. Moreover, atomic-line cooling can render volatile-rich super-Earths remarkably resilient to catastrophic photoevaporation even on close-in orbits around low-mass stars.

The original shoreline already pointed toward targeting more massive, less-irradiated super-Earths; the hydrodynamic shorelines strengthen that guidance. A notable nuance is that, although lower-mass stars are generally favorable, more massive super-Earths around such stars remain compelling because of the plateau associated with the collisional–radiative thermostat—a poorly understood regime that merits observation.

The cosmic shoreline hypothesis can develop with results from theory and observations. A first revision is a two-stage shoreline, reflecting the distinct physics of the hydrodynamic escape of secondary atmospheres from sub-Earths and super-Earths. Though nonlinear escape physics reduces sensitivity to initial volatile inventory, the framework may be better cast in terms of volatile-rich and volatile-poor branches; that is, unless the volatile-mass-fraction distribution of rocky exoplanets proves unimodal. A significant unknown arises from leading hydrodynamic studies of high-molecular-weight atmospheres having yet to

include intrinsic planetary magnetic fields, which could further bifurcate the shorelines. In the next section, we present a novel analysis of the impact of magnetic on atmospheric retention on rocky exoplanets (to be reported also in Meier et al. 2025).

4.5 Magnetic Suppression of Rapid Escape

The population of long-lived planetary dynamos may significantly deform or override the umagnetised cosmic shoreline. The degree to which planetary magnetism can protect super-Earth secondary atmospheres against escape when atmospheric temperatures are regulated by with the electron-impact excitation of atomic lines (Nakayama et al., 2022) has not been explored. A comprehensive analysis is beyond the scope of this thesis, but we suggest a few key points here.

We have shown how predominantly neutral escape of secondary atmospheres from super-Earths would require upper atmosphere temperatures significantly in excess of 20,000 K, which would be prohibited by efficient atomic line cooling. But for large XUV fluxes, predominantly ionised outflow can be driven at roughly half-as-high temperatures due to the ambipolar electrostatic field from buoyant electrons boosting escape. However, in the presence of a planetary dynamo the charge separation of ions and electron can only occur parallel to magnetic field lines, precluding radial acceleration in the closed-field regions found at low latitudes. So, XUV-driven ion outflow can only occur along the open magnetic field lines at the poles. Thus, mass loss should be greatly suppressed, and in this regime a magnetic field can be considered *a priori* protective, akin to the analysis of Owen and Adams (2014) for hot Jupiters. We note that such escape rates still exceed the classical polar wind considered in the Earth context where sound speed is reached by collisionless acceleration above the ion-exobase (Yau et al., 2007). Here, the photoionisation conditions are extreme enough such the sonic point occurs at a denser collisional altitude of the polar region.

Our suggestion of effective magnetic suppression of rapid escape contrasts with the recent view—grounded in comparative studies of present-day escape rates for Earth, Mars, and Venus (Strangeway et al., 2010; Gunell, Herbert et al., 2018; Gronoff et al., 2020a)—that intrinsic magnetism can just as readily enhance as inhibit escape rates. Only when non-thermal processes dominate (e.g. stellar-wind erosion) does it appear that the net benefit of a long-lived dynamo become uncertain. The work reported in this thesis, particularly the role of the plasma escape temperature in the collisional radiative thermostat (Fig 3.5), highlights how magnetic fields may strongly influence the loss and retention of rocky exoplanet atmospheres.

4.6 Summary

This chapter offers a broad assessment of secondary atmosphere loss and retention. The first section, reported in Taylor et al. (2025), marks the first consideration of the possibility of volcanic revival of a secondary atmosphere of a super-Earth that accounts for the effects of atomic line cooling. The second section looks at a comparison of rates of volcanism to support a highly marginal atmospheric detection on L 98-59 b (Bello-Arufe et al., 2025b), but are in fact implausible when integrated over the planetary lifetime as reported in Nicholls et al. (2025b). The third section reports a selection of results from Ji et al. (2025), which marks the first population study of escape of secondary atmospheres and redraws the cosmic shoreline. Finally, in the fourth section, we suggest that rocky exoplanet magnetic fields should be considered *a priori* protective against irreversible escape. To improve on the estimates made here, detailed numerical simulations are required, which is the subject of the following chapter.

5

Hydrodynamic and Molecular-Kinetic Simulations of Escape

The second part of this chapter includes results from Chatterjee et al. (2025) based on simulations run by Shane Carberry Mogan using a version of his custom-built `Harrah` *code.*

5.1 Introduction

A purely hydrodynamic description is fully adequate only when the outflow becomes transonic with the sonic point beneath the exobase, so that the collisionless exosphere cannot

communicate information upstream into the collisional flow. Even under the same boundary and heating conditions, a hydrostatic solution may also satisfy the global energy budget, because atomic line cooling operates differently when the ionisation state is set by recombination balance versus by advection. Discriminating between these possibilities requires a kinetic treatment that bridges the collisional and collisionless regimes. For subsonic "breeze" solutions, the mass-loss rate is set by the transition where the Knudsen number is of order unity, provided the outer atmosphere is not confined by interplanetary pressure or by a stellar-wind bow shock. Accordingly, Section 5.2 develops a scheme to integrate the spherically symmetric compressible Euler equations as an initial-value problem, and Section 5.3 implements direct molecular-kinetic simulations (DSMC) as an approximation to the Boltzmann equation. The simulations presented here are preliminary and constitute a first step towards tackling open questions in atmospheric escape with both hydrodynamic and molecular-kinetic models.

5.2 Solving Hydrodynamics with Constrained Interpolation Profiles

For hydrodynamic escape, the singular behaviour of passing through the critical point is difficult to reproduce numerically. Steady-state hydrodynamic escape can be considered as a two-point boundary problem (Press et al., 2007) and Watson et al. (1981) obtained a transonic solution via a shooting method, but its high sensitivity and reliance on trial-and-error limited its applicability as noted by Kasting and Pollack (1983), who instead resorted to subsonic 'breeze' solutions as approximations. Later, Murray-Clay et al. (2009) found that a relaxation method effectively converged to transonic solutions, experimentation with the initial conditions and set-up is still required. An alternative is to treat the equations as an initial value problem and integrate to steady state, as in Tian et al. (2005), who modelled

hydrogen escape from the early Earth using a Lax–Friedrichs scheme. However, the scheme's inherent numerical diffusion (Press et al., 2007) can spuriously propagate information into supersonic regions (O'Brien, 2017), an issue highlighted by Kuramoto et al. (2013) in their early-Earth hydrogen escape study. Their solution was to adopt the more accurate Constrained Interpolation Profile [1] (CIP) scheme (Yabe and Aoki, 1991; Yabe et al., 2001).

5.2.1 Method

Following Tian et al. (2005), we write the spherically symmetric inviscid Euler equations for a single-component atmosphere with thermal conduction:

$$\frac{\partial(\rho r^2)}{\partial t} + \frac{\partial(\rho u r^2)}{\partial r} = 0, \tag{5.1a}$$

$$\frac{\partial(\rho u r^2)}{\partial t} + \frac{\partial(\rho u^2 r^2 + p r^2)}{\partial r} = -\rho GM + 2pr, \tag{5.1b}$$

$$\frac{\partial(E r^2)}{\partial t} + \frac{\partial[(E+p)u r^2]}{\partial r} = -\rho u GM + q r^2 + \frac{\partial}{\partial r}\left(\kappa r^2 \frac{\partial T}{\partial r}\right), \tag{5.1c}$$

where ρ, T and p are the density, temperature and pressure of the atmosphere, respectively. The mass of the planet is M, G is Newton's constant ($6.67 \cdot 10^{-11}\mathrm{Nm^2kg^{-2}}$), u is the bulk radial velocity of the escaping flow, q is the heating rate per unit volume, κ the thermal conductivity, e the internal energy density and the total energy density is $E = u^2/2 + e$. These equations couple conservation of mass, momentum, and energy in spherical geometry, and form the basis for our time-dependent solver.

We follow Sasaki (2008) in our numerical implementation of the CIP scheme to solve these equations. In contrast to standard finite-difference advection schemes, which suffer from numerical diffusion or dispersive oscillations, CIP achieves higher accuracy by embedding local profile information into a cubic representation. This makes it particu-

[1] The name has changed over time to expand the set of schemes encompassed. Earlier names include cubic interpolated propagation and cubic interpolated pseudo-particle.

larly well-suited for steep atmospheric gradients where diffusion errors would otherwise smear out shocks or heating fronts. The CIP scheme propagates *both* the value or 'height' of the profile and the gradient[2] at that point to ensure maximum fidelity. We aim to solve hyperbolic equations of the form:

$$\frac{\mathrm{d}f}{\mathrm{d}t} + u\frac{\mathrm{d}f}{\mathrm{d}r} = G, \tag{5.2}$$

which can be split into two phases. The non-advection phase ignores the advective $u\frac{\mathrm{d}f}{\mathrm{d}r}$ term and solves the remaining equation with simple finite difference:

$$f_i^* = f_i^n + G\delta t^n, \tag{5.3}$$

where the time step δt is calculated using the Courant-Friedrichs-Lewy (CFL) condition:

$$\delta t^n \leq \min\left(\frac{\delta r \cdot c_{max}}{u_i^n}\right), \tag{5.4}$$

where we use $c_{max} = 1/2$. It turns out that it is useful to have the velocity staggered from the other profiles (Yabe and Aoki, 1991). The governing equations become

$$\frac{\eta_i^* - \eta_i^n}{\delta t^n} = -\eta_i^n\left(\frac{u_{i+1/2}^n - u_{i-1/2}^n}{r_{i+1} - r_i}\right), \tag{5.5a}$$

$$\frac{u_{i+1/2}^* - u_{i+1/2}^n}{\delta t^n} = \frac{2}{\rho_{i+1}^n + \rho_i^n}\frac{p_{i+1}^n - p_i^n + \nu_{i+1}^n - \nu_i^n}{r_{i+1} - r_i} - \frac{GM}{(r_{i+1/2})^2}, \tag{5.5b}$$

$$\frac{T_i^* - T_i^n}{\delta t^n \cdot (\gamma - 1)} = -T_i^n\left(\frac{u_{i+1/2}^n + u_{i-1}}{\delta r} + \frac{2u_{i+1/2}^n}{r_i}\right) + q_i^n + \frac{1}{r_i^2}\left[\kappa r_j^2 \frac{T_j^n - T_{j-1}^n}{\delta r_j}\right]_{j=i}^{j=i+1}. \tag{5.5c}$$

[2]The CIP-CSL2 was also explored and this propagates the height and the integral of the profile: the cell-integrated value (CIV). This ensures a more exact conservation of mass, but did not appear to help with numerical issues encountered, so is set aside.

where $\eta = 4\pi\rho r^2$ and ν is the explicit artificial viscosity (EAV) with dimensions of pressure:

$$\nu_i = -c_\nu \gamma \rho_i \Delta u_i \left(\sqrt{\frac{p_i^n}{\rho_i^n}} - \frac{\gamma+1}{2}\Delta u_i \right) \quad \text{if } \Delta u_i < 0\,; \;\; \text{else } \nu_i = 0, \tag{5.6}$$

with $\Delta u_i = u^n_{i+1/2} - u^n_{i-1/2}$ (Sasaki, 2008). The EAV is only added to the pressure gradient term in the momentum equation, acts only in regions of compression ($\Delta u_i < 0$) and prevents unphysical oscillations at shocks by smoothing steep velocity gradients. This is a standard modification for shock-capturing schemes in spherical geometry. The variables after the non-advection phase are denoted with a star: u^* and p^*.

We also need to ensure that the profile gradient f' is consistent with the above governing equation. The immediate way of doing this is to take the spatial derivative of Eqn. 5.2 and then solve a complicated finite-difference equation in terms of G'; picking up other terms as well. However, this would be extremely computationally expensive and prone to instability, especially for more complicated G. Instead, a judicious formulation by Yabe and Aoki (1991) is used whereby we take the differences of the old profiles with the new profiles (after one more iteration step) to find the change in gradient given by

$$f_i'^* = \frac{f^*_{i+1} - f^*_{i-1} - f^n_{i+1} + f^n_{i-1}}{2\delta r} - f_i'^n \left(1 - u_i'^n \delta t\right). \tag{5.7}$$

The next phase is advection. The advected profile and its gradient are given by

$$f_i^{n+1} = a_i \varepsilon_i^3 + b_i \varepsilon_i^2 + f_i'^* \varepsilon_i + f_i^*, \tag{5.8a}$$

$$f_i'^{n+1} = 3a_i \varepsilon_i^2 + 2b_i \varepsilon_i + f_i'^*. \tag{5.8b}$$

where $\varepsilon = -u\delta t$. The a and b coefficients that specify the cubic polynomials are calculated at each gridpoint using

$$a_i = \frac{f_i'^* + f_{iup}'^*}{\delta r_i^2} + 2\frac{f_i^* - f_{iup}^*}{\delta r_i^3}, \tag{5.9a}$$

$$b_i = 2\frac{f_i'^* + f_{iup}'^*}{\delta r_i^2} - 3\frac{f_i^* - f_{iup}^*}{\delta r_i^2}, \tag{5.9b}$$

where $\delta r_i = r_{iup} - r_i, \quad iup = i - \mathrm{sgn}(u_i)$ to deal with backward propagation that will sometimes develop. The f_i^{n+1} and $f_i'^{n+1}$ are then fed back

5.2.2 Application

We validate our implementation of the CIP scheme using a spherically symmetric generalisation of the Sod shock tube problem following Omang et al. (2006). In this setup, a high–pressure region with $p = 1.0$, $\rho = 1.0$ is separated from a low–pressure region with $p = 0.1$, $\rho = 0.125$ by a spherical membrane located at $r = 1.0$, with the gas initially at rest and an adiabatic index $\gamma = 1.4$. Once the membrane is removed, the system evolves to produce an outward–moving shock front, a contact discontinuity, and an inward–moving rarefaction wave, analogous to the planar Sod problem but with spherical divergence included. Because no analytical solution exists for the spherical case, we benchmark against the 1D Riemann solver results of Omang et al. (2006). As shown in Fig. 5.1, the CIP scheme captures the density, pressure, velocity, and energy profiles with good agreement, including the correct treatment of the spherical origin boundary. For comparison, the planar Sod shock tube produces similarly accurate results (not shown), confirming that the scheme performs reliably in both Cartesian and curvilinear geometries.

To implement significant XUV heating in the code, we adopted a staggered-grid scheme and included an explicit artificial viscosity. For sufficiently large XUV energy deposition, a transonic steady state should exist over a broad range of lower boundary conditions, but

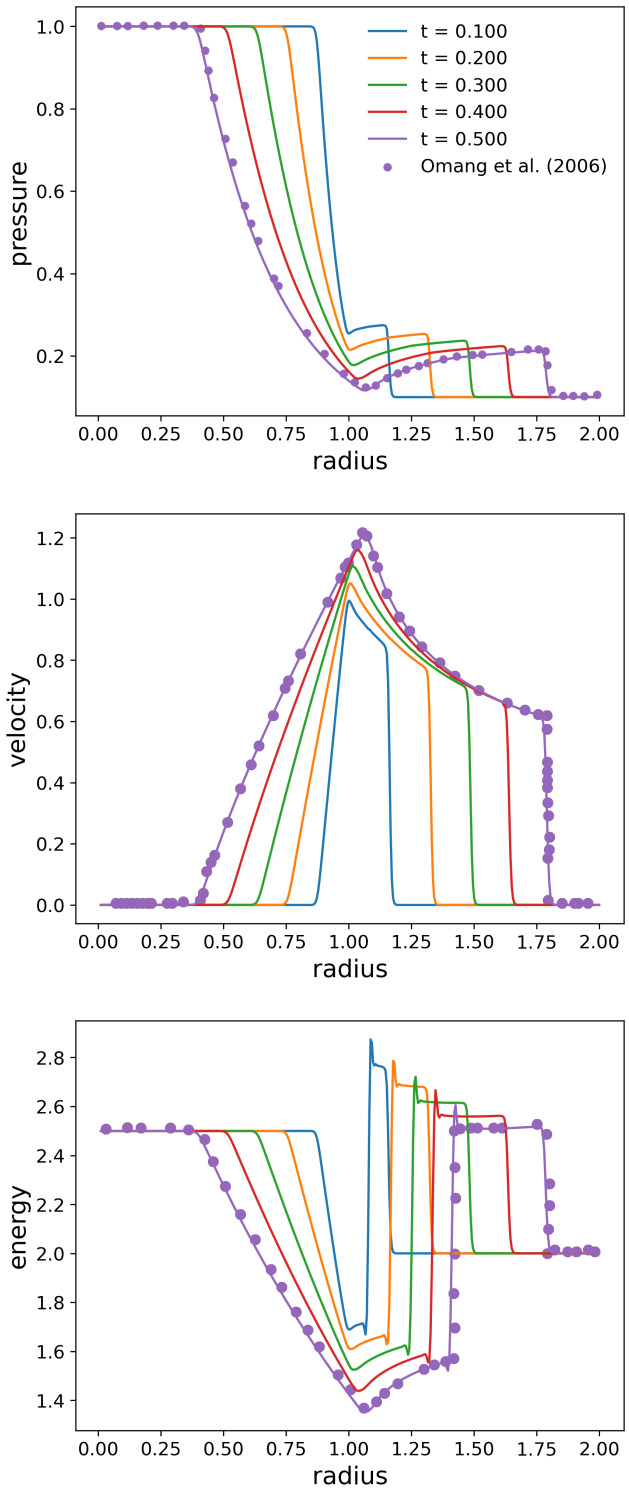

Fig. 5.1 Spherical Sod shock test showing pressure, velocity, and internal energy profiles at $t = 0.1 - 0.5$ s, with comparison in the final time-step against Riemann-solved reference solutions from Omang et al. (2006). The CIP scheme reproduces the expected shock, contact discontinuity, and rarefaction with good agreement; the most prominent deviation is a mild overshoot in the internal energy near the shock front.

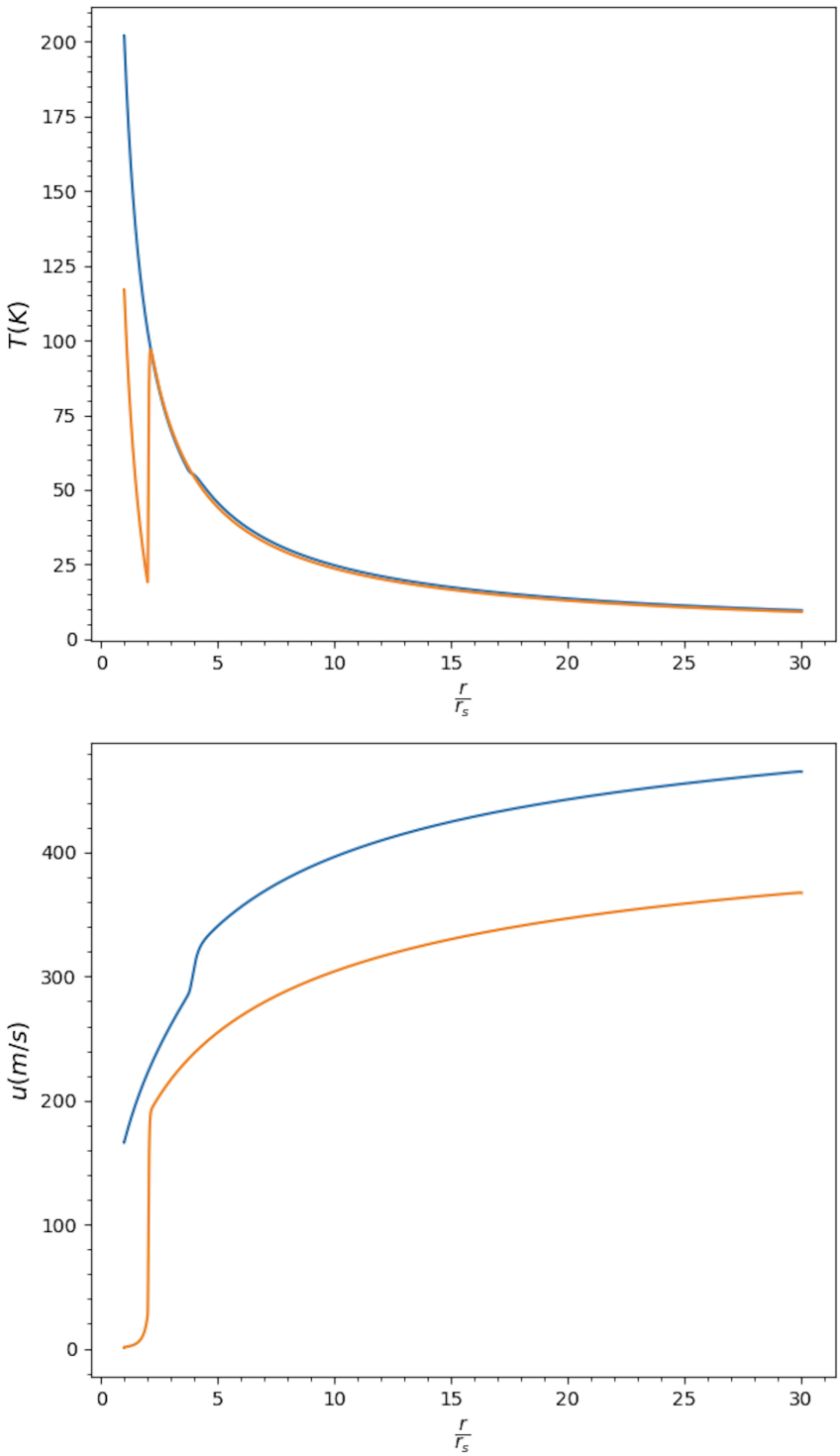

Fig. 5.2 Numerical experiments with the CIP scheme applied to a hypothetical primordial hydrogen atmosphere on the Moon. The blue curves show the initial adiabatic escape solution with a base temperature of ~200 K, while the orange curves show the adjusted solutions with a cooler base temperature of ~117 K sustained by EUV heating. The upper and lower panels show the temperature and velocity profiles.

attempts to obtain such solutions were numerically unstable. In contrast, stable transonic steady states were readily obtained for adiabatic thermal escape. We therefore attempted to reach an XUV-heated solution by progressively adjusting the flow from an initial adiabatic escape profile. Specifically, we considered a planet with a surface temperature high enough that adiabatic expansion alone drives escape, and then gradually lowered the base temperature while introducing XUV heating, asking how cool the planet could be while still sustaining an outflow. In practice, the code encountered a "soft floor" in temperature below which stable integration failed. This floor likely reflects numerical difficulties in resolving the extremely small velocities near the base of the flow, where dissipation dominates. It is also possible that a residual coding error remains— one not revealed by the Spherical Sod Shock test.

Figure 5.2 shows the result of this method, with an illustrative application to a primordial hydrogen atmosphere on the Moon. The computational domain is resolved with 4000 radial cells, ensuring that the Beer–Lambert peak of EUV heating is sharply captured. In both the temperature profile (top) and velocity profile (bottom), the blue curve represents the initial adiabatic escape solution, while the orange curve shows the adjusted solution with a lower base temperature sustained by XUV heating. In this heated case, the atmosphere remains cooler at the base yet still transitions to outflow, exhibiting a pronounced thermal inversion at the heating peak and a correspondingly steeper acceleration profile. These results demonstrate that the CIP scheme can stably capture the interplay between heating, inversion, and acceleration in a hydrodynamic outflow. Although intended as a proof of concept rather than a realistic model of lunar evolution, the parameter regime explored may be relevant for icy exomoons or small bodies subject to intense EUV irradiation, and it provides a foundation for applying CIP to the more complex problem of secondary-atmosphere escape considered in future work.

5.3 Solving Molecular- Kinetics with DSMC

5.3.1 Method

To understand the direct simulation Monte Carlo (DSMC) method and its aim, we start with the Liouville equation governing the evolution of the full N–particle distribution in the $6N$–dimensional phase space. By integrating the Liouville equation over the coordinates and momenta of $N-1$ particles we obtain the first BBGKY equation: an evolution equation for the one–particle distribution f_1 whose right-hand side involves the two–particle (pair) distribution f_2 (e.g. Cercignani, 1988). In the Boltzmann–Grad limit of a dilute gas, incoming hard–sphere pairs found at contact are uncorrelated, so their pre-collisional pair distribution factorizes, $f_2 \approx f_1(\mathbf{v}_1) f_1(\mathbf{v}_2)$ allowing the interaction term to become the Boltzmann collision integral.

We write the non-dimensional Boltzmann equation as

$$\mathrm{Sh}\,\frac{\partial \bar{f}}{\partial \bar{t}} + \bar{\mathbf{v}}\cdot\nabla_{\bar{\mathbf{r}}}\bar{f} + \frac{1}{\mathrm{Fr}}\bar{\mathbf{F}}\cdot\nabla_{\bar{\mathbf{v}}}\bar{f} = \frac{\sigma_{\mathrm{tot}} n_0 L_0}{4\pi}\int_{\mathbb{R}^3} \mathrm{d}^3\bar{v}_1 \int_{\mathbb{S}^2} \mathrm{d}\boldsymbol{\omega}\; \bar{g}\,(\bar{f}'\bar{f}_1' - \bar{f}\bar{f}_1), \tag{5.10}$$

where $\bar{g} = |\bar{\mathbf{v}} - \bar{\mathbf{v}}_1|$, σ_{tot} is the (dimensional) total hard–sphere cross section, n_0 and L_0 are the reference number density and length, and bars denote dimensionless variables, Sh is the Strouhal number and Fr the Froude number (Volkov, 2017). For equal-mass particles with initial velocities $(\mathbf{v}, \mathbf{v}_1)$, the set of possible $(\mathbf{v}', \mathbf{v}_1')$ is generated by reflecting the relative velocity $\mathbf{g} = \mathbf{v} - \mathbf{v}_1$ across planes orthogonal to any $\boldsymbol{\omega} \in \mathbb{S}^2$; thus the post states lie on a sphere of radius $|\mathbf{g}|$ in relative velocity space: $\bar{\mathbf{v}}' = \bar{\mathbf{v}} - (\bar{\mathbf{g}}\cdot\boldsymbol{\omega})\boldsymbol{\omega}$, and $\bar{\mathbf{v}}_1' = \bar{\mathbf{v}}_1 + (\bar{\mathbf{g}}\cdot\boldsymbol{\omega})\boldsymbol{\omega}$. The collision integral is defined over this Cartesian partner velocity space $\bar{\mathbf{v}}_1 \in \mathbb{R}^3$ and the unit sphere of scattering directions $\boldsymbol{\omega} \in \mathbb{S}^2$. Each binary collision conserves momentum and kinetic energy $\mathbf{v} + \mathbf{v}_1 = \mathbf{v}' + \mathbf{v}_1'$ and $\mathbf{v}|^2 + |\mathbf{v}_1|^2 = |\mathbf{v}'|^2 + |\mathbf{v}_1'|^2$.

We define the Knudsen number that is shared by the real and simulated flow

$$\mathrm{Kn} = \frac{1}{\sigma_r n_r L} = \frac{1}{\sigma_s n_s L}, \qquad W = \frac{n_r}{n_s} = \frac{\sigma_s}{\sigma_r}, \tag{5.11}$$

where subscripts r and s denote, respectively, real and simulated values. W is a weighting of real to simulated particles chosen so that the product σn is preserved. It is this Knudsen similarity that underpins DSMC (Volkov, 2017).

Classic DSMC time–splits the simulation into motion, boundary and collision substeps over each Δt. We emphasise that DSMC is not an attempt to sample and evolve a representation of the full N-body Liouville distribution; instead it targets the one-particle distribution $f(\mathbf{r}, \mathbf{v}, t)$ and its moments, under the Boltzmann molecular-chaos closure (Bird, 1994). In Bird's no–time–counter method, the collision substep has random pairing of particles in each cell to samples $\mathrm{d}^3 v_1$ weighted in expectation by $f f_1$ and uniform sampling of a scattering direction $\mathrm{d}\boldsymbol{\omega}$ (Bird, 1994). The kernel factor $\frac{d^2}{4}|\mathbf{g}|$ for hard spheres of diameter d appears through the expected number of pair trials that is proportional to $d^2 g_{\max} \Delta t$ and the acceptance probability $|\mathbf{g}|/g_{\max}$. Each accepted collision performs the deterministic velocity reflection that enforces momentum and energy conservation, thereby implementing the gain–loss term $f' f_1' - f f_1$ at the sample level. Ensemble averages of particle properties converge to the moments of the Boltzmann solution as particle number increases and discretisation parameters satisfy standard DSMC resolution constraints (Wagner, 1992).

In the time-counter method (Bird, 1994), a collision rate and an accumulating counter for every particle pair in a cell is tracked and collision triggered when that counter exceeds one, which scales quadratically with particle number. The No-Time-Counter method, replaces those per-pair counters with accept–reject sampling from a cellwise majorant $(\sigma_s g)_{\max}$, yielding the same unbiased collision statistics but with a computational cost that's roughly linear in particle number. Following Volkov (2017), we consider a cell of volume V, containing N simulation particles, with each simulation particle representing W physical

molecules. For two simulation particles i and j in the same cell the relative speed of the pair is $g_{ij} = |\mathbf{v}_i - \mathbf{v}_j|$. So, The probability of a random collision between molecules i and j during a sufficiently small time step:

$$P_{ij} = \frac{W \sigma_s g_{ij} \Delta t}{V},$$

so the associated pair collision frequency is $z_{ij} = P_{ij}/\Delta t = W \sigma_s g_{ij}/V$. Summing over all unordered pairs gives the actual (ideal) cell collision frequency

$$Z_{\text{cell}} = \sum_{i=1}^{N-1} \sum_{j=i+1}^{N} z_{ij} = \frac{W}{V} \sum_{i=1}^{N-1} \sum_{j=i+1}^{N} \sigma_s g_{ij}. \tag{5.12}$$

as can be found in Volkov (2017). The "majorant" upper bound $[\sigma_s g]_{\max} \geq \sigma_{T,ij} g_{ij}$ defines the majorant collision frequency

$$Z_{\max} = \frac{N(N-1)}{2} \frac{W}{V} [\sigma_s g]_{\max}.$$

A collision substep then proceeds by generating $Z_{\max}\Delta t$ candidate unordered pairs uniformly at random; each candidate (i, j) is accepted with probability $\frac{\sigma_s g_{ij}}{[\sigma_s g]_{\max}}$. Accepted pairs are processed with a freshly sampled isotropic $\boldsymbol{\omega}$; their velocities are updated via the reflection above. Rejection leaves particle velocities unchanged. The expected number of accepted collisions in the cell over Δt equals $Z_{\text{cell}}\Delta t$, yielding an unbiased Monte Carlo estimator of the continuous collision integral consistent with the molecular-chaos factorisation.

5.3.2 Application

The overarching aim of the Chatterjee et al. (2025) collaboration is to investigate the molecular-kinetics of atmospheric escape from terrestrial planets under strong XUV irradiation, following on from Johnson et al. (2013a). As a ready example, we present here a proof-of-concept

DSMC calculation that highlights the role of molecular transport in shaping an outflow. A toy model of Earth's thermosphere under extreme XUV fluxes at a base, or heating peak, temperature of 10,000 K and under the approximation of full photodissocation. The lower boundary is set to Earth's radius for simplicity $r_0 = 1\,R_\oplus$. The base number density is fixed at $n_0 = 10^{10}\,\mathrm{cm}^{-3}$ or $\mathrm{Kn} \sim 10^{-3}$.

The DSMC model employs a 1D spherically symmetric grid with adaptive resolution. The smallest cell width—located at the dense lower boundary where the local mean free path is shortest—is approximately $\Delta r \sim 2\,\mathrm{km}$. The maximum cell width is limited to $\Delta r \sim 10\,\mathrm{km}$ in regions where the local mean free path exceeds this value. This resolution ensures that each computational cell remains smaller than the local mean free path, satisfying standard DSMC resolution criteria. The timestep was chosen as $\Delta t \sim 10^{-2}\,\mathrm{s}$, smaller than the mean collision time at the base (estimated from the base density and temperature). Each simulation particle represents $W \sim 6 \times 10^{31}$ physical nitrogen atoms. Particle motion is integrated in the radial gravitational field of Earth using a fourth-order Runge–Kutta scheme. At each timestep, particles move according to their velocity, interact with boundaries, and undergo binary collisions sampled via the no-time-counter (NTC) method. Collisions conserve momentum and kinetic energy, and modify post-collision velocities accordingly. External energy sources (e.g. stellar heating) can be imposed but are not included in this particular example.

Within the polytropic framework (Chapter 2), a monatomic adiabatic outflow $\gamma = 5/3$ exhibits the unphysical feature of a decelerating outflow. Here, DSMC demonstrates that thermal conduction—which cannot be neglected when the Knudsen number is finite—removes this behaviour. Unlike hydrodynamic models, where conduction can be artificially switched off, DSMC inherently includes molecular transport processes. Consequently, both subsonic and transonic outflow solutions are altered once conduction is accounted for. In the simulation presented here, the bulk outflow velocity rises from zero at the base to $\sim$ 100 m/s, corresponding to non-negligible Mach numbers out to beyond the exobase. As

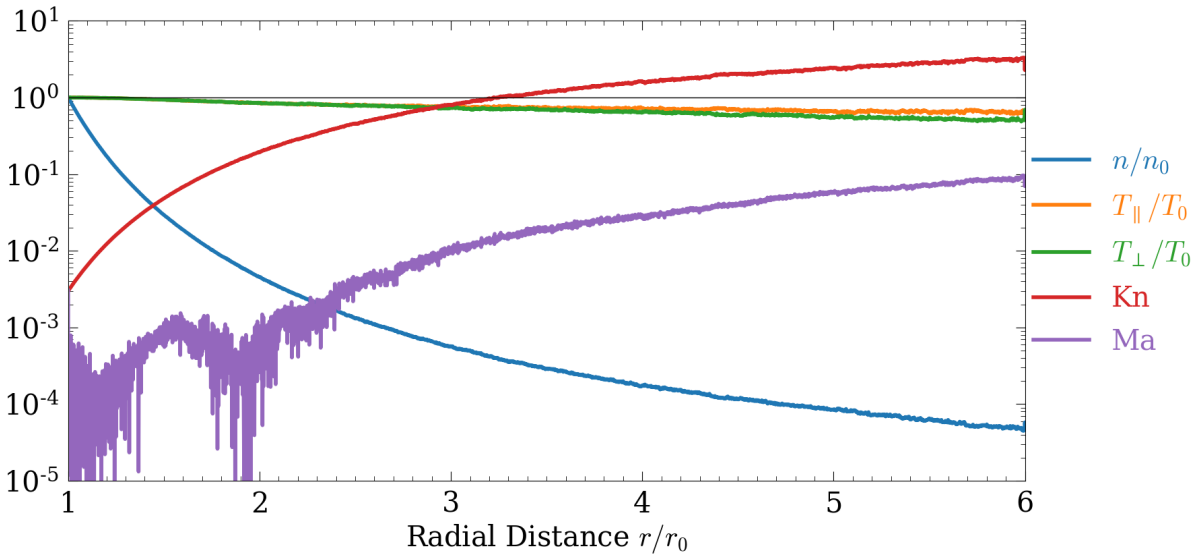

Fig. 5.3 Profiles of a thermally conductive outflow of monatomic nitrogen from an Earth-like planet with a hot base temperature of 10,000 K. The figure shows the radial dependence of number density, temperature, bulk velocity, and heat flux obtained from the DSMC simulation. The model employs a spherically symmetric grid with resolution tied to the local mean free path (2–10 km), and a timestep of 10^{-2} s. Each DSMC particle represents 6×10^{31} nitrogen atoms. The results demonstrate that thermal conduction, captured naturally by molecular transport in DSMC, resolves the unphysical deceleration of the adiabatic monatomic outflow (see Chapter 2), and leads instead to a physically consistent subsonic outflow with finite escape.

expected for a subsonic breeze, the escape flux remains weakly sensitive to the location of the upper boundary due to particle return fluxes from exosphere. In practical applications, the outer boundary could be set at the magnetopause distance or another physically motivated altitude.

5.4 Outlook

Following foundational studies such as García Muñoz (2007) on HD 209458b, which simulated heavy element escape beyond the Roche lobe, one-dimensional hydrocodes have flourished, routinely solving the Euler equations to model transonic outflows across an increasingly diverse population of exoplanets. Once certain numerical issues have been fixed, the development and implementation of the CIP method (Yabe and Aoki, 1991; Kuramoto et al., 2013) in Section 5.2 can contribute to this effort, with plans to make the code open source. However, the modelling frontier of escape is often shaped by the hand-off from continuum to rarefied flow ($\mathrm{Kn} \gtrsim 0.1$) and non-equilibrium processes. Molecular-kinetic techniques, long the workhorse of Solar-System aeronomy, naturally bridge this gap, but is rarely implemented in studies of hydrodynamic escape or exoplanet atmospheres. Johnson et al. (2013a,b) combined an analytic treatment with DSMC modelling to derive a critical heating rate for triggering transonic flow, working with the ansatz that the scaling of this transition extends smoothly from Pluto- to Earth-sized bodies, which many not prove true. As such, we provide a pedagogical introduction to how DSMC effectively solves the Boltzmann equation in Section 5.3. To illustrate the method, we present a preliminary simulation of thermally conductive outflow of a monatomic nitrogen thermosphere on an Earth-like planet with a hot base temperature of 10,000 K.

Characterising the transition from Jeans (particle-by-particle) escape to subsonic and ultimately transonic bulk outflow remains an open problem in escape theory. Chapter 4 illustrates how onset of rapid escape ($\gtrsim 1$ bar/Myr) as ionising irradiation increases is a key

parameter defining the phase boundary between airless and airy rocky worlds—the "Cosmic Shoreline" (Zahnle and Catling, 2017; Ji et al., 2025). We hope to build on the framework of Johnson et al. (2013a) and the work reported here to characterise the onset of rapid escape of secondary atmospheres across the size range of rocky planets, progressively implementing the physical processes explored in this thesis.

6

Conclusions

The principal outcome of this thesis is a predictive, physically motivated map of atmospheric loss for rocky planets subjected to intense XUV irradiation. By combining analytic tractability with an up-to-date range of physical processes, the framework fills a gap between detailed numerical simulations and oversimplified energy–limited models, offering both immediate interpretive power for current surveys and a foundation for future, more complete simulations. Across four chapters of original results, the work advances both analytic and numerical modelling.

Context: Research on hydrodynamic escape from secondary atmospheres remains at an early stage: available studies are few, sometimes conflicting, and unevenly regarded within the broader planetary field. Pioneering work from Tian et al. (2008) suggested that

Earth-like atmospheres should be unstable under a modest enhancement of present-day Earth levels of ionising irradiation, while Johnstone et al. (2019) found transonic outflow could be driven in the raised fluxes of the active young Sun. In contrast, groundbreaking simulations by Nakayama et al. (2022) showed that efficient cooling through metastable N, C, and O states could maintain hydrostatic stability under XUV fluxes nearly three orders of magnitude higher than Tian et al. (2008). However, their study was restricted to Earth-sized planets and a single composition, leaving its broad applicability to the exoplanet population uncertain. These results have been taken to imply atmospheric retention on sub-Earths, independent of the intensity of ionising irradiation (Krissansen-Totton et al., 2024), or, conversely, set aside entirely due to modelling difficulties, with escape then inferred to occur readily (Van Looveren et al., 2024; Looveren et al., 2025). In parallel, it remains common in parts of the field to assume that secondary atmospheres never undergo direct hydrodynamic escape, regardless of the debate arising from simulations (e.g. Teixeira et al., 2023; Kreidberg and Stevenson, 2025).

Chapter 1: The opening chapter frames atmospheric loss as a central challenge in the study of planetary habitability and exoplanet characterisation. Early results from the *James Webb Space Telescope* indicate that many rocky planets orbiting M dwarfs may be airless. This motivates the development of a theoretical framework to predict which rocky worlds can retain high–molecular–weight atmospheres, such as those dominated by nitrogen or carbon dioxide. The chapter outlines the habitable zone concept, summarises the physics of upper–atmosphere escape, reviews methods for detecting exoplanet atmospheres, and introduces the “cosmic shoreline” heuristic that distinguishes worlds with substantial atmospheres from those without.

Chapters 2 & 3: A polytropic equation of state has long been used to capture the physics of gas envelopes, from stellar structure and the solar wind (Chandrasekhar, 1931; Holzer and Axford, 1970; Lamers and Cassinelli, 1999) to hydrogen escape from hot Jupiters (Owen

and Jackson, 2012). We extend this approach to rocky planet atmospheres, exploring the landscape of high–molecular–weight escape (Fig. 3.6) by varying the power–law index γ, which sets the steepness of atmospheric inversion under idealised XUV heating. For a given gravitational binding described by the escape parameter λ_0, we derive analytic solutions for atmospheric profiles, including approximations for sonic–point properties and thermomechanical efficiency, which remain relatively insensitive to a physically motivated range of lower boundary conditions. As a validation, we compared our Young–Sun Earth transonic escape model with the hydrocode simulations of Johnstone et al. (2019).

We diagnosed forbidden-line cooling from polytropic profiles with a three-level atom model, finding it minor for Young-Sun Mars transonic escape and significant for Young-Sun Earth. We develop an explanation for the temperature behaviour in varying XUV fluxes of Nakayama et al. (2022) based on the feedback from electron densities on the forbidden line cooling in the photoionization front. We generalize the notion, calling it the collisional-radiative thermostat, and explore its control on escape under a range of conditions.

For strongly ionized atmospheres, the ambipolar electric field halves the mean molecular weight compared to a predominantly neutral flow, reducing the temperatures required for hydrostatic instability and transonic outflow by half. We suggest that incomplete accounting of these ion-electron interactions explains how Nakayama et al. (2022) found persistent stability even up to 1000× Modern Earth XUV fluxes, in contrast with our study, which finds transonic outflow for half that flux or less. We propose that the shift to ion-acoustic sound speed, characterized by the *plasma* escape temperature, allows the transonic outflow of a secondary atmosphere from a super-Earth even under the action of the collisional-radiative thermostat (see Figure 3.5).

We conclude that the escape rate of secondary atmospheres from Mars-to-Earth-sized bodies can be roughly calculated with an energy limit above a threshold XUV flux given by the Knudsen-onset in collisionality at the sonic point. For super-Earths, escape shifts

towards a transonic global ion outflow with the thermal structure determined by the balance of photoionization heating and forbidden line cooling. The transonic onset and escape rate can be roughly interpolated from the collisional-radiative thermostat presented in Figure 3.5. These results are consistent with the vulnerability of TRAPPIST-1 b and c to easily lose a thick atmosphere and the ability of LHS 1140 b to hold on to a possibly N_2-dominated secondary atmosphere.

Chapter 4: Building on the classic "cosmic shoreline" framework (Zahnle and Catling, 2017), this chapter applied the escape thresholds and scaling laws developed in Chapters 2 and 3 to evolutionary case studies and population-level analyses. We examined the potential for atmospheric survival on GJ 357 b (Taylor et al., 2025), highlighting how its unusually inactive host star may allow volcanic revival of a secondary atmosphere, and analysed the L 98-59 system (Nicholls et al., 2025a), where high XUV fluences challenge the plausibility of retention of a secondary atmosphere on the sub-Earth planet b despite suggestion of a tentative detection (Bello-Arufe et al., 2025b). We then redrew the cosmic shoreline based on Monte Carlo population modelling from Ji et al. (2025), showing how volatile inventory, stellar evolution, and nonlinear escape physics combine to reshape the boundary between airless and atmosphere-bearing rocky worlds. Finally, we explored how intrinsic planetary magnetic fields could act as a powerful suppressor of rapid escape, potentially shifting the shoreline further (Meier et al., 2025). Together, these results provide both detailed case studies and a population-wide update to the fate of rocky exoplanet atmospheres.

Chapter 5: Until recently there were no open-source time-dependent hydrodynamic escape solvers, and today there are only a few (Caldiroli, 2021; Schulik and Booth, 2023), none of which have been applied to the escape of Earth-like or Venus-like atmospheres. It was therefore deemed useful to attempt the development of a new code based on a semi-Lagrangian scheme that had proven effective in modelling hydrogen escape from Early Earth. We present and validate an implementation of the Constrained Interpolation

Profile (CIP) algorithm against against a Spherical Sod Shock program and a thermal hydrodynamic escape simulation, but stability issues were encountered. We then introduce molecular–kinetic treatments with the direct simulation Monte Carlo (DSMC) method, including a proof-of-concept simulation of subsonic escape of an artificially hot Earth-like thermosphere, bridging collisional and collisionless regimes. Given uncertainties over the broad applicability of the results of Johnson et al. (2013a) on the energy-limit and the onset of transonic escape, in particular for tightly bound atmospheres with steep thermospheric inversions, there is clear value in developing DSMC approaches.

Future Work: The successes and limitations of this thesis present several avenues for future research. The analytic methods developed using the polytropic framework and the collisional–radiative thermostat could be applied to atmospheres rich in CO_2, SO_2, and O_2. The heating and cooling mechanisms assessed here could also be expanded to include strong atomic lines and molecular coolants. Ultimately, however, comprehensive photochemical simulations of Exo-Earths and Exo-Venuses around M dwarfs are required, and first steps in this direction are already underway (Blumenthal et al., 2025). Recently, Hanson et al. (2025) simulated global ionospheres at intermediate XUV fluxes, though without including atomic line cooling. Such a 3D model could be embedded in a planetary magnetic field and further developed to create robust representations of the escape of secondary atmospheres from rocky exoplanets. Even then, however, the results are likely to be highly sensitive to energetic and dynamical processes that are often neglected, such as Joule heating (Cohen et al., 2024), as well as to processes that may not yet be well understood, such as ionospheric mixing in regimes of extreme ionization.

Know thy planet, know thy star: for progress in the physics of escape to truly come to fruition, a better understanding of the XUV luminosity evolution of low-mass stars is essential. A first step in this direction would be to combine `MORS` with the latest M-dwarf catalogues (e.g., Engle, 2023). At present, `MORS` appears to struggle with inactive stars,

as seen for GJ 357 b. Ultimately, however, progress will require an EUV space telescope, such as *ESCAPE* (France et al., 2022); otherwise, we remain limited by order-of-magnitude uncertainties in this wavelength range.

Progress on both the planetary and stellar fronts, combined with the rapidly growing sample of rocky exoplanets characterised by *JWST*, will enable important inferences. In Chapter 4, we compared volatile-poor and volatile-rich shorelines, laying the groundwork for inferring the primordial volatile inventories of the population of rocky planets from their present-day characteristics. This effort will be aided by the precise masses and radii of rocky planets around Sun-like stars that ESA's *PLATO* mission is expected to deliver following its planned 2026 launch (Rauer et al., 2025). Further development of the molecular–kinetic and hydrocode approaches introduced in Chapter 5 could be used to address fundamental questions about the transition from Jeans escape, through subsonic bulk-kinetic outflow, to transonic escape; unsteady dynamics such as the response to stellar flares; and the possibility of bistability in the dynamical states of upper atmospheres.

Outlook: *The Kepler Space Telescope* revealed that the population of small exoplanets is profoundly shaped by atmospheric photoevaporation, and that rocky planets are ubiquitous. The first three observing cycles of the *James Webb Space Telescope* have proven technological capability to constrain the presence of Earth-like and Venus-like atmospheres around rocky planets orbiting low-mass stars, and have hinted that the signature of photoevaporation extends from primary to secondary atmospheres. Building on this foundation, the forthcoming General Observing Programs and the Rocky Worlds DDT observations promise a step-change in our understanding of rocky exoplanets over the next few years. The depth of that advance, however, will depend critically on the capabilities of state-of-the-art models of hydrodynamic atmospheric escape and the predictive frameworks they enable— precisely the focus of this thesis. This revisiting of the hydrodynamic escape of planetary atmospheres

in the age of *JWST* is but a first step into the rich and still largely uncharted domain of rocky exoplanet aeronomy and escape.

References

Adams, F. C., Bodenheimer, P., and Laughlin, G. (2005). M dwarfs: planet formation and long term evolution. *Astronomische Nachrichten*, 326(10):913–919.

Adams, F. C. and Laughlin, G. (1997). A dying universe: the long-term fate and evolutionof astrophysical objects. *Reviews of Modern Physics*, 69(2):337–372.

Agol, E., Dorn, C., Grimm, S. L., Turbet, M., Ducrot, E., Delrez, L., Gillon, M., Demory, B.-O., Burdanov, A., Barkaoui, K., Benkhaldoun, Z., Bolmont, E., Burgasser, A., Carey, S., De Wit, J., Fabrycky, D., Foreman-Mackey, D., Haldemann, J., Hernandez, D. M., Ingalls, J., Jehin, E., Langford, Z., Leconte, J., Lederer, S. M., Luger, R., Malhotra, R., Meadows, V. S., Morris, B. M., Pozuelos, F. J., Queloz, D., Raymond, S. N., Selsis, F., Sestovic, M., Triaud, A. H. M. J., and Grootel, V. V. (2021). Refining the Transit-timing and Photometric Analysis of TRAPPIST-1: Masses, Radii, Densities, Dynamics, and Ephemerides. *The Planetary Science Journal*, 2(1):1.

Alderson, L., Moran, S. E., Wallack, N. L., Batalha, N. E., Wogan, N. F., Dattilo, A., Wakeford, H. R., Redai, J. A., Alam, M. K., Aguichine, A., Batalha, N. M., Gagnebin, A., Gao, P., Kirk, J., López-Morales, M., Meech, A., Teske, J., and Wolfgang, A. (2025). JWST COMPASS: NIRSpec/G395H Transmission Observations of the Super-Earth TOI-776 b. AJ, 169(3):142.

August, P. C., Buchhave, L. A., Diamond-Lowe, H., Mendonça, J. M., Gressier, A., Rathcke, A. D., Allen, N. H., Fortune, M., Jones, K. D., Meier-Valdés, E. A., Demory, B.-O., Espinoza, N., Fisher, C. E., Gibson, N. P., Heng, K., Hoeijmakers, J., Hooton, M. J., Kitzmann, D., and Prinoth, B. (2024). Hot Rocks Survey I : A shallow eclipse for LHS 1478 b. *arXiv e-prints*, page arXiv:2410.11048.

August, P. C., Buchhave, L. A., Rathcke, A., Allen, N., Demory, B.-O., Diamond-Lowe, H., Espinoza, N., Fisher, C., Fortune, M., Gibson, N., Gressier, A., Heng, K., Hoeijmakers, J., Hooton, M., Jones, K., Kitzmann, D., Krissansen-Totton, J., Meier Valdes, E. A., Mendonca, J. M., Prinoth, B., Ribas, I., and Wordsworth, R. (2025). Confirming a Tentative Terrestrial Atmosphere Detection on LHS 1478 b with JWST/MIRI. JWST Proposal. Cycle 4, ID. #7675.

Badnell, N. R. (2006). Radiative recombination data for modeling dynamic finite-density plasmas. ApJS, 167(2):334.

Banerjee, A., Barstow, J. K., Gressier, A., Espinoza, N., Sing, D. K., Allen, N. H., Birkmann, S. M., Challener, R. C., Crouzet, N., Haswell, C. A., Lewis, N. K., Lewis, S. R., and Yang, J. (2024). Atmospheric Retrievals Suggest the Presence of a Secondary Atmosphere and Possible Sulfur Species on L98-59 d from JWST Nirspec G395H Transmission Spectroscopy. *The Astrophysical Journal Letters*, 975(1):L11. Publisher: IOP ADS Bibcode: 2024ApJ...975L..11B.

Baraffe, I., Homeier, D., Allard, F., and Chabrier, G. (2015). New evolutionary models for pre-main sequence and main sequence low-mass stars down to the hydrogen-burning limit. *Astronomy & Astrophysics*, 577:A42.

Baranne, A., Queloz, D., Mayor, M., Adrianzyk, G., Knispel, G., Kohler, D., Lacroix, D., Meunier, J. P., Rimbaud, G., and Vin, A. (1996). ELODIE: A spectrograph for accurate radial velocity measurements. A&AS, 119:373–390.

Bates, D. R. (1951). The temperature of the upper atmosphere. *Proceedings of the Physical Society. Section B*, 64(9):805.

Bauer, A. and Carter, P. (2021). Existence of transonic solutions in the stellar wind problem with viscosity and heat conduction. *SIAM Journal on Applied Dynamical Systems*, 20:262–298.

Bauer, S. and Lammer, H. (2004). *Planetary Aeronomy, Atmosphere Environments in Planetary Systems*. Springer.

Behr, P. R., France, K., Brown, A., Duvvuri, G., Bean, J. L., Berta-Thompson, Z., Froning, C., Miguel, Y., Pineda, J. S., Wilson, D. J., and Youngblood, A. (2023). The MUSCLES Extension for Atmospheric Transmission Spectroscopy: UV and X-Ray Host-star Observations for JWST ERS & GTO Targets. AJ, 166(1):35.

Bello-Arufe, A., Damiano, M., Bennett, K. A., Hu, R., Welbanks, L., MacDonald, R. J., Seligman, D. Z., Sing, D. K., Tokadjian, A., Oza, A., and Yang, J. (2025a). Evidence for a volcanic atmosphere on the sub-Earth L98-59b. Technical report, arXiv. arXiv:2501.18680 [astro-ph].

Bello-Arufe, A., Damiano, M., Bennett, K. A., Hu, R., Welbanks, L., MacDonald, R. J., Seligman, D. Z., Sing, D. K., Tokadjian, A., Oza, A., and Yang, J. (2025b). Evidence for a volcanic atmosphere on the sub-earth l98-59b.

Benneke, B., Roy, P.-A., Coulombe, L.-P., Radica, M., Piaulet, C., Ahrer, E.-M., Pierrehumbert, R., Krissansen-Totton, J., Schlichting, H. E., Hu, R., Yang, J., Christie, D., Thorngren, D., Young, E. D., Pelletier, S., Knutson, H. A., Miguel, Y., Evans-Soma, T. M., Dorn, C., Gagnebin, A., Fortney, J. J., Komacek, T., MacDonald, R., Raul, E., Cloutier, R., Acuna, L., Lafrenière, D., Cadieux, C., Doyon, R., Welbanks, L., and Allart, R. (2024). JWST Reveals CH_4, CO_2, and H_2O in a Metal-rich Miscible Atmosphere on a Two-Earth-Radius Exoplanet. *arXiv e-prints*, page arXiv:2403.03325.

Berger, T. A., Huber, D., Gaidos, E., Van Saders, J. L., and Weiss, L. M. (2020). The Gaia–Kepler Stellar Properties Catalog. II. Planet Radius Demographics as a Function of Stellar Mass and Age. *The Astronomical Journal*, 160(3):108.

Bird, G. (1994). *Molecular Gas Dynamics and the Direct Simulation of Gas Flows*. Clarendon Press.

Blumenthal, S., Chatterjee, R., Nicholls, H., Amard, L., Tsai, S.-M., Komacek, T., and Pierrehumbert, R. (2025). Photochemistry versus escape in the TRAPPIST-1 planets. In *EPSC–DPS Joint Meeting 2025*, Helsinki, Finland.

Bryson, S., Kunimoto, M., Kopparapu, R. K., Coughlin, J. L., Borucki, W. J., Koch, D., Aguirre, V. S., Allen, C., Barentsen, G., Batalha, N. M., Berger, T., Boss, A., Buchhave, L. A., Burke, C. J., Caldwell, D. A., Campbell, J. R., Catanzarite, J., Chandrasekaran, H., Chaplin, W. J., Christiansen, J. L., Christensen-Dalsgaard, J., Ciardi, D. R., Clarke, B. D., Cochran, W. D., Dotson, J. L., Doyle, L. R., Duarte, E. S., Dunham, E. W., Dupree, A. K., Endl, M., Fanson, J. L., Ford, E. B., Fujieh, M., Gautier, III, T. N., Geary, J. C., Gilliland, R. L., Girouard, F. R., Gould, A., Haas, M. R., Henze, C. E., Holman, M. J., Howard, A. W., Howell, S. B., Huber, D., Hunter, R. C., Jenkins, J. M., Kjeldsen, H., Kolodziejczak, J., Larson, K., Latham, D. W., Li, J., Mathur, S., Meibom, S., Middour, C., Morris, R. L., Morton, T. D., Mullally, F., Mullally, S. E., Pletcher, D., Prsa, A., Quinn, S. N., Quintana, E. V., Ragozzine, D., Ramirez, S. V., Sanderfer, D. T., Sasselov, D., Seader, S. E., Shabram, M., Shporer, A., Smith, J. C., Steffen, J. H., Still, M., Torres, G., Troeltzsch, J., Twicken, J. D., Uddin, A. K., Van Cleve, J. E., Voss, J., Weiss, L. M., Welsh, W. F., Wohler, B., and Zamudio, K. A. (2021). The Occurrence of Rocky Habitable-zone Planets around Solar-like Stars from Kepler Data. AJ, 161(1):36.

Cadieux, C., Doyon, R., MacDonald, R. J., Turbet, M., Artigau, , Lim, O., Radica, M., Fauchez, T. J., Salhi, S., Dang, L., Albert, L., Coulombe, L.-P., Cowan, N. B., Lafrenière, D., L'Heureux, A., Piaulet-Ghorayeb, C., Benneke, B., Cloutier, R., Charnay, B., Cook, N. J., Fournier-Tondreau, M., Plotnykov, M., and Valencia, D. (2024). Transmission Spectroscopy of the Habitable Zone Exoplanet LHS 1140 b with JWST/NIRISS. *The Astrophysical Journal Letters*, 970(1):L2.

Caldiroli, A. (2021). ATES: ATmospheric EScape. Astrophysics Source Code Library, record ascl:2106.015.

Canto, J. and Raga, A. C. (1991). Mixing Layers in Stellar Outflows. *The Astrophysical Journal*, 372:646. ADS Bibcode: 1991ApJ...372..646C.

Carolan, S., Vidotto, A. A., Hazra, G., D'Angelo, C. V., and Kubyshkina, D. (2021). The effects of magnetic fields on observational signatures of atmospheric escape in exoplanets: Double tail structures.

Carteret, Y., Bourrier, V., and Dethier, W. (2024). The Rossiter-McLaughlin effect and exoplanet transits: A delicate association at medium and low spectral resolution. A&A, 683:A63.

Casasayas-Barris, N., Pallé, E., Yan, F., Chen, G., Luque, R., Stangret, M., Nagel, E., Zechmeister, M., Oshagh, M., Sanz-Forcada, J., Nortmann, L., Alonso-Floriano, F. J., Amado, P. J., Caballero, J. A., Czesla, S., Khalafinejad, S., López-Puertas, M., López-Santiago, J., Molaverdikhani, K., Montes, D., Quirrenbach, A., Reiners, A., Ribas, I., Sánchez-López, A., and Zapatero Osorio, M. R. (2020). Is there Na I in the atmosphere of HD 209458b?. Effect of the centre-to-limb variation and Rossiter-McLaughlin effect in transmission spectroscopy studies. A&A, 635:A206.

Catling, D. and Kasting, J. (2017). *Atmospheric evolution on inhabited and lifeless worlds*. CUP.

Cercignani, C. (1988). *The Boltzmann Equation and Its Applications*, volume 67 of *Applied Mathematical Sciences*. Springer New York, 1 edition.

Chandrasekhar, S. (1931). The Maximum Mass of Ideal White Dwarfs. ApJ, 74:81.

Charbonneau, D., Allen, L. E., Megeath, S. T., Torres, G., Alonso, R., Brown, T. M., Gilliland, R. L., Latham, D. W., Mandushev, G., O'Donovan, F. T., and Sozzetti, A. (2005). Detection of Thermal Emission from an Extrasolar Planet. ApJ, 626(1):523–529.

Charbonneau, D., Brown, T. M., Latham, D. W., and Mayor, M. (2000). Detection of Planetary Transits Across a Sun-like Star. *The Astrophysical Journal*, 529(1):L45–L48.

Charbonneau, D., Brown, T. M., Noyes, R. W., and Gilliland, R. L. (2002). Detection of an Extrasolar Planet Atmosphere. *The Astrophysical Journal*, 568(1):377–384.

Chatterjee, R., Carberry Mogan, S., and Johnson, R. (2025). Refining exoplanet escape predictions with molecular-kinetic simulations. In *EPSC-DPS Joint Meeting 2025*, pages EPSC–DPS2025–1756, Helsinki, Finland. 7–12 September 2025.

Chatterjee, R. D. and Pierrehumbert, R. T. (2024). Novel Physics of Escaping Secondary Atmospheres May Shape the Cosmic Shoreline. *arXiv e-prints*, page arXiv:2412.05188.

Chen, F. F. (2016). *Introduction to Plasma Physics and Controlled Fusion*. Springer International Publishing.

Cohen, O., Glocer, A., Garraffo, C., Alvarado-Gómez, J. D., Drake, J. J., Monsch, K., and Puigdomenech, F. F. (2024). Heating of the atmospheres of short-orbit exoplanets by their rapid orbital motion through an extreme space environment. *ApJ*, 962(2):157.

Collinson, G. A., Glocer, A., Pfaff, R., Barjatya, A., Conway, R., Breneman, A., Clemmons, J., Eparvier, F., Michell, R., Mitchell, D., Imber, S., Akbari, H., Davis, L., Kavanagh, A., Robertson, E., Swanson, D., Xu, S., Miller, J., Cameron, T., Chornay, D., Uribe, P., Nguyen, L., Clayton, R., Graves, N., Debchoudhury, S., Valentine, H., Ghalib, A., Zesta, E., Zarro, D., Xu, S., Wroblewski, N., Wilson, T., West, B., West, L., Waters, F., Wallace, M., Valentine, H., Uribe, P., Tucker, C., Tiede, S., Terwiliger, R., Taylor, W., Swift, R., Swanson, D., Sveen, J., Sutton, V., Søreng, J., Snyder, T., Simonsen, R., Sherman, T., Serabian, B., Samara, M., Russell, T., Rosnack, T., Rose, B., Rosanova, G., Rodriguez, S., Robertson, E., Ribbens, P., Rawlings, Z., Raley, D., Puopolo, D., Polidan, J., Pittman, E., Pirner, C., Pfaff, R., Paschalidis, N., Page, D., Osbakk, K., Ogundere, W., Nguyen, L., Nelson, C., Mueseler, A., Morris, N., Moffett, M., Mitchell, D., Michell, R., McFaden, T., Martin, S., Marshall, R., Marsh, G., Maimone, M., Lotz, P., Lien, R., Lankford, T., Laman, R., Knight, D., King, M., Kavanagh, A., Jones, T., Jones, G., Johnson, H., Johnson, E., Jillard, R., Jester, T., Jensen, K., Imber, S., Herseth, K., Henderson, D., Henderson, J., Helgesen, E., Haugh, H., Harper, T., Harlan, G., Hanssen, P., Haggstrom, I., Graves, N., Grabusky, C., Glocer, A., Ghalib, A., Gass, T., Frost, C., Francheshini, M., Farrell, J., Fahringer, R., Ethridge, R., Eparvier, F., Ellis, S., Eilertsen, L., Doughty, J., Disbrow, M., Detwiler, D., Demaine, P., Debchoudhury, S., Davis, L., Conway, R., Conser, L., Collinson, G., Clemmons, J., Clayton, R., Chornay, D., Cathell, P., Campbell, M., Cameron, T., Bridges, G., Breneman, A., Bradshaw, M., Bowlen, E., Bowker, D., Bowden, D., Borgen, H., Bonsteel, B., Bolton, A., Blix, K., Bissett, S., Binder, M., Barrie, A., Barjatya, A., Bancroft, C., Bain, G., Bahr, H., Baddeley, L., Albano, R., Akbari, H., and Adkins, S. (2024). Earth's ambipolar electrostatic field and its role in ion escape to space. *Nature*, 632:1021–1025.

Connors, N. J., Monaghan, C., Benneke, B., and Dang, L. (2025). Uniform Reanalysis of JWST MIRI 15μm Exoplanet Eclipse Observations using Frame-Normalized Principal Component Analysis. *arXiv e-prints*, page arXiv:2507.02052.

Cranmer, S. R. (2004). New views of the solar wind with the lambert w function. *American Journal of Physics*, 72:1397–1403.

Crossfield, I. J. M., Malik, M., Hill, M. L., Kane, S. R., Foley, B., Polanski, A. S., Coria, D., Brande, J., Zhang, Y., Wienke, K., Kreidberg, L., Cowan, N. B., Dragomir, D., Gorjian, V., Mikal-Evans, T., Benneke, B., Christiansen, J. L., Deming, D., and Morales, F. Y. (2022). GJ 1252b: A Hot Terrestrial Super-Earth with No Atmosphere. *The Astrophysical Journal Letters*, 937(1):L17.

de Wit, J., Wakeford, H. R., Gillon, M., Lewis, N. K., Valenti, J. A., Demory, B.-O., Burgasser, A. J., Burdanov, A., Delrez, L., Jehin, E., Lederer, S. M., Queloz, D., Triaud, A. H. M. J., and Van Grootel, V. (2016). A combined transmission spectrum of the Earth-sized exoplanets TRAPPIST-1 b and c. *Nature*, 537(7618):69–72. Publisher: Nature Publishing Group.

de Wit, J., Wakeford, H. R., Lewis, N. K., Delrez, L., Gillon, M., Selsis, F., Leconte, J., Demory, B.-O., Bolmont, E., Bourrier, V., Burgasser, A. J., Grimm, S., Jehin, E., Lederer, S. M., Owen, J. E., Stamenković, V., and Triaud, A. H. M. J. (2018). Atmospheric reconnaissance of the habitable-zone Earth-sized planets orbiting TRAPPIST-1. *Nature Astronomy*, 2(3):214–219. Publisher: Nature Publishing Group.

Demangeon, O. D. S., Zapatero Osorio, M. R., Alibert, Y., Barros, S. C. C., Adibekyan, V., Tabernero, H. M., Antoniadis-Karnavas, A., Camacho, J. D., Suárez Mascareño, A., Oshagh, M., Micela, G., Sousa, S. G., Lovis, C., Pepe, F. A., Rebolo, R., Cristiani, S., Santos, N. C., Allart, R., Allende Prieto, C., Bossini, D., Bouchy, F., Cabral, A., Damasso, M., Di Marcantonio, P., D'Odorico, V., Ehrenreich, D., Faria, J., Figueira, P., Génova Santos, R., Haldemann, J., Hara, N., González Hernández, J. I., Lavie, B., Lillo-Box, J., Lo Curto, G., Martins, C. J. A. P., Mégevand, D., Mehner, A., Molaro, P., Nunes, N. J., Pallé, E., Pasquini, L., Poretti, E., Sozzetti, A., and Udry, S. (2021). Warm terrestrial planet with half the mass of Venus transiting a nearby star. A&A, 653:A41.

Deming, D., Seager, S., Richardson, L. J., and Harrington, J. (2005). Infrared radiation from an extrasolar planet. *Nature*, 434(7034):740–743.

Demory, B.-O., Gillon, M., De Wit, J., Madhusudhan, N., Bolmont, E., Heng, K., Kataria, T., Lewis, N., Hu, R., Krick, J., et al. (2016). A map of the large day–night temperature gradient of a super-earth exoplanet. *Nature*, 532(7598):207–209.

Diamond-Lowe, H., King, G. W., Youngblood, A., Brown, A., Howard, W. S., Winters, J. G., Wilson, D. J., France, K., Mendonça, J. M., Buchhave, L. A., Corrales, L., Kreidberg, L., Medina, A. A., Bean, J. L., Berta-Thompson, Z. K., Evans-Soma, T. M., Froning, C., Duvvuri, G. M., Kempton, E. M.-R., Miguel, Y., Pineda, J. S., and Schneider, C. (2024). High-energy spectra of ltt 1445a and gj 486 reveal flares and activity. *AA*, 689:A48.

Dole, S. H. (1964). *Habitable Planets for Man*. Blaisdell Publishing Company, New York, NY.

Dong, C., Jin, M., Lingam, M., Airapetian, V. S., Ma, Y., and van der Holst, B. (2018). Atmospheric escape from the TRAPPIST-1 planets and implications for habitability. *Proceedings of the National Academy of Sciences*, 115(2):260–265.

Dorn, C. and Lichtenberg, T. (2021). Hidden Water in Magma Ocean Exoplanets. ApJ, 922(1):L4.

Dorn, C., Noack, L., and Rozel, A. (2018). Outgassing on stagnant-lid super-Earths. *Astronomy & Astrophysics*, 614:A18.

Dressing, C. D. and Charbonneau, D. (2015). THE OCCURRENCE OF POTENTIALLY HABITABLE PLANETS ORBITING M DWARFS ESTIMATED FROM THE FULL *KEPLER* DATASET AND AN EMPIRICAL MEASUREMENT OF THE DETECTION SENSITIVITY. *The Astrophysical Journal*, 807(1):45. Publisher: IOP ADS Bibcode: 2015ApJ...807...45D.

Drew, J. E. (1985). A radiative ionization and thermal equilibrium model for the wind from P Cygni. *MNRAS*, 217(4):867–893.

Ducrot, E., Lagage, P.-O., Min, M., Gillon, M., Bell, T. J., Tremblin, P., Greene, T., Dyrek, A., Bouwman, J., Waters, R., Güdel, M., Henning, T., Vandenbussche, B., Absil, O., Barrado, D., Boccaletti, A., Coulais, A., Decin, L., Edwards, B., Gastaud, R., Glasse, A., Kendrew, S., Olofsson, G., Patapis, P., Pye, J., Rouan, D., Whiteford, N., Argyriou, I., Cossou, C., Glauser, A. M., Krause, O., Lahuis, F., Royer, P., Scheithauer, S., Colina, L., van Dishoeck, E. F., Ostlin, G., Ray, T. P., and Wright, G. (2024). Combined analysis of the 12.8 and 15 μm jwst/miri eclipse observations of trappist-1 b. *Nature Astronomy*.

Engle, S. G. (2023). Living with a red dwarf: X-ray, uv, and ca ii activity–age relationships of m dwarfs. *The Astrophysical Journal*, 960(1):62.

Erwin, J., Tucker, O., and Johnson, R. E. (2013). Hybrid fluid/kinetic modeling of pluto's escaping atmosphere. *Icarus*, 226(1):375–384.

Ferland, G. J., Fabian, A. C., Hatch, N. A., Johnstone, R. M., Porter, R. L., Van Hoof, P. A. M., and Williams, R. J. R. (2009). Collisional heating as the origin of filament emission in galaxy clusters*. *MNRAS*, 392(4):1475–1502.

Feynman, R. P., Leighton, R. B., and Sands, M. (2011). *The Feynman lectures on physics, Vol. I: The new millennium edition: mainly mechanics, radiation, and heat*.

Fisher, C. E., Hooton, M. J., Gressier, A., Zgraggen, M., Tian, M., Heng, K., Allen, N. H., Chatterjee, R. D., Morris, B. M., Borsato, N. W., Espinoza, N., Kitzmann, D., Meier, T. G., Buchhave, L. A., Burgasser, A. J., Demory, B.-O., Fortune, M., Hoeijmakers, H. J., Luque, R., Valdés, E. A. M., Mendonça, J. M., Prinoth, B., Rathcke, A. D., and Taylor, J. (2025). JWST NIRSpec finds no clear signs of an atmosphere on TOI-1685 b. MNRAS.

Fleming, D. P., Barnes, R., Luger, R., and VanderPlas, J. T. (2020). On the XUV Luminosity Evolution of TRAPPIST-1. *The Astrophysical Journal*, 891(2):155.

France, K., Duvvuri, G., Egan, H., Koskinen, T., Wilson, D. J., Youngblood, A., Froning, C. S., Brown, A., Alvarado-Gómez, J. D., Berta-Thompson, Z. K., Drake, J. J., Garraffo, C., Kaltenegger, L., Kowalski, A. F., Linsky, J. L., Loyd, R. O. P., Mauas, P. J. D., Miguel, Y., Pineda, J. S., Rugheimer, S., Schneider, P. C., Tian, F., and Vieytes, M. (2020). The high-energy radiation environment around a 10 gyr m dwarf: Habitable at last? *The Astronomical Journal*, 160(5):237.

France, K., Fleming, B., Youngblood, A., Mason, J., Drake, J. J., Amerstorfer, U. V., Barstow, M., Bourrier, V., Champey, P., Fossati, L., Froning, C. S., Green, J. C., Grisé, F., Gronoff, G., Hellickson, T., Jin, M., Koskinen, T. T., Kowalski, A. F., Kruczek, N., Linsky, J. L., Lipscy,

S. J., McEntaffer, R. L., McKenzie, D. E., Miles, D. M., Patton, T., Savage, S., Siegmund, O., Spittler, C., Unruh, B. W., and Volz, M. (2022). Extreme-ultraviolet Stellar Characterization for Atmospheric Physics and Evolution mission: motivation and overview. *Journal of Astronomical Telescopes, Instruments, and Systems*, 8:014006.

France, K., Fleming, B., Youngblood, A., Mason, J., Drake, J. J., Amerstorfer, U. V., Barstow, M., Bourrier, V., Champey, P., Fossati, L., Froning, C. S., Green, J. C., Grisé, F., Gronoff, G., Hellickson, T., Jin, M., Koskinen, T. T., Kowalski, A. F., Kruczek, N., Linsky, J. L., Lipscy, S. J., McEntaffer, R. L., McKenzie, D. E., Miles, D. M., Patton, T., Savage, S., Siegmund, O., Spittler, C., Unruh, B. W., and Volz, M. (2022). Extreme-ultraviolet stellar characterization for atmospheric physics and evolution mission: motivation and overview. *Journal of Astronomical Telescopes, Instruments, and Systems*, 8(1):014006.

Fulton, B. J., Petigura, E. A., Howard, A. W., Isaacson, H., Marcy, G. W., Cargile, P. A., Hebb, L., Weiss, L. M., Johnson, J. A., Morton, T. D., et al. (2017). The california-kepler survey. iii. a gap in the radius distribution of small planets. *The Astronomical Journal*, 154(3):109.

García Muñoz, A. (2007). Physical and chemical aeronomy of HD 209458b. Planet. Space Sci., 55(10):1426–1455.

García Muñoz, A., Fossati, L., Youngblood, A., Nettelmann, N., Gandolfi, D., Cabrera, J., and Rauer, H. (2021). A Heavy Molecular Weight Atmosphere for the Super-Earth π Men c. ApJ, 907(2):L36.

García Muñoz, A., Asensio Ramos, A., and Faure, A. (2024). Nlte modelling of water-rich exoplanet atmospheres. cooling and heating rates. *Icarus*, 415:116080.

Gillon, M. (2024). The double phase curve of TRAPPIST-1b and c at 15 microns. In *EGU General Assembly Conference Abstracts*, EGU General Assembly Conference Abstracts, page 9116.

Gillon, M., Triaud, A. H. M. J., Demory, B.-O., Jehin, E., Agol, E., Deck, K. M., Lederer, S. M., de Wit, J., Burdanov, A., Ingalls, J. G., Bolmont, E., Leconte, J., Raymond, S. N., Selsis, F., Turbet, M., Barkaoui, K., Burgasser, A., Burleigh, M. R., Carey, S. J., Chaushev, A., Copperwheat, C. M., Delrez, L., Fernandes, C. S., Holdsworth, D. L., Kotze, E. J., Van Grootel, V., Almleaky, Y., Benkhaldoun, Z., Magain, P., and Queloz, D. (2017). Seven temperate terrestrial planets around the nearby ultracool dwarf star TRAPPIST-1. *Nature*, 542(7642):456–460. Publisher: Nature Publishing Group.

Goldsmith, P. F., Yildiz, U. A., Langer, W. D., and Pineda, J. L. (2015). Herschel galactic plane survey of [n ii] fine structure emission. *Astrophysical Journal*, 814.

Greene, T. P., Bell, T. J., Ducrot, E., Dyrek, A., Lagage, P.-O., and Fortney, J. J. (2023). Thermal Emission from the Earth-sized Exoplanet TRAPPIST-1 b using JWST. *Nature*, 618(7963):39–42. ADS Bibcode: 2023Natur.618...39G.

Gressier, A., Espinoza, N., Allen, N. H., Sing, D. K., Banerjee, A., Barstow, J. K., Valenti, J. A., Lewis, N. K., Birkmann, S. M., Challener, R. C., Manjavacas, E., Alves de Oliveira, C., Crouzet, N., and Beck, T. L. (2024a). Hints of a Sulfur-rich Atmosphere around the 1.6 $R_\oplus$ Super-Earth L98-59 d from JWST NIRspec G395H Transmission Spectroscopy. *The Astrophysical Journal Letters*, 975(1):L10.

Gressier, A., MacDonald, R. J., Espinoza, N., Wakeford, H. R., Lewis, N. K., Goyal, J., Louie, D. R., Radica, M., Batalha, N. E., Long, D., May, E. M., Mullens, E., Seager, S., Stevenson, K. B., Valenti, J. A., Alderson, L., Allen, N. H., Cañas, C. I., Challener, R. C., Colòn, K., Glidden, A., Grant, D., Huang, J., Lin, Z., Valentine, D., Mountain, C. M., Pueyo, L., Perrin, M. D., and van der Marel, R. P. (2024b). JWST-TST DREAMS: A Super-Solar Metallicity in WASP-17 b Dayside Atmosphere from NIRISS SOSS Eclipse Spectroscopy. *arXiv e-prints*, page arXiv:2410.08149.

Gronoff, G., Arras, P., Baraka, S., Bell, J. M., Cessateur, G., Cohen, O., Curry, S. M., Drake, J. J., Elrod, M., Erwin, J., Garcia-Sage, K., Garraffo, C., Glocer, A., Heavens, N. G., Lovato, K., Maggiolo, R., Parkinson, C. D., Simon Wedlund, C., Weimer, D. R., and Moore, W. B. (2020a). Atmospheric Escape Processes and Planetary Atmospheric Evolution. *Journal of Geophysical Research: Space Physics*, 125(8):e2019JA027639.

Gronoff, G., Arras, P., Baraka, S., Bell, J. M., Cessateur, G., Cohen, O., Curry, S. M., Drake, J. J., Elrod, M., Erwin, J., Garcia-Sage, K., Garraffo, C., Glocer, A., Heavens, N. G., Lovato, K., Maggiolo, R., Parkinson, C. D., Simon Wedlund, C., Weimer, D. R., and Moore, W. B. (2020b). Atmospheric escape processes and planetary atmospheric evolution. *JGRA*, 125(8).

Guinan, E. F., Engle, S. G., and Durbin, A. (2016). Living with a red dwarf: Rotation and x-ray and ultraviolet properties of the halo population kapteyn's star. *The Astrophysical Journal*, 821(2):81. Publisher: The American Astronomical Society.

Gunell, Herbert, Maggiolo, Romain, Nilsson, Hans, Stenberg Wieser, Gabriella, Slapak, Rikard, Lindkvist, Jesper, Hamrin, Maria, and De Keyser, Johan (2018). Why an intrinsic magnetic field does not protect a planet against atmospheric escape. *A&A*, 614:L3.

Hammond, M., Guimond, C. M., Lichtenberg, T., Nicholls, H., Fisher, C., Luque, R., Meier, T. G., Taylor, J., Changeat, Q., Dang, L., Hay, H. C. F. C., Herbort, O., and Teske, J. (2025). Reliable Detections of Atmospheres on Rocky Exoplanets with Photometric JWST Phase Curves. *The Astrophysical Journal Letters*, 978(2):L40.

Hammond, M., Guimond, C. M., Lichtenberg, T., Nicholls, H., Fisher, C., Luque, R., Meier, T. G., Taylor, J., Changeat, Q., Dang, L., Herbort, O., and Teske, J. (2024). Reliable Detections of Atmospheres on Rocky Exoplanets with Photometric JWST Phase Curves. Publication Title: arXiv e-prints ADS Bibcode: 2024arXiv240904386H.

Hanson, L., Cohen, O., Ridley, A. J., and Glocer, A. (2025). The impact of enhanced extreme-ultraviolet flux on the upper atmosphere of earth-like exoplanets. *The Astrophysical Journal*, 992(1):58.

Heays, Bosman, A. D., and van Dishoeck, E. F. (2017). Photodissociation and photoionisation of atoms and molecules of astrophysical interest. *A&A*, 602:A105.

Hertel, I. V. and Schulz, C.-P. (2015). *Inelastic Collisions – A First Overview*, pages 453–513. Springer Berlin Heidelberg, Berlin, Heidelberg.

Holzer, T. E. and Axford, W. I. (1970). The theory of stellar winds and related flows. *Annual Review of Astronomy and Astrophysics*, 8(1):31–60.

Hong, J. M., Yen, C. C., and Huang, B. C. (2014). Characterization of the transonic stationary solutions of the hydrodynamic escape problem. *SJADS*, 74:1709–1741.

Hord, B. J., Kempton, E. M. R., Evans-Soma, T. M., and Latham, D. W. (2024). Identification of the Top TESS Objects of Interest for Atmospheric Characterization of Transiting Exoplanets with JWST. AJ, 167(5):233.

Hu, R., Bello-Arufe, A., Zhang, M., Paragas, K., Zilinskas, M., van Buchem, C., Bess, M., Patel, J., Ito, Y., Damiano, M., Scheucher, M., Oza, A. V., Knutson, H. A., Miguel, Y., Dragomir, D., Brandeker, A., and Demory, B.-O. (2024). A secondary atmosphere on the rocky exoplanet 55 Cancri e. *Nature*, 630(8017):609–612. A secondary atmosphere on the rocky Exoplanet 55 Cancri e.

Hu, R. and Thomas, T. B. (2022). A nitrogen-rich atmosphere on ancient mars consistent with isotopic evolution models. *Nature Geoscience*, 15:106–111.

Huang, S.-S. (1959). The problem of life in the universe and the mode of star formation. *PASP*, 71(422):421.

Huebner, W. F. and Mukherjee, J. (2015). Photoionization and photodissociation rates in solar and blackbody radiation fields. *Planetary and Space Science*, 106:11–45.

Ito, Y. and Ikoma, M. (2020). Hydrodynamic escape of mineral atmosphere from hot rocky exoplanet. i. model description.

Jackson, A. P., Davis, T. A., and Wheatley, P. J. (2012). The coronal X-ray-age relation and its implications for the evaporation of exoplanets: X-ray-age relation and exoplanet evaporation. *Monthly Notices of the Royal Astronomical Society*, 422(3):2024–2043.

Jeans, J. H. (1921). *The dynamical theory of gases*. University Press.

Ji, X., Chatterjee, R. D., Coy, B. P., and Kite, E. (2025). The Cosmic Shoreline Revisited: A Metric for Atmospheric Retention Informed by Hydrodynamic Escape. ApJ, 992(2):198.

Johnson, R. E., Volkov, A. N., and Erwin, J. T. (2013a). molecular-kinetic simulations of escape from the ex-planet and exoplanets: Criterion for transonic flow. *ApJL*, 768(1):L4.

Johnson, R. E., Volkov, A. N., and Erwin, J. T. (2013b). Erratum: "molecular-kinetic simulations of escape from the ex-planet and exoplanets: Criterion for transonic flow" (2013, apjl, 768, l4). *The Astrophysical Journal*, 779:L30.

Johnstone, Khodachenko, M. L., Lüftinger, T., Kislyakova, K. G., Lammer, H., and Güdel, M. (2019). Extreme hydrodynamic losses of earth-like atmospheres in the habitable zones of very active stars. *A&A*, 624:L10.

Johnstone, C. P. (2020). Hydrodynamic escape of water vapor atmospheres near very active stars. *The Astrophysical Journal*, 890(1):79.

Johnstone, C. P., Bartel, M., and Güdel, M. (2021). The active lives of stars: A complete description of the rotation and XUV evolution of F, G, K, and M dwarfs. *Astronomy & Astrophysics*, 649:A96.

Kasting, J. F. (1988). Runaway and moist greenhouse atmospheres and the evolution of earth and venus. *Icarus*, 74(3):472–494.

Kasting, J. F. and Pollack, J. B. (1983). Loss of water from venus. i. hydrodynamic escape of hydrogen. *Icarus*, 53(3):479–508.

Kasting, J. F., Whitmire, D. P., and Reynolds, R. T. (1993). Habitable zones around main sequence stars. *Icarus*, 101(1):108–128.

Keil, K. (1989). Enstatite meteorites and their parent bodies. *Meteoritics (ISSN 0026-1114), vol. 24, Dec. 1989, p. 195-208.*, 24:195–208.

Kempton, E. M.-R., Bean, J. L., Louie, D. R., Deming, D., Koll, D. D. B., Mansfield, M., Christiansen, J. L., López-Morales, M., Swain, M. R., Zellem, R. T., Ballard, S., Barclay, T., Barstow, J. K., Batalha, N. E., Beatty, T. G., Berta-Thompson, Z., Birkby, J., Buchhave, L. A., Charbonneau, D., Cowan, N. B., Crossfield, I., Val-Borro, M. d., Doyon, R., Dragomir, D., Gaidos, E., Heng, K., Hu, R., Kane, S. R., Kreidberg, L., Mallonn, M., Morley, C. V., Narita, N., Nascimbeni, V., Pallé, E., Quintana, E. V., Rauscher, E., Seager, S., Shkolnik, E. L., Sing, D. K., Sozzetti, A., Stassun, K. G., Valenti, J. A., and Essen, C. v. (2018). A Framework for Prioritizing the *TESS* Planetary Candidates Most Amenable to Atmospheric Characterization. *Publications of the Astronomical Society of the Pacific*, 130(993):114401.

Khodachenko, M. L., Shaikhislamov, I. F., Lammer, H., and Prokopov, P. A. (2015). Atmosphere expansion and mass loss of close-orbit giant exoplanets heated by stellar xuv. ii. effects of planetary magnetic field; structuring of inner magnetosphere. *Astrophysical Journal*, 813.

King, G. W. and Wheatley, P. J. (2020). EUV irradiation of exoplanet atmospheres occurs on Gyr time-scales. *Monthly Notices of the Royal Astronomical Society: Letters*, 501(1):L28–L32.

Kirk, J., Stevenson, K. B., Fu, G., Lustig-Yaeger, J., Moran, S. E., Peacock, S., Alam, M. K., Batalha, N. E., Bennett, K. A., Gonzalez-Quiles, J., López-Morales, M., Lothringer, J. D., MacDonald, R. J., May, E. M., Mayorga, L. C., Rustamkulov, Z., Sing, D. K., Sotzen, K. S., Valenti, J. A., and Wakeford, H. R. (2024). JWST/NIRCam Transmission Spectroscopy of the Nearby Sub-Earth GJ 341b. *The Astronomical Journal*, 167(3):90. Publisher: IOP ADS Bibcode: 2024AJ....167...90K.

Kislyakova, Holmström, M., Odert, P., Lammer, H., Erkaev, N. V., Khodachenko, M. L., Shaikhislamov, I. F., Dorfi, E., and Güdel, M. (2019). Transit lyman- signatures of terrestrial planets in the habitable zones of m dwarfs. *A&A*, 623:A131.

Kite, E. S. (2019). Geologic Constraints on Early Mars Climate. Space Sci. Rev., 215(1):10.

Kite, E. S. and Barnett, M. N. (2020). Exoplanet secondary atmosphere loss and revival. *PNAS*.

Kite, E. S., Tutolo, B. M., Turner, M. L., Franz, H. B., Burtt, D. G., Bristow, T. F., Fischer, W. W., Milliken, R. E., Fraeman, A. A., and Zhou, D. Y. (2025). Carbonate formation and fluctuating habitability on Mars. Nature, 643(8070):60–66.

Knudsen, M. (1909). Die gesetze der molekularströmung und der inneren reibungsströmung der gase durch röhren. *AnP*, 333:75–130.

Koll, D. D. B. (2022). A Scaling for Atmospheric Heat Redistribution on Tidally Locked Rocky Planets. *The Astrophysical Journal*, 924(2):134.

Kopparapu, R. K., Ramirez, R., Kasting, J. F., Eymet, V., Robinson, T. D., Mahadevan, S., Terrien, R. C., Domagal-Goldman, S., Meadows, V., and Deshpande, R. (2013). HABITABLE ZONES AROUND MAIN-SEQUENCE STARS: NEW ESTIMATES. *The Astrophysical Journal*, 765(2):131.

Koskinen, T., Harris, M., Yelle, R., and Lavvas, P. (2013). The escape of heavy atoms from the ionosphere of hd209458b. i. a photochemical–dynamical model of the thermosphere. *Icarus*, 226(2):1678–1694.

Kreidberg, L. (2023). Search for distant atmosphere off to a rocky start. Nature, 618(7963):32–33.

Kreidberg, L., Koll, D. D., Morley, C., Hu, R., Schaefer, L., Deming, D., Stevenson, K. B., Dittmann, J., Vanderburg, A., Berardo, D., et al. (2019). Absence of a thick atmosphere on the terrestrial exoplanet lhs 3844b. *Nature*, 573(7772):87–90.

Kreidberg, L. and Stevenson, K. B. (2025). A first look at rocky exoplanets with JWST. *arXiv e-prints*, page arXiv:2507.00933.

Krissansen-Totton, J., Wogan, N., Thompson, M., and Fortney, J. J. (2024). The erosion of large primary atmospheres typically leaves behind substantial secondary atmospheres on temperate rocky planets. *Nature communications*, 15(8374):1–16. Publisher: Nature Publishing Group.

Kubyshkina, D., Fossati, L., Erkaev, N. V., Cubillos, P. E., Johnstone, C. P., Kislyakova, K. G., Lammer, H., Lendl, M., and Odert, P. (2018). Overcoming the limitations of the energy-limited approximation for planet atmospheric escape. *The Astrophysical Journal Letters*, 866(2):L18.

Kunc, J. A. and Soon, W. H. (1989). Collisional-radiative nonequilibrium in partially ionized atomic nitrogen.

Kuramoto, K., Umemoto, T., and Ishiwatari, M. (2013). Effective hydrodynamic hydrogen escape from an early earth atmosphere inferred from high-accuracy numerical simulation. *Earth and Planetary Science Letters*, 375:312–318.

Lamers, H. and Cassinelli, J. (1999). *Introduction to Stellar Winds*. Cambridge University Press.

Lammer, H., Sproß, L., Grenfell, J. L., Scherf, M., Fossati, L., Lendl, M., and Cubillos, P. E. (2019). The Role of N_2 as a Geo-Biosignature for the Detection and Characterization of Earth-like Habitats. *Astrobiology*, 19(7):927–950.

Lammer, H., Zerkle, A. L., Gebauer, S., Tosi, N., Noack, L., Scherf, M., Pilat-Lohinger, E., Güdel, M., Grenfell, J. L., Godolt, M., and Nikolaou, A. (2018). Origin and evolution of the atmospheres of early venus, earth and mars. *Astronomy and Astrophysics Review*, 26.

Laricchiuta, A., Bruno, D., Capitelli, M., Catalfamo, C., Celiberto, R., Colonna, G., Diomede, P., Giordano, D., Gorse, C., Longo, S., Pagano, D., and Pirani, F. (2009). High temperature mars atmosphere. part i: Transport cross sections. *EPJD*, 54:607–612.

Lehmer, O. R. and Catling, D. C. (2017). Rocky worlds limited to 1.8 earth radii by atmospheric escape during a star's extreme uv saturation. *The Astrophysical Journal*, 845(2):130.

Looveren, G. V., Saikia, S. B., Herbort, O., Schleich, S., Gudel, M., Johnstone, C., and Kislyakova, K. (2025). Habitable zone and atmosphere retention distance (hazard) stellar-evolution-dependent loss models of secondary atmospheres.

Lopez, E. D. and Fortney, J. J. (2013). THE ROLE OF CORE MASS IN CONTROLLING EVAPORATION: THE KEPLER RADIUS DISTRIBUTION AND THE KEPLER-36 DENSITY DICHOTOMY. *The Astrophysical Journal*, 776(1):2.

Loyd, R. O. P., Shkolnik, E. L., Schneider, A. C., Barman, T. S., Meadows, V. S., Pagano, I., and Peacock, S. (2018). Hazmat. iv. flares and superflares on young m stars in the far ultraviolet*. *The Astrophysical Journal*, 867(1):70.

Luque, R., Coy, B. P., Xue, Q., Feinstein, A. D., Ahrer, E.-M., Changeat, Q., Zhang, M., Moran, S. E., Bean, J. L., Kite, E., Weiner Mansfield, M., and Pallé, E. (2025). A Dark, Bare Rock for TOI-1685 b from a JWST NIRSpec G395H Phase Curve. AJ, 170(1):49.

Lustig-Yaeger, J., Fu, G., May, E. M., Ceballos, K. N. O., Moran, S. E., Peacock, S., Stevenson, K. B., Kirk, J., López-Morales, M., MacDonald, R. J., Mayorga, L. C., Sing, D. K., Sotzen, K. S., Valenti, J. A., Redai, J. I. A., Alam, M. K., Batalha, N. E., Bennett, K. A., Gonzalez-Quiles, J., Kruse, E., Lothringer, J. D., Rustamkulov, Z., and Wakeford, H. R. (2023). A JWST transmission spectrum of the nearby Earth-sized exoplanet LHS 475 b. *Nature Astronomy*, 7(11):1317–1328. ADS Bibcode: 2023NatAs...7.1317L.

López-Puertas, M. and Taylor, F. W. (2001). *Non-LTE Radiative Transfer in the Atmosphere*. World Scientific.

Magaudda, E., Stelzer, B., Raetz, St., Klutsch, A., Salvato, M., and Wolf, J. (2022). First erosita study of nearby m dwarfs and the rotation-activity relation in combination with tess. *AA*, 661:A29.

Mamajek, E. E. (2022). A modern mean dwarf stellar color and effective temperature sequence. `http://www.pas.rochester.edu/~emamajek/EEM_dwarf_UBVIJHK_colors_Teff.txt`. Version 2022.04.16. Online table.

Mansfield, M. W., Xue, Q., Zhang, M., Mahajan, A. S., Ih, J., Koll, D., Bean, J. L., Coy, B. P., Eastman, J. D., Kempton, E. M.-R., Kite, E. S., and Lunine, J. (2024). No Thick Atmosphere on the Terrestrial Exoplanet Gl 486b. arXiv:2408.15123 [astro-ph].

Marvin, C. J., Reiners, A., Anglada-Escudé, G., Jeffers, S. V., and Boro Saikia, S. (2023). Absolute Ca II H & K and H-alpha flux measurements of low-mass stars: Extending R'$_{HK}$ to M dwarfs. A&A, 671:A162.

Maxence Lefèvre, Martin Turbet, R. P. (2021). 3d convection-resolving model of temperate, tidally-locked exoplanets. *The Astrophysical Journal*.

Mayor, M. and Queloz, D. (1995). A jupiter-mass companion to a solar-type star. *nature*, 378(6555):355–359.

Meier, T. G., Pierrehumbert, R. T., Birkby, J., Chatterjee, R. D., Fisher, C. E., Guimond, C. M., Golabek, G. J., Hammond, M., Komacek, T. D., Lichtenberg, T., McGinty, A., Meier Valdés, E., Nicholls, H., Parker, L. T., Spaargaren, R. J., and Tackley, P. J. (2025). Mantle Convection and Nightside Volcanism on Lava World K2-141 b. *Monthly Notices of the Royal Astronomical Society*. Submitted.

Meier Valdés, E. A., Demory, B. O., Diamond-Lowe, H., Mendonça, J. M., August, P. C., Fortune, M., Allen, N. H., Kitzmann, D., Gressier, A., Hooton, M., Jones, K. D., Buchhave, L. A., Espinoza, N., Fisher, C. E., Gibson, N. P., Heng, K., Hoeijmakers, J., Prinoth, B., Rathcke, A. D., and Eastman, J. D. (2025). Hot Rocks Survey: II. The thermal emission of TOI-1468 b reveals a bare hot rock. A&A, 698:A68.

Ment, K. and Charbonneau, D. (2023). The Occurrence Rate of Terrestrial Planets Orbiting Nearby Mid-to-late M Dwarfs from TESS Sectors 1-42. AJ, 165(6):265.

Modirrousta-Galian, D., Stelzer, B., Magaudda, E., Maldonado, J., Güdel, M., Sanz-Forcada, J., Edwards, B., and Micela, G. (2020). GJ 357 b. A super-Earth orbiting an extremely inactive host star. *Astronomy and Astrophysics*, 641:A113. ADS Bibcode: 2020A&A...641A.113M.

Monaghan, C., Roy, P.-A., Benneke, B., Crossfield, I. J. M., Coulombe, L.-P., Piaulet-Ghorayeb, C., Kreidberg, L., Dressing, C. D., Kane, S. R., Dragomir, D., Werner, M. W., Parmentier, V., Christiansen, J. L., Morales, F. Y., Berardo, D., and Gorjian, V. (2025). Low 4.5 μm Dayside Emission Disfavors a Dark Bare-rock Scenario for the Hot Super-Earth TOI-431 b. AJ, 169(5):239.

Murray-Clay, R. A., Chiang, E. I., and Murray, N. (2009). ATMOSPHERIC ESCAPE FROM HOT JUPITERS. *The Astrophysical Journal*, 693(1):23–42. Publisher: American Astronomical Society.

Nakayama, A., Ikoma, M., and Terada, N. (2022). Survival of Terrestrial N2–O2 Atmospheres in Violent XUV Environments through Efficient Atomic Line Radiative Cooling. *The Astrophysical Journal*, 937(2):72.

Namur, O., Charlier, B., Holtz, F., Cartier, C., and McCammon, C. (2016). Sulfur solubility in reduced mafic silicate melts: Implications for the speciation and distribution of sulfur on mercury. *Earth and Planetary Science Letters*, 448:102–114.

Nicholls, H., Guimond, C. M., Hay, H. C. F. C., Chatterjee, R. D., Lichtenberg, T., and Pierrehumbert, R. T. (2025a). Self-limited tidal heating and prolonged magma oceans in the L 98-59 system. MNRAS, 541(3):2566–2584.

Nicholls, H., Guimond, C. M., Hay, H. C. F. C., Chatterjee, R. D., Lichtenberg, T., and Pierrehumbert, R. T. (2025b). Self-limited tidal heating and prolonged magma oceans in the L 98-59 system. MNRAS, 541(3):2566–2584.

Nicholls, H., Hébrard, E., Venot, O., Drummond, B., and Evans, E. (2023). Temperature–chemistry coupling in the evolution of gas giant atmospheres driven by stellar flares. *Monthly Notices of the Royal Astronomical Society*, 523(4):5681–5702.

Nicholls, H., Lichtenberg, T., Chatterjee, R. D., Guimond, C. M., Postolec, E., and Pierrehumbert, R. T. (2025c). Volatile-rich evolution of molten super-Earth L 98-59 d. arXiv.

Nikolov, N. K., Kovacs, A., and Martlin, C. (2022). TrExoLiSTS: Transiting Exoplanets List of Space Telescope Spectroscopy. *Research Notes of the American Astronomical Society*, 6(12):272.

O'Brien, P. (2017). One-dimensional models of atmospheric escape to space. MPhys project, University of Oxford, Atmospheric Oceanic and Planetary Physics.

Omang, M., Børve, S., and Trulsen, J. (2006). SPH in spherical and cylindrical coordinates. *Journal of Computational Physics*, 213(1):391–412.

Owen, J. E. (2019). Atmospheric Escape and the Evolution of Close-In Exoplanets. *Annual Review of Earth and Planetary Sciences*, 47(1):67–90.

Owen, J. E. and Adams, F. C. (2014). Magnetically controlled mass-loss from extrasolar planets in close orbits. *Monthly Notices of the Royal Astronomical Society*, 444:3761–3779. ADS Bibcode: 2014MNRAS.444.3761O.

Owen, J. E. and Jackson, A. P. (2012). Planetary evaporation by uv and x-ray radiation: Basic hydrodynamics. *Monthly Notices of the Royal Astronomical Society*, 425:2931–2947.

Owen, J. E. and Wu, Y. (2013). *KEPLER* PLANETS: A TALE OF EVAPORATION. *The Astrophysical Journal*, 775(2):105.

Parker, E. N. (1958). Dynamics of the interplanetary gas and magnetic fields. *The Astrophysical Journal*, 128.

Pecaut, M. J. and Mamajek, E. E. (2013). Intrinsic Colors, Temperatures, and Bolometric Corrections of Pre-main-sequence Stars. ApJS, 208(1):9.

Penz, T. and Micela, G. (2008). X-ray induced mass loss effects on exoplanets orbiting dM stars. A&A, 479(2):579–584.

Piaulet-Ghorayeb, C., Benneke, B., Turbet, M., Moore, K., Roy, P.-A., Lim, O., Doyon, R., Fauchez, T. J., Albert, L., Radica, M., Coulombe, L.-P., Lafrenière, D., Cowan, N. B., Belzile, D., Musfirat, K., Kaur, M., L'Heureux, A., Johnstone, D., MacDonald, R. J., Allart, R., Dang, L., Kaltenegger, L., Pelletier, S., Rowe, J. F., Taylor, J., and Turner, J. D. (2025). Strict limits on potential secondary atmospheres on the temperate rocky exo-Earth TRAPPIST-1 d. *arXiv e-prints*, page arXiv:2508.08416.

Pierrehumbert, R. (2010a). *Principles of planetary climate*. Cambridge University Press, Cambridge New York.

Pierrehumbert, R. T. (2010b). *Principles of planetary climate*. Cambridge University Press.

Press, W. H., William, H., Teukolsky, S. A., Vetterling, W. T., Saul, A., and Flannery, B. P. (2007). *Numerical recipes 3rd edition: The art of scientific computing*. Cambridge university press.

Radica, M., Piaulet-Ghorayeb, C., Taylor, J., Coulombe, L.-P., Albert, L., Artigau, , Benneke, B., Cowan, N. B., Doyon, R., Lafrenière, D., L'Heureux, A., and Lim, O. (2024). Promise and Peril: Stellar Contamination and Strict Limits on the Atmosphere Composition of TRAPPIST-1c from JWST NIRISS Transmission Spectra. Publication Title: arXiv e-prints ADS Bibcode: 2024arXiv240919333R.

Radica, M., Piaulet-Ghorayeb, C., Taylor, J., Coulombe, L.-P., Benneke, B., Albert, L., Artigau, , Cowan, N. B., Doyon, R., Lafrenière, D., L'Heureux, A., and Lim, O. (2025). Promise and Peril: Stellar Contamination and Strict Limits on the Atmosphere Composition of TRAPPIST-1 c from JWST NIRISS Transmission Spectra. *The Astrophysical Journal Letters*, 979(1):L5.

Rajpaul, V. M., Barragán, O., and Zicher, N. (2024). A non-zero Doppler amplitude is not enough: revisiting the putative radial velocity detection of sub-Venus exoplanet L 98-59b. MNRAS, 530(4):4665–4675.

Rauer, H., Aerts, C., Cabrera, J., Deleuil, M., Erikson, A., Gizon, L., Goupil, M., Heras, A., Walloschek, T., Lorenzo-Alvarez, J., Marliani, F., Martin-Garcia, C., Mas-Hesse, J. M., O'Rourke, L., Osborn, H., Pagano, I., Piotto, G., Pollacco, D., Ragazzoni, R., Ramsay, G., Udry, S., Appourchaux, T., Benz, W., Brandeker, A., Güdel, M., Janot-Pacheco, E., Kabath, P., Kjeldsen, H., Min, M., Santos, N., Smith, A., Suarez, J.-C., Werner, S. C., Aboudan, A., Abreu, M., Acuña, L., Adams, M., Adibekyan, V., Affer, L., Agneray, F., Agnor, C., Aguirre Børsen-Koch, V., Ahmed, S., Aigrain, S., Al-Bahlawan, A., Alcacera Gil, M. d. l. A., Alei, E., Alencar, S., Alexander, R., Alfonso-Garzón, J., Alibert, Y., Allende Prieto, C., Almeida, L., Alonso Sobrino, R., Altavilla, G., Althaus, C., Alvarez Trujillo, L. A., Amarsi, A., Ammler-von Eiff, M., Amôres, E., Andrade, L., Antoniadis-Karnavas, A., António, C., Aparicio del Moral, B., Appolloni, M., Arena, C., Armstrong, D., Aroca Aliaga, J., Asplund, M., Audenaert, J., Auricchio, N., Avelino, P., Baeke, A., Baillié, K., Balado, A., Ballber Balagueró, P., Balestra, A., Ball, W., Ballans, H., Ballot, J., Barban, C., Barbary, G., Barbieri, M., Barceló Forteza, S., Barker, A., Barklem, P., Barnes, S., Barrado Navascues, D., Barragan, O., Baruteau, C., Basu, S., Baudin, F., Baumeister, P., Bayliss, D., Bazot, M., Beck, P. G., Belkacem, K., Bellinger, E., Benatti, S., Benomar, O., Bérard, D., Bergemann, M., Bergomi, M., Bernardo, P., Biazzo, K., Bignamini, A., Bigot, L., Billot, N., Binet, M., Biondi, D., Biondi, F., Birch, A. C., Bitsch, B., Bluhm Ceballos, P. V., Bódi, A., Bognár, Z., Boisse, I., Bolmont, E., Bonanno, A., Bonavita, M., Bonfanti, A., Bonfils, X., Bonito, R., Bonomo, A. S., Börner, A., Boro Saikia, S., Borreguero Martín, E., Borsa, F., Borsato, L., Bossini, D., Bouchy, F., Boué, G., Boufleur, R., Boumier, P., Bourrier, V., Bowman, D. M., Bozzo, E., Bradley, L., Bray, J., Bressan, A., Breton, S., Brienza, D., Brito, A., Brogi, M., Brown, B., Brown, D. J. A., Brun, A. S., Bruno, G., Bruns, M., Buchhave, L. A., Bugnet, L., Buldgen, G., Burgess, P., Busatta, A., Busso, G., Buzasi, D., Caballero, J. A., Cabral, A., Cabrero Gomez, J.-F., Calderone, F., Cameron, R., Cameron, A., Campante, T., Campos Gestal, N., Canto Martins, B. L., Cara, C., Carone, L., Carrasco, J. M., Casagrande, L., Casewell, S. L., Cassisi, S., Castellani, M., Castro, M., Catala, C., Catalán Fernández, I., Catelan, M., Cegla, H., Cerruti, C., Cessa, V., Chadid, M., Chaplin, W., Charpinet, S., Chiappini, C., Chiarucci, S., Chiavassa, A., Chinellato, S., Chirulli, G., Christensen-Dalsgaard, J., Church, R., Claret, A., Clarke, C., Claudi, R., Clermont, L., Coelho, H., Coelho, J., Cogato, F., Colomé, J., Condamin, M., Conde García, F., and Conseil, S. (2025). The PLATO mission. *Experimental Astronomy*, 59(3):26.

Redfield, S., Batalha, N., Benneke, B., Biller, B., Espinoza, N., France, K., Konopacky, Q., Kreidberg, L., Rauscher, E., and Sing, D. (2024). Report of the Working Group on Strategic Exoplanet Initiatives with HST and JWST. *arXiv e-prints*, page arXiv:2404.02932. arXiv:2404.02932.

Ribas, I., Guinan, E. F., Güdel, M., and Audard, M. (2005). Evolution of the solar activity over time and effects on planetary atmospheres. i. high-energy irradiances (1-1700 Å). *ApJ*, 622(1):680.

Rogers, J. G. and Owen, J. E. (2021). Unveiling the planet population at birth. *Monthly Notices of the Royal Astronomical Society*, 503(1):1526–1542.

Sasaki, T. (2008). Numerical study of multi-component hydrodynamic escape: Application to the early venusian atmosphere.

Scarsdale, N., Wogan, N., Wakeford, H. R., Wallack, N. L., Batalha, N. E., Alderson, L., Aguichine, A., Wolfgang, A., Teske, J., Moran, S. E., López-Morales, M., Kirk, J., Gordon, T., Gao, P., Batalha, N. M., Alam, M. K., and Redai, J. A. (2024). Jwst compass: The 3–5 m transmission spectrum of the super-earth l 98-59 c. *The Astronomical Journal*, 168(6):276.

Scherf, M., Lammer, H., and Sproß, L. (2022). Eta earth revisited: How many earth-like habitats might there be in the milky way? In *EPSC 2022*, Granada. EPSC2022-1032.

Schulik, M. and Booth, R. A. (2023). AIOLOS - A multipurpose 1D hydrodynamics code for planetary atmospheres. MNRAS, 523(1):286–304.

Seaton, M. J. (1960). Planetary nebulae. *RPPh*, 23(1):313.

Sekiya, M., Nakazawa, K., and Hayashi, C. (1980). Dissipation of the Primordial Terrestrial Atmosphere Due to Irradiation of the Solar EUV. *Progress of Theoretical Physics*, 64(6):1968–1985.

Selsis, F., Kasting, J. F., Levrard, B., Paillet, J., Ribas, I., and Delfosse, X. (2007). Habitable planets around the star Gliese 581? A&A, 476(3):1373–1387.

Solomon, S. C. (2010). *Terrestrial ionospheres*, page 351–362. Cambridge University Press.

Spinelli, R., Gallo, E., Haardt, F., Caldiroli, A., Biassoni, F., Borsa, F., and Rauscher, E. (2023). Planetary parameters, xuv environments, and mass-loss rates for nearby gaseous planets with x-ray-detected host stars. *AJ*, 165(5):200.

Spitzer, Lyman, J. (1949). The Terrestrial Atmosphere above 300 KM. In Kuiper, G. P., editor, *The Atmospheres of the Earth and Planets*, page 211. Chicago Press.

Spitzer, L. J. (1978). *Physical processes in the interstellar medium*. Wiley.

Strangeway, R. J., Russell, C. T., Luhmann, J. G., Moore, T. E., Foster, J. C., Barabash, S. V., and Nilsson, H. (2010). Does a Planetary-Scale Magnetic Field Enhance or Inhibit Ionospheric Plasma Outflows? In *AGU Fall Meeting Abstracts*, volume 2010, pages SM33B–1893. ADS Bibcode: 2010AGUFMSM33B1893S.

Struve, O. (1952). Proposal for a project of high-precision stellar radial velocity work. *The Observatory*, 72:199–200.

Tang, Y., Fortney, J. J., and Murray-Clay, R. (2024). Assessing Core-powered Mass Loss in the Context of Early Boil-off: Minimal Long-lived Mass Loss for the Sub-Neptune Population. *The Astrophysical Journal*, 976(2):221. ADS Bibcode: 2024ApJ...976..221T.

Taylor, J., Radica, M., Chatterjee, R. D., Hammond, M., Meier, T., Aigrain, S., MacDonald, R. J., Albert, L., Benneke, B., Coulombe, L.-P., Cowan, N. B., Dang, L., Doyon, R., Flagg, L., Johnstone, D., Kaltenegger, L., Lafrenière, D., Pelletier, S., Piaulet-Ghorayeb, C., Rowe, J. F., and Roy, P.-A. (2025). JWST NIRISS transmission spectroscopy of the super-Earth GJ 357b, a favourable target for atmospheric retention. MNRAS, 540(4):3677–3692.

Teixeira, K. E., Morley, C. V., Foley, B. J., and Unterborn, C. T. (2023). The carbon-deficient evolution of trappist-1c. *ApJ*, 960(1):44.

Tian, F. (2009). Thermal Escape from Super Earth Atmospheres in the Habitable Zones of M Stars. *The Astrophysical Journal*, 703(1):905–909. ADS Bibcode: 2009ApJ...703..905T.

Tian, F., Kasting, J. F., Liu, H. L., and Roble, R. G. (2008). Hydrodynamic planetary thermosphere model: 1. response of the earth's thermosphere to extreme solar euv conditions and the significance of adiabatic cooling. *Journal of Geophysical Research E: Planets*, 113.

Tian, F., Kasting, J. F., and Solomon, S. C. (2009). Thermal escape of carbon from the early martian atmosphere. *GRL*, 36.

Tian, F., Toon, O. B., Pavlov, A. A., and Sterck, H. D. (2005). Transonic Hydrodynamic Escape of Hydrogen from Extrasolar Planetary Atmospheres. *The Astrophysical Journal*, 621(2):1049–1060.

Tucker, W. H. and Gould, R. J. (1966). Radiation from a Low-Density Plasma at 10^6 ° - 10^8 ° K. ApJ, 144:244.

Van Looveren, G., Güdel, M., Boro Saikia, S., and Kislyakova, K. (2024). Airy worlds or barren rocks? on the survivability of secondary atmospheres around the trappist-1 planets. *A&A*.

Velli, M. (1994). From Supersonic Winds to Accretion: Comments on the Stability of Stellar Winds and Related Flows. ApJ, 432:L55.

Venot, O., Rocchetto, M., Carl, S., Hashim, A. R., and Decin, L. (2016). INFLUENCE OF STELLAR FLARES ON THE CHEMICAL COMPOSITION OF EXOPLANETS AND SPECTRA. *The Astrophysical Journal*, 830(2):77.

Vidal-Madjar, A., Des Etangs, A. L., Désert, J.-M., Ballester, G., Ferlet, R., Hébrard, G., and Mayor, M. (2003). An extended upper atmosphere around the extrasolar planet hd209458b. *Nature*, 422(6928):143–146.

Vidal-Madjar, A., Dsert, J.-M., des Etangs, A. L., Hbrard, G., Ballester, G. E., Ehrenreich, D., Ferlet, R., McConnell, J. C., Mayor, M., and Parkinson, C. D. (2004). Detection of oxygen and carbon in the hydrodynamically escaping atmosphere of the extrasolar planet HD 209458b. *The Astrophysical Journal*, 604(1):L69–L72.

Vilhu, O. (1984). The nature of magnetic activity in lower main sequence stars. A&A, 133:117–126.

Volkov, A. (2017). Me 491/591 non-equilibrium gas dynamics: Chapter 6, direct simulation monte carlo (dsmc) method. Course notes, University of Alabama. Spring 2017, ME 491/591 Non-Equilibrium Gas Dynamics, Dr. Alexey Volkov.

Volkov, A. N., Tucker, O. J., Erwin, J. T., and Johnson, R. E. (2011). Kinetic simulations of thermal escape from a single component atmosphere. *Physics of Fluids*, 23.

Wachiraphan, P., Berta-Thompson, Z. K., Diamond-Lowe, H., Winters, J. G., Murray, C., Zhang, M., Xue, Q., Morley, C. V., Rosario-Franco, M., and Duvvuri, G. M. (2025). The Thermal Emission Spectrum of the Nearby Rocky Exoplanet LTT 1445A b from JWST MIRI/LRS. AJ, 169(6):311.

Wagner, W. (1992). A convergence proof for bird's direct simulation monte carlo method for the boltzmann equation. *Journal of Statistical Physics*, 66(3-4):1011–1044.

Watson, A. J., Donahue, T. M., and Ker, J. C. G. W. (1981). The dynamics of a rapidly escaping atmosphere: Applications to the evolution of earth and venus. *Icarus*, 48:150–166.

Williams, R. E., Blacker, B., Dickinson, M., Dixon, W. V. D., Ferguson, H. C., Fruchter, A. S., Giavalisco, M., Gilliland, R. L., Heyer, I., Katsanis, R., Levay, Z., Lucas, R. A., McElroy, D. B., Petro, L., Postman, M., Adorf, H.-M., and Hook, R. (1996). The Hubble Deep Field: Observations, Data Reduction, and Galaxy Photometry. AJ, 112:1335.

Williams, R. M. E., Grotzinger, J. P., Dietrich, W. E., Gupta, S., Sumner, D. Y., Wiens, R. C., Mangold, N., Malin, M. C., Edgett, K. S., Maurice, S., Forni, O., Gasnault, O., Ollila, A., Newsom, H. E., Dromart, G., Palucis, M. C., Yingst, R. A., Anderson, R. B., Herkenhoff, K. E., Le Mouélic, S., Goetz, W., Madsen, M. B., Koefoed, A., Jensen, J. K., Bridges, J. C., Schwenzer, S. P., Lewis, K. W., Stack, K. M., Rubin, D., Kah, L. C., Bell, J. F., Farmer, J. D., Sullivan, R., Van Beek, T., Blaney, D. L., Pariser, O., Deen, R. G., Kemppinen, O., Bridges, N., Johnson, J. R., Minitti, M., Cremers, D., Edgar, L., Godber, A., Wadhwa, M., Wellington, D., McEwan, I., Newman, C., Richardson, M., Charpentier, A., Peret, L., King, P., Blank, J., Weigle, G., Schmidt, M., Li, S., Milliken, R., Robertson, K., Sun, V., Baker, M., Edwards, C., Ehlmann, B., Farley, K., Griffes, J., Miller, H., Newcombe, M., Pilorget, C., Rice, M., Siebach, K., Stolper, E., Brunet, C., Hipkin, V., Léveillé, R., Marchand, G., Sobrón Sánchez, P., Favot, L., Cody, G., Steele, A., Flückiger, L., Lees, D., Nefian, A., Martin, M., Gailhanou, M., Westall, F., Israël, G., Agard, C., Baroukh, J., Donny, C., Gaboriaud, A., Guillemot, P., Lafaille, V., Lorigny, E., Paillet, A., Pérez, Muriel, R. S., Yana, C., Aparicio, C. A., Caride Rodríguez, J., Carrasco Blázquez, I., Gómez Gómez, F., Elvira, J. G., Hettrich, S., Lepinette Malvitte, A., Marín Jiménez, M., Frías, J. M., Soler, J. M., Torres, F. J. M., Molina Jurado, A., Sotomayor, L. M., Muñoz Caro, G., Navarro López, S., González, V. P., García, J. P., Rodriguez Manfredi, J. A., Planelló, J. J. R., Alejandra Sans Fuentes, S., Sebastian Martinez, E., Torres Redondo, J., O'Callaghan, R. U., Zorzano Mier, M.-P., Chipera, S., Lacour, J.-L., Mauchien, P., Sirven, J.-B., Manning, H., Fairén, A., Hayes, A., Joseph, J., Squyres, S., Thomas, P., Dupont, A., Lundberg, A., Melikechi, N., Mezzacappa, A., DeMarines, J., Grinspoon, D., Reitz, G., Prats, B., Atlaskin, E., Genzer, M., Harri, A.-M., Haukka, H., Kahanpää, H., Kauhanen, J., Paton, M., Polkko, J., Schmidt, W., Siili, T., Fabre, C., Wray, J., Wilhelm, M. B., Poitrasson, F., Patel, K., Gorevan, S., Indyk, S., Paulsen, G., Bish, D., Schieber, J., Gondet, B., Langevin, Y., Geffroy, C., Baratoux, D., Berger, G., Cros, A., Uston, C. d., Lasue, J., Lee, Q.-M., Meslin, P.-Y., Pallier, E., Parot, Y., Pinet, P., Schröder, S., Toplis, M., Lewin, É., Brunner, W., Heydari, E., Achilles, C., Oehler, D., Sutter, B., Cabane, M., Coscia, D., Szopa, C., Robert, F., Sautter, V., Nachon, M., Buch, A., Stalport, F., Coll, P., François, P., Raulin, F., Teinturier, S., Cameron, J., Clegg, S., Cousin, A., DeLapp, D., Dingler, R., Jackson, R. S., Johnstone, S., Lanza, N., Little, C., and Nelson, T. (2013). Martian Fluvial Conglomerates at Gale Crater. *Science*, 340(6136):1068–1072.

Winn, J. N. (2010). Transits and occultations. *arXiv preprint arXiv:1001.2010*.

Witze, A. (2023). Life in the cosmos: JWST hints at lower number of habitable planets. Nature, 618(7967):897–898.

Wood, B. E., Müller, H.-R., Redfield, S., Konow, F., Vannier, H., Linsky, J. L., Youngblood, A., Vidotto, A. A., Jardine, M., Alvarado-Gómez, J. D., and Drake, J. J. (2021). New observational constraints on the winds of m dwarf stars*. *The Astrophysical Journal*, 915(1):37.

Xue, Q., Bean, J. L., Zhang, M., Mahajan, A., Ih, J., Eastman, J. D., Lunine, J., Mansfield, M. W., Coy, B. P., Kempton, E. M.-R., Koll, D., and Kite, E. (2024). Jwst thermal emission of the terrestrial exoplanet gj 1132b. *ApJL*, 973(1):L8.

Yabe, T. and Aoki, T. (1991). A universal solver for hyperbolic equations by cubic-polynomial interpolation i. one-dimensional solver. *Computer Physics Communications*, 66.

Yabe, T., Tanaka, R., Nakamura, T., and Xiao, F. (2001). Exactly conservative semi-lagrangian scheme (cip-csl) in one dimension. *Monthly Weather Review*, 129:332–.

Yau, A. W., Abe, T., and Peterson, W. (2007). The polar wind: Recent observations. *Journal of Atmospheric and Solar-Terrestrial Physics*, 69(16):1936–1983. Recent Advances in the Polar Wind Theories and Observations.

Yoshida, T., Terada, N., Ikoma, M., and Kuramoto, K. (2022). Less effective hydrodynamic escape of h ₂ –h ₂ o atmospheres on terrestrial planets orbiting pre-main-sequence m dwarfs. *ApJ*, 934:137.

Yoshida, T., Terada, N., and Kuramoto, K. (2024). Suppression of hydrodynamic escape of an h2-rich early earth atmosphere by radiative cooling of carbon oxides. *Progress in Earth and Planetary Science*, 11(1):59.

Zahnle, K. J. and Catling, D. C. (2013). The cosmic shoreline. In *44th Annual Lunar and Planetary Science Conference*, Lunar and Planetary Science Conference, page 2787.

Zahnle, K. J. and Catling, D. C. (2017). The Cosmic Shoreline: The Evidence that Escape Determines which Planets Have Atmospheres, and what this May Mean for Proxima Centauri B. *The Astrophysical Journal*, 843(2):122. https://iopscience.iop.org/article/10.3847/1538-4357/aa7846/pdf.

Zatsarinny, O., Gorczyca, T. W., Korista, K. T., Badnell, N. R., and Savin, D. W. (2004). Dielectronic recombination data for dynamic finite-density plasmas. iv. the carbon isoelectronic sequence. *A&A*, 417:1173–1181.

Zatsarinny, O., Gorczyca, T. W., Korista, K. T., Badnell, N. R., and Savin, D. W. (2005). Dielectronic recombination data for dynamic finite-density plasmas - iv. the carbon isoelectronic sequence. *A&A*, 440(3):1203–1204.

Zhang, M., Hu, R., Inglis, J., Dai, F., Bean, J. L., Knutson, H. A., Lam, K., Goffo, E., and Gandolfi, D. (2024). GJ 367b Is a Dark, Hot, Airless Sub-Earth. *The Astrophysical Journal Letters*, 961(2):L44.

Zieba, S., Kreidberg, L., Ducrot, E., Gillon, M., Morley, C., Schaefer, L., Tamburo, P., Koll, D. D. B., Lyu, X., Acuña, L., Agol, E., Iyer, A. R., Hu, R., Lincowski, A. P., Meadows, V. S., Selsis, F., Bolmont, E., Mandell, A. M., and Suissa, G. (2023). No thick carbon dioxide atmosphere on the rocky exoplanet TRAPPIST-1 c. *Nature*, 620(7975):746–749. ADS Bibcode: 2023Natur.620..746Z.

Zieba, S., Zilinskas, M., Kreidberg, L., Nguyen, T. G., Miguel, Y., Cowan, N. B., Pierrehumbert, R., Carone, L., Dang, L., Hammond, M., Louden, T., Lupu, R., Malavolta, L., and Stevenson, K. B. (2022). K2 and Spitzer phase curves of the rocky ultra-short-period planet K2-141 b hint at a tenuous rock vapor atmosphere. A&A, 664:A79.

Öpik, E. J. (1963). Selective escape of gases*†. *Geophysical Journal International*, 7(4):490–509.